Remote Sensing and GIS Models-Based Approach to the Land Cover Classification on Ahipara Region Using RapidEye and Landsat 7 (ETM+)

By

Abbas Sarkhosh

A thesis submitted to

Auckland University of Technology

in partial fulfillment of the requirements for the degree

Of

Master of Science (MSc)

2012

School of Applied Science

TABLE OF CONTENTS

Contents

List of Figures

Contents

List of Tables

Contents

List of Acronyms

AOI: Area of Interest

DN: Digital Number

DoC: Department of Conservation

ETM+: Enhanced Thematic Mapper Plus

GCP: Ground Control Point

GIS: Geographic Information System

GLCF: Global Land Cover Facility

LCDB: Land Cover Databases

LULC: Land Use/Land Cover

MfE: Ministry for the Environment

MLC: Maximum Likelihood Classifier

NIR: Near Infra-Red

PCA: Principle Components Analysis

PP: Parallelepiped

RapidEye: RE

ToA: Top of Atmosphere

UTM: Universal Transverse Mercator

VI: Vegetation Index

Attestation of Authorship

I hereby declare that this submission is my own work and that, to the best of my knowledge and belief, it contains no material previously published or written by another person (except where explicitly defined in the acknowledgements), nor material which to a substantial extent has been submitted for the award of any other degree or diploma of a university or other institution of higher learning.

Signed:

Abbas Sarksosh

Acknowledgements

I would like to express my gratitude to my supervisor, Dr Barbara Breen for her support, guidance and encouragement throughout the process of this research. I am also grateful to Dr. Salman Ashraf for his suggestions. I would special thank to Dr R. Klinger from Germany for dedicating his time and expertise to this project. I am also thankful to Dr D. Parker as he contributed to this project by editing some parts of my thesis. I would like to thank Dr Dan Breen for helping me to go and allowing me to see the study area (Ahipara).

Finally, I would like to thank my wife, Susan and my children, Niloufar, Amir and Parsa for their support and encouragements throughout my studies. I thank my parents, who always believe in me.

Abstract

In this study, RapidEye (RE_ 5m multispectral-orthorectified) and Landsat 7 ETM+ imagery over the Ahipara region were utilized to classify the land cover from the study area. Various methods of image classification were implemented to produce the thematic maps of the land cover types. Twelve classified images from the L7 and RE images were generated by using different band (432, 543) and principle components 1, 2 with vegetation index layer combinations, as well as applying the supervised classification algorithms, including the maximum likelihood classifier (MLC) and combination of MLC with the parallelepiped algorithm. The error matrix and Kappa statistic of the classified images were estimated. The results of the classified images for both sensors (L7 and RE) identified all classified images by PPMLC had a higher accuracy and Kappa statistic than the classified images used by MLC approach. Furthermore, the Kappa statistics and the overall accuracies represented that the Red-Edge band from the RapidEye system combined with NIR and Red can improve the classification performance as it is sensitive to distinguish in vegetation cover.

This study revealed that one of the most accurate procedures for classifying the RapidEye image of the study area was a combination of principal components and vegetation index layers (PC12VI) while the degraded images (RE with 30m spatial resolution) and also the images with 432 band combination had lower accuracy assessment results. The results of the classification processes and comparative assessments between LCDB2 and RE data indicated the RE_543_PPMLC and RE_PC12VI_PPMLC images had higher classification performance in discriminating land cover types than the LCDB2 classification.

The RapidEye high spatial and spectral-resolution image represented more accurate classification performance with useful information in classifying the study area in Ahipara region whereas the Landsat 7 classified images had moderate classification accuracy.

Chapter 1

Introduction

Traditionally, ecologists have used the direct sampling method to characterize shoreline and coastal habitats or classify land-cover features. However, this method is neither time nor cost effective for vast expanses of coastline. Remote sensing tools, such as aerial photography, airborne and satellite imagery, are appropriate for surveying and classifying marine habitats or land-cover features (Guillaumont, Callens, & Dion, 1993; Bajjouk, Guilaumont, & Populus, 1996; Guillaumont, Bajjouk, & Talec, 1997; Méléder, Launeau, Barille, & Rince, 2003; Combe, Launeau, Carrere, Despan, & Méléder, 2005).

Remote sensing technologies have been considered widely in forested and aquatic environments for mapping vegetation and other attributes (Banko, 1998; Czaplewski, 2003). Satellite imagery can be a significant source of environmental data that would be combined in GIS-based and marine ecosystem models with bathymetry, submerged vegetation, sea surface temperature, chlorophyll, and so on (Phinn, Roelfsema, Brando, & Anstee, 2008). High resolution remote sensing observation can be applied to monitor patterns and processes of selected ecosystem attributes over multiple spatial and temporal scales.

The vegetation or non-vegetation features on the Earth's surface that are assigned as land-cover would be monitored at the particular place and time (Campbell, 2002). In fact, land-cover demonstrates the observable data of land use including vegetation and non vegetation features. There is an obvious difference between land cover and land use, however they are often utilized identically with each other, in view of the fact that land-use is referred to as all controls and activities which are made by humans on the land while, land-cover includes all type of lands whether manipulated by humans for any purposes or not, for instance; grass, forest, urban and so on (Campbell, 2002). The change in land cover is widely considered as one of the main parameters of global change affecting biodiversity, ecological and environmental systems (Vitousek, 1994). Hence, land cover could describe the existence and non existence of such species and habitats on the specific area of the Earth's surface. The fire burning, deforestation and urban development, or other human activities are causes of the

land cover changes that can be mapped for further study and observation (Huang & Siegert, 2006).

As a result, it is essential to collect information for a range of purposes, for example, natural resources monitoring, detecting crop, agriculture, forestry, hydrological analysis and land management to apply some procedures for land-cover conservation or modification (Coppin, Jonckheere, Nackaerts, & Muys, 2004.

Supervised and unsupervised methods are generally implemented for land cover mapping, as explained in Campbell (2002), Franklin and Wulder (2002), Lillesand, Kiefer and Chipman (2004), Jensen (1996) and Liu, Skidmore and Van Oosten (2002). There are several methods that need to be considered to detect the land cover changes, however some of the applications are more regularly used depending on the purposes for which analyses are intended. These kinds of approaches can be categorized as pre-processing of satellite data before performing image classification and post-processing after image classification (Coppin et al., 2004; Lunneta & Elvidge, 1999). Utilizing a high resolution remote sensing satellite imagery can be the most efficient approach to provide large scale, high quality information for land-cover and land-use monitoring and classification (Hester, Cakir, Nelson, & KHorram, 2008).

1.1 Satellite Remote Sensing for Land Cover Mapping and Vegetation Monitoring in New Zealand

Satellite imagery has been available for New Zealand more than 30 years; The data over New Zealand were acquired by Landsat series (1, 2 and 3) and Spot satellites in 1970s and 1980s (Stephens, 1991). The Spot XS data was used by Israel and Fyfe (1996) for mapping of vegetation along the coastline of the Otago Harbour.

New Zealand Land Cover Database (LCDB) is database containing information about monitoring and mapping vegetation through remotely sensed images (Walker, Price, Rutledge, Stephens, & Lee, 2006). There are two versions of the LCDB, 1 and 2 that applied SPOT 2 (1996/97) and Landsat 7 (2001/02) images, respectively. The aim of the New

Zealand Ministry of the Environment (MfE) was to collect the data for land cover management and environmental change assessment (Thompson, Grüner, & Gapar, 2003).

1.2 Research Problem

In this study, the RapidEye (RapidEye AG, Inc.) and ETM+ images were applied to select training pixels to produce the reference data set for the classification procedure. There are different methods to cluster data pixels into classes with using various band combinations and classification algorithms so that the results can be different. Furthermore, the collection of a training sample may have a huge effect on the classification result. Using specific areas as training sites for the supervised classification can be more crucial than the selection of classification methods for finding out the accuracy of classification of agriculture fields in the United States (Scholtz, Fuhs, & Hixson, 1979; Al-Ahmadi & Hames, 2009; Campbell, 2002). In fact, an approach for selecting training sites relies on the purposes of the classification and the land-cover features identification where the specific area of interest (AOI) is considered to study (Jensen, 2005).

In multispectral image classification, the spectral raster data properties of each pixel which include several image layers can be converted into a specific set of categorization which signifies the land cover types as observed in the satellite imagery (Jensen, 2005). Remote sensing data can be analysed by different methods and purposes, including using a false colour-infrared (CIR) image and different band combination.

The best selection of three band combinations could be essential to represent appropriate information from a remotely sensed data set for demonstration and further analysis. The selection and combination of specific layers depends on the characteristics of the area under study, the spectral reflectance of an object and also using the data of interest. The desired bands from the data acquired can be selected according to the spectral band specifications of the sensor (Liu et al., 2002). On the other hand, applying image processing techniques may not detect or classify all features on the Earth's surface, for example, by using false colour composites, the soil or vegetation moisture cannot be monitored, but vegetation to be identified readily in the image because of a high reflectance in the NIR band. At the end of land cover classification, an accuracy assessment of the classification results could be applied, thus the ground truthing data for characterizing the area of interest with combination of enhanced layers would be essential.

The goal of this study was to assess the benefits of different approaches for using higher resolution imagery (represented by RapidEye imagery with 5m orthorectified, multispectral data) to classify lower resolution imagery (Landsat7 ETM+ at 30m resolution). The classification approaches were compared in terms of classification accuracy and included different band combinations, different training fields, and different classification algorithms. By using multi-spectral data such as RapidEye and Landsat7 (ETM+), general or specific vegetation classes can be identified and also the extensive vegetation communities can be discriminated (Harvey & Hill, 2001; Li, Ustin, & Lay, 2005). High resolution satellite imagery by RapidEye sensor would provide 5m multispectral resolution across 5 spectral bands, including blue, green, red, red-edge and NIR. These bands are uniquely chosen for a variety of applications resources management, vegetation detection, coastal mapping and environmental monitoring (RapidEye, AG 2012).

The specific aim of my research was to demonstrate that satellite remote sensing imagery and GIS application can be applied to detect and classify land cover from Ahipara Bay through to Herekino Harbour which is located in New Zealand's Far North (Figure 1.1).

Figure 1.1 Map of Northland Conservancy (MfE, 2010)

The following main objectives were implemented in this project:

1) To critically assess the effectiveness of the RapidEye and the Landsat 7 (ETM+) imagery to mapping land-cover in the Ahipara region.
2) To develop and apply different image classification methods on Landsat ETM+ and RapidEye data for optimal land cover classification.
3) To conduct a comparative analysis of the accuracy of the classification results for the RapidEye and Landsat7 images.
4) To conduct a comparative analysis of land cover classified using RapidEye imagery and the Land Cover Databases Version 2 (LCDB 2) from the Ministry for the Environment.

1.3 Structure of the Thesis

Land-cover classification was assessed by using RapidEye which is a high spatial and temporal resolution satellite (5m orthorectified, multispectral) and also Landsat 7 (ETM+) as medium spatial resolution (15m pan, 30m multispectral), with geographic information system (GIS) models. A variety of classification methods including different layer combinations, options for characterizing training fields, and different classification approaches (algorithms) were compared in terms of classification accuracy using ERDAS Imagine as an advanced remote sensing analysis and spatial modelling application.

1.3.1 Thesis Outline

Chapter1 provides a general introduction that indicates the research problems and objectives.
Chapter 2 provides a literature review and research background.
Chapter 3 describes the methods used to connect observational and experimental evidence.
Chapter 4 provides some results of the study, accuracy assessments, Landsat 7 and RapidEye images classification.
Chapter 5 contains discussion, conclusion and recommendation that identify the important findings of this study effort for future research.

Chapter 2

Literature Review

2.1 Overview of Remote Sensing in Environmental Modeling

Every piece of land on this earth's surface presents a distinctive feature in terms of the cover it possesses (Meyer, Staenz, & Itten, 1996). Land use and land cover are two distinct aspects, yet they are linked to one another. Land use includes agricultural land, land for urban area development, logging and mining land and so forth. On the other hand, land cover classification may be ranked as farming land, forests, wetland, roads, urban areas and so forth. Land cover can refer to the classification of land according to state of its existing plant life for instance, forest cover. However, it may also be used in identifying the subsequent procedures that can include human inhabitation structure, soil type, bio-diversity and so forth.

According to Riebsame, Meyer, and Turner (1994), Turner, Ollinger and Kimball (2004), Sundarakumar, Harika, Begum, Yamini, and Balakrishna (2012), Land-use and land-cover change can provide as warning sign of the economic causes of environmental change. The changes can impact on a local or global range of environmental characteristics including the quality of water, land and natural resources, ecosystem developments, and the climate system. The land use/land cover model of an area is a result of natural and human activities. In fact, land use has direct effects on land cover and, changes observed on land cover affects land use. However, they argue that land transformation in aspect either does not necessarily mean it is a creation resulting from the impacts of the other. There are so many factors that would involve the land cover and land use changes.

The result of land cover change that have a direct influence on biodiversity of some aspects such as water as well as emission released in the form of trice gases among other development that on overall come together to affect both climate as well as affect the biosphere.

Not only anthropogenic, but also other forces can distort similar arguments on Land cover (Manandhar, Odeh and Ancev, 2009). There are natural events that can be a cause to land cover change. This may be in the form of weather, flooding and environmental dynamics, which are identified to have effects that may result to modification on land development. However, current trend across the globe indicates that land cover alteration is principally through direct human land use, by either agricultural practices, forest harvesting or through land development in the urban region as well as suburban areas. There are cases where land cover is altered by human activities for example, lakes and forest damage through acidic rain caused by fossil energy ignition, while most of the crops within the urban areas are toxified through extensive use of tropospheric zone that is released to the ozone from diesel fuel engines.

In order to use land effectively, it is not only necessary to have information on existing land use/cover, but it is also important to understand the capability to monitor dynamics of land use as a result of both change in demands of increasing population and forces of nature acting to shape the landscape. The traditional ground methods of land use mapping are labor intensive and time consuming and at the same time relatively infrequent (Manandhar et al., 2009). These traditional mapping models are soon becoming outdated with the passage of time, notably in rapidly changing environments. Some researchers have monitored changes and time series analysis reveals that this process in itself is difficult if traditional methods of surveying are to be used. More recently, satellite remote sensing methods have been applied, which have provided benefits for mapping the land use or cover maps while examining any identifiable transformation achieved at regular timeframes. Remote sensing provides a reliable technique, which is possibly the only technique of acquiring broad scale data on a cost-effective and timely basis, especially to inaccessible or remote areas. Marine ecologists have for decades used the direct sampling method to discriminate shallow and intertidal marine vegetation and habitats for classification and mapping. However, this method requires extensive field work. Remote sensing reduces the time and effort in obtaining large amounts of data directly from the field, particularly in marine environments that are often remote and difficult to access (Holden & LeDrew, 1998). In fact, remote sensing is defined as the technique of capturing information of an object, area or phenomena from a distance and all the acquired data can be analyzed by using digital image processing techniques without making any physical contact with the object (Thomas, Davies, & Dunn, 2004; Chandra, Ziemke, Bhartia, & Martin, 2002; Luzi, Monserrat, Crosetto, Copons, & Altimir, 2010). This

procedure is getting close to mathematical concepts when the satellite sensor is getting started to calculate the quantity of electromagnetic radiation (EMR) reflected an object or Earth's surface from the space or distance and also deriving precious information from a digital remotely sensed data with applying the statistical and mathematical algorithms, it would be a scientific process (Fussell, Rundquist, & Harrington, 1986).

Remote sensing tools, such as aerial photography, airborne and satellite imagery, are appropriate for surveying and classifying marine habitats in the tidal zone and land cover features (Guillaumont et al., 1993; Bajjouk et al., 1996; Guillaumont et al., 1997; Méléder et al., 2003; Combe et al., 2005). Use of remotely sensed data in natural resources mapping and as a source of input data for environmental processes modeling has been popular in modern times. Due to the availability of remotely sensed data from sensors of diverse platforms, with a series of spatiotemporal radiometric, as well as spectral resolutions, is achieved remotely sensing as the best source of data for large scale applications and research (DeFries & Chan, 2000). Remote sensing techniques create a possibility for images for target land surface taken in different wavelength as per the area of the electromagnetic band (EMS). For instance, remote sensing is applied in hydrological modeling and imaging fractional vegetation cover and urban modeling. Similarly, aspects such as drought prediction can be forecasted through monitoring soil water index, whose data can be obtained from remotely sensed technique (Vogelmann, Sohl, & Howard, 1998).

High resolution remote sensing observation can be applied to monitor patterns and processes of selected ecosystem attributes over multiple spatial and temporal scales. These techniques have been used for decades to make regional observations of coastal marine ecosystems (Tucker, 1979; Jensen, 1996; Deysher, 1993). For this advantage, many researchers have used multi-spectral data such as Landsat TM, SPOT, RapidEye and QuickBird imagery to identify general vegetation classes or to attempt to discriminate broad vegetation communities (May, Pinder, & Kroh, 1997; Harvey & Hill, 2001; Li et al., 2005), and hyper-spectral data to discriminate and map coastline vegetation or at the species level (Belluco, Camuffo, & Ferrari, 2006; Skidmore, 2002; Rosso, Ustin, & Hastings, 2005; Pengra, Johnston, & Loveland, 2007; Vaiphasa, Ongsomwang, Vaiphasa, & Skidmore, 2005).

2.2 Remote Sensing Sensors

Remote sensing is primarily a process, which relies on sensors obtaining information from an object while not in direct contact with the object under investigation. Consequently, sensors usually detect either emitted or reflected electromagnetic energy from the investigated object, which is often found on the Earth's surface.

Each satellite carries specific platforms and sensors with a variety of characteristics, and these are able to detect and acquire all radiations reflected from the object on the Earth's surface (Wulder, Hall, Coops, & Franklin, 2004). All sensors are categorized based on the source of energy on the Earth or from the Sun. The energy that is naturally available, including all reflected energy during the time when the sun is illuminating the earth, can be estimated by passive sensors remotely. On the other hand, active sensors are able to generate their own energy source for radiance.

2.3 Remote Sensing in the Optical and Microwave Domains

Remote sensing is a process involving interaction between radiance and objects in which the emitted and reflected electromagnetic radiance can be detected by satellite sensor. After acquiring data from sensors for further processing and analysis, all data to be transmitted to the Earth to monitor any environmental changes and issues (Campbell, 2002).

The electromagnetic spectrum ranges which are used extensively for remote sensing applications are in visible and microwave. The optical wavelength includes a visible portion about 0.4 µm to 0.7 µm as well as infrared ranges about 0.7 to 300 µm (Near IR, Middle IR and Far IR). The microwave region (1 mm to 1 m) is another part of EM spectrum that is frequently used to gather valuable remote sensing information (Jensen, 2005).

2.3.1 Electromagnetic Radiation

Remote sensing is the science of acquiring data (temporal, spectral, and spatial) about areas, objects or features without any physical contact with the items or areas under observation. In remote sensing the data transfer is performed by utilizing of electromagnetic radiation

(EMR). One of the main sources of remote sensing data is the electromagnetic radiation (EMR), which is reflected from an object on earth. The extensive range of electromagnetic spectrum (EMR) from gamma ray (short wave) to a very long Radio wave can be used in remote sensing technology (Figure 2.1). There is the optical wavelength of EMR with the different range of EM spectrum from gamma ray, X-ray, ultraviolet (UV), visible light, infrared (IR) and radio wave (Reitz, Facius, Bilski, & Olko, 2002)

Visible range	0.38 – 0.72 mm
Near IR (NIR)	0.72 – 1.30 mm
Middle IR	1.30 – 3.00 mm
Far IR Thermal	7.00 – 15.00 mm
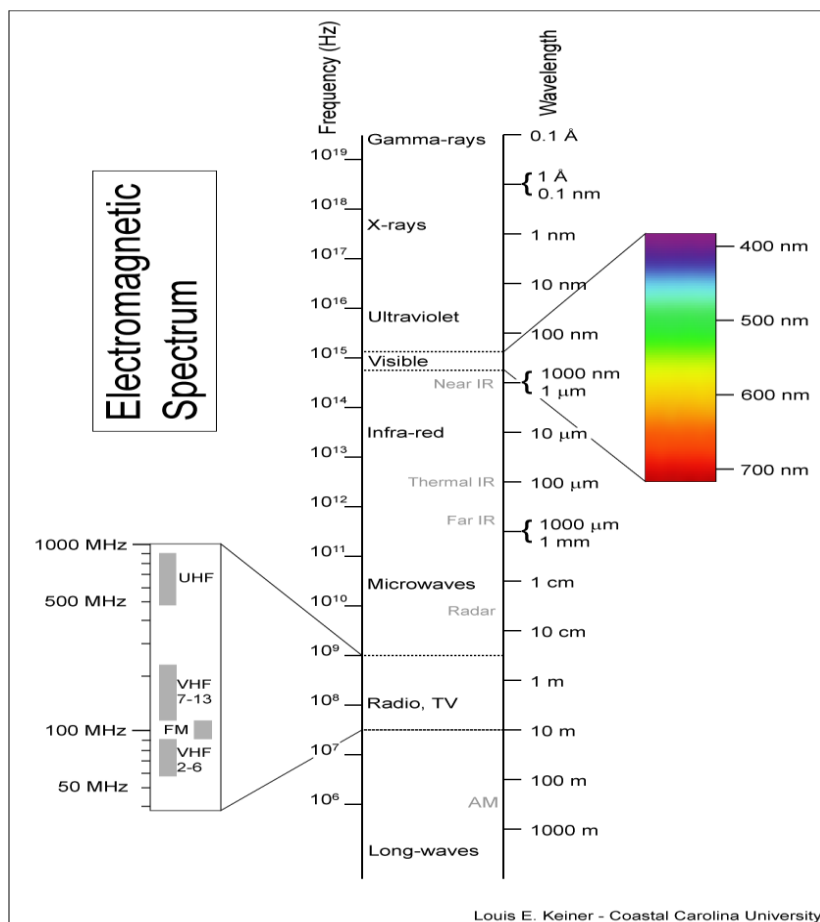
Figure 2.1Electromagnetic spectrum (Keiner, 2003).

For example, the far infrared region can be used to detect thermal signatures for fire monitoring. The optical satellite sensors are capable to estimate the amount of radiation such as light or radiant heat which is called the radiance that is emitted by a specific area or object. The radiance SI unit is watts per steradian per square meter (w.sr-[1].m-²). Radiance indicates total emission from the source and reflection of the describe surface. The spectral radiance SI units are w.sr-[1].m-².Hz-[1] or wavelength (nm), w.sr-[1].m-².nm-[1]. The fact of irradiance is the amount of radiation occurrence on unit area of a surface. It is defined in watts per square meter w/m² or w. m-².nm-[1].

2.3.1.1 Spectral Reflectance Curves

Spectral reflectance curves are the spectral response that is measured in order to assess the condition of the target feature. It is hence a graph of spectral reflectance of a feature as a function of wavelength. Spectral reflectance is the basis for the color in satellite images of a feature. For instance, vegetation mainly appears green because it reflects a great amount of green wavelength. Various features have varying values of spectral reflectance over a defined wavelength interval, hence the determination of vegetation and other features in Ahipara. It is therefore, dependant on wavelength having a variety of values on various terrain features (Jenson, 1996). Consequently, the plot between reflectivity and wavelength is depicted as spectral reflectance curve, which vary depending on the chemical composition and physical situation of the feature.

$$P(\lambda) = [E_r(\lambda) / E_I(\lambda)] \times 100$$

Legend:

$\rho(\lambda)$ = Spectral reflectance (reflectivity) at a particular wavelength.

$E_R(\lambda)$ = Energy of wavelength reflected from object

$E_I(\lambda)$ = Energy of wavelength incident upon the object

Source: (Jenson, 1996)
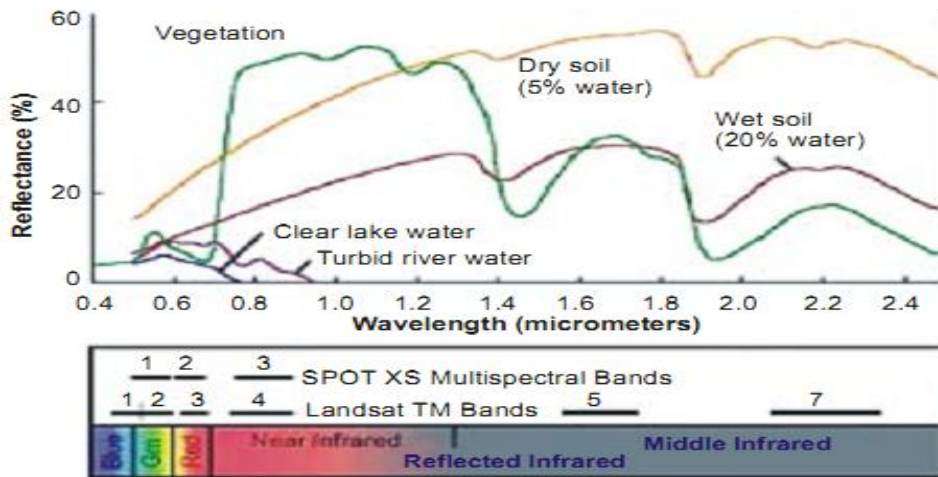
Figure 2.2The diagram shows a typical reflectance signature of various features on earth's surface (Jenson, 1996).

When the energy is reached to the surface it is called irradiance which is reflected by the surface as called radiance. Each object on the surface has specific reflectance that is a part of the radiation that will be reflected as a wavelength operation (Henry, Chastanet, Fellah, & Desnos, 2006).

The longer wavelength bands commonly are used by remote sensing. The reflectance curves are created in optical range of EM will be used to estimate the overall reflectance in such bands. There are some of the land cover types with their reference (Figure 2.2).

2.3.1.2 Vegetation

Reflectance curve for green vegetation can be distinguished with wavelength (Aggarwal, 2003). As shown in Figure 2.3 the most absorption or lowest reflectance regions of the visible spectrum occur in blue and red bands. The chlorophyll of the green leaf can absorb the maximum of the energy emitted by the sun. There is a high reflectivity of green vegetation in the near infrared section of the spectrum (0.7µm).
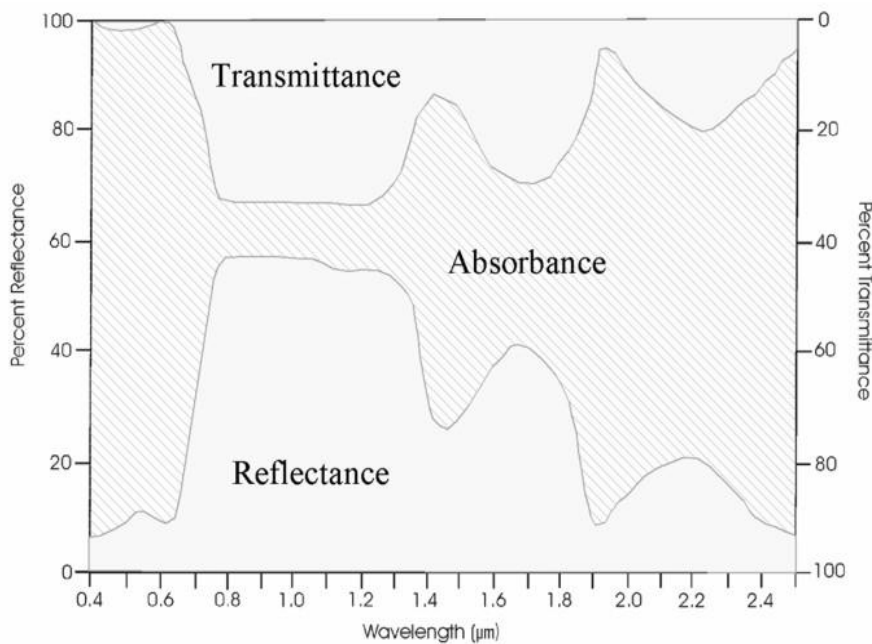
Figure 2.3The domain of optical observations extends from 400 nm in the visible region of the electromagnetic spectrum to 2500 nm in the shortwave infrared region.

2.3.1.3 Normalized Difference Vegetation Index (NDVI)

NDVI is one of the commonly used vegetative indices, which consisting an index primarily for plant photosynthetic action. The vegetative indices are often generated due to the reflective effect generated from different types of lights hitting the surface, while it still reflects a bigger position that is next to infrared light. On the other hand, the non-vegetated land cover posse a bigger reflectance on the light spectrum. If the ratio of the infrared bands and the red ratio generated from a remotely sensed surface image or even an indicator of vegetation increased the possibility of identification. NDVI is perhaps the most common of all ratio indices used in vegetation detection.

NDVI is computed based on a per-pixel considering the normalized disparity between red and close to infrared bands and indicated from the identified image. This implies that the NDVI is actually a regular grid-distributed across with an expression that reveals specified resolutions according to the data source. In fact, the ground characteristic groups themselves through identifying inner characteristics that illustrated in remote sensing imageries, when textures, digital numbers among other things detected. This paper proposes new models that

are lays its basis on the advanced division and data integration aimed at performing a land use classification. Particularly, for urban vegetation examination and extraction, the model makes use of ASTER data in developing a hierarchical resolution importantly to reflect the inbuilt relations between the land surface features under different scale levels (Shirish, Roy, & Sharma, 1995).

2.3.2 Energy Interactions in the Atmosphere

The satellite sensor gather the radiation from the sun and energy emitted by the Earth however, the electromagnetic energy should pass through the atmosphere hence, it can affect on the sensor's observation (Tso & Mather, 2009).

The electromagnetic radiation can be changed on the intensity and direction when it travel s through the atmosphere so that two basic components are known as Scattering and Absorption which are needed to consider when measuring radiation (Jensen, 2005).

2.4 Data Requirements

Remote sensing data can be specified in terms of spectral, radiometric, temporal and spatial (Lefsky, Turner, Guzy, & Cohen, 2004). The spatial resolution and the region under investigation with the other surveyor's considerations can be the most priorities to choose the satellite acquired data (Lu & Weng, 2007). If the objective of using satellite imagery for land cover classification is at the small scale, it should be a high resolution image like Ikonos, RapidEye and QuickBird imagery that could be required. Landsat TM and ETM+ data as a medium spatial resolution or MODIS imagery are used for different purposes and scales.

2.4.1 Spectral Resolution

For remote sensing applications to effectively create desired image, distance separating the target object to be detected, in addition, the platform has a critical role in pinpointing out the detail that regard useful information acquired on the entire area, for classification. The involved Sensors platforms that are identified to be far from the main targets, naturally view a wider area, however, they cannot provide much detail (Behnia, 2005). When compared to an

astronaut involve space shuttle that one can view while off the target location from a distance located airplane. The spectral resolution of a remotely sensing system can described as its ability to differentiate different parts of the range of calculated wavelengths. In essence, this amounts to number of wavelengths intervals measured and how narrow each interval is. The finer the spectral resolution, the narrower the wavelength for a specific band, for instance black and white films have a characteristic lower spectral resolution as compared to color films.

Image produced by sensor system contain wider wavelength band, several wide-ranging bands or even many narrow wavelength bands. The names used for these three categories are panchromatic, multispectral and hyper-spectral (Atmopawiro, 2004). Whereas, multispectral sensors mainly measure energy over several separated wavelength ranges, considering various spectral resolutions. With the advanced system, sensors detect numerous narrow spectral bands throughout the near infrared, visible and mid-infrared parts of the electromagnetic spectrum. As a result, such sensors promote fine discrimination between various targets basing on their specific spectral response in the various bands (Table 2.1).

Table 2.1Characteristics of selected satellite sensors (Hester et al., 2008)

Sensor Mission	Organization	Operation period	Swath width (km)	Spatial res.	Temporal res.	Radiometric res.	Spectral res. (μm)	Spectral Channels
MSS (Landsat 1-5)	NASA, USA	1972-1983	185	75 (MS) 240 (TIR)	16-18 days	8-bit	0.5-12.6	4
AVHRR (NOAA 6-15)	NOAA, USA	1978-	2700	1100	12 hours	10-bit	0.58-11.5	5
TM (Landsat 5)	NASA, USA	1984-	185	30 (MS) 120 (TIR)	16 days	8-bit	0.45-2.35	7
HRV (SPOT 1-3)	SPOT Image, France	1986-	60	10 (PAN) 20 (MS)	26 days	8-bit	0.50-0.89	3
LISS-I (IRS-1A)	ISRO, India	1988-	148	72.5	24 days		0.45-0.86	4
LISS-II (IRS-1B)	ISRO, India	1991-	146	36.25	24 days		0.45-0.86	4
SAR, OPS (JERS-1)	NASDA, Japan	1992-	75	18	44 days		0.43-1.7	7
LISS-III (IRS-1C, 1D)	ISRO, India	1995-	142	23, 70 188 (WiFS)	24 days	7-bit	0.52-1.7	4
SAR (RADARSAT-1)	Canada	1995-	45-500	8-100	24 days	4-bit	N/A	1
Panchromatic (IRS-1D)	ISRO, India	1997-	70	5.8	24 days	7-bit	0.50-0.75	1
GOES-8,10	NESDIS, USA	1994-	8	1000 (VNIR) 8000 (SWIR) 4000 (TIR)	0.25 - 3 hours	10-, 13-bit	0.52-12.5	5
SAR OPS (ERS-2)	ESA	1995-	102	26	35 days		N/A	N/A
HRVIR (SPOT 4,5)	SPOT Image, France	1998-	60	10 (PAN) 20 (MS)	26 days	8-bit	0.50-1.75	3
Vegetation (SPOT 4,5)	SPOT Image, France	1998-	2250	1150	26 days	8-bit	0.43-1.75	5
SeaWiFS (OrbView-2)	GeoEye, USA	1997-	2800	1130	24 hours		0.40-0.88	8
MODIS (EOS)	NASA, USA	1999-	2300	250 (PAN) 500 (VNIR) 1000 (SWIR)	1-2 days	12-bit	0.620-2.155, 3.66-14.385	36
ASTER (EOS Terra)	NASA and MITI, USA	1999-	60	15 (VNIR) 30 (SWIR) 90 (TIR)	4-16 days	8-, 8-, 12-bit	0.52-0.86, 1.60-2.43, 8.125-11.65	14
MISR (EOS Terra)	JPL and NASA, USA	1999-	360	275	16 days		0.425-0.886	4
ETM+ (Landsat 7)	NASA, USA	1999-	185	15 (PAN) 30 (MS) 60 (TIR)	16 days		0.45-2.35, 10.4-12.5	7
IKONOS	Space Imaging, USA	1999-	11	1 (PAN) 4 (NIR)	2-5 days	11-bit	0.45-0.90	4
QuickBird	DigitalGlobe, USA	2001-	6, 30	0.61 (PAN) 2.44 (MS)	1-4 days	11-bit	0.45-0.90	4
Hyperion and ALI (EO-1)	NASA, USA	2000-	7.5, 185	10 (PAN) 30 (MS)	16 days		0.433-2.35	242, 9
MERIS (Envisat-1)	NASA, USA	2001-	1150	300, 1200	35 days		0.39-1.04	Up to 15
ASAR (Envisat-1)	NASA, USA	2001-	400	30	35 days		Radar	1
HRG (Spot 5)	SPOT Image, France	2002-	60	5 (PAN) 10 (VNIR) 20 (SWIR)	26 days	8-bit	0.48-1.75	3
OrbView-3	GeoEye, USA	2003-2007	8	1 (PAN) 4 (MS)	3 days	11-bit	0.45-0.90	4

2.4.2 Spatial Resolution

The spatial, spectral and temporal components of the image(s) that all provide information that we use in forming interpretations about surface materials and their present conditions. Understanding the properties, we can define resolution of the images generated by the classification system. Image resolution has several aspects or features in place that limits information, which is usually generated by remotely sensed imagery data (Goetz, 1997). In particular, spatial resolution measures special detail in the generated image, elaborating on the function of the design of sensor as well as its operating elevation above the target surface. The smaller each individual patches are the more detailed is the spatial information that can be used to construe the image. For digital images, spatial resolution can commonly be compared to the ground proportions of an image cell. Shape is one visual factor, which can be

useful in recognizing and identifying image(s) (Behnia, 2005). Often, shape can only be discernible if the object dimensions are larger compared to the cell dimensions. Spatial resolution is highly dependent on IFOW, which is the angular funnel of perceptibility of the employed in a remote sensing sensor. On this case the cone of IFOV into the earth's surface or any other surface that is, Ahipara is referred to as resolution cone (Cakir, Khorram, & Nelson, 2006). Consequently, spatial resolution is managed by the separation between remote sensing sensor and the target (Table 2.1).

Spatial resolution in terms of a homogenous feature measured and detected, the objects' dimension has to have the same ratio as the resolution cell or rather larger when contrasted to the latter. On this incidence when the size of the object is smaller compared to the resolution cell, can be difficult to identify because the mean intensity of present objects in the resolution cell that may be verified (Cakir et al., 2006).

2.4.3 Temporal Resolution

The environmental surface of the earth's dynamic, which is progressively transitioning ranging from seconds to decades. The periodic cycle on the continuous growth of plants, which affects natural ecosystem, is a vital example (Ashraf, Brabyan, Hicks, & Collier, 2010). Through repeated imagery of a similar area after some period adds to the potential of one to detect and distinguish between two phenomena for instance plants. Moreover, a time series can also be employed to monitor variations on earth surface features because of other natural activities or human triggered activities. Thus, this period, which separates consecutive images in such a sequence, defines temporal resolution of image sequence.

Therefore, temporal resolution depicts the frequency with which the remote sensing system images the same area over a given period of time say one planting season. When the frequency of imaging is high, it is significant in monitoring and management of environmental issues such as soil erosion, vegetation cover and encroachment of human activity. Moreover, this is also employed in change detection (Atmopawiro, 2004).

A majority of surface-monitoring satellites is spatially gyrating in low-Earth orbit of an altitude approximately 650-850 Km above the earth's surface and pass almost close to the

poles that is North and South Pole. Mainly the satellite completes numerous orbits in 24 hours in accordance with the Earth's rotation beneath the system (Masek, Honzak, Goward, Liu, & Pak, 2001). The determining factors of the periodic interval between repeat passes over a similar point on the surface are the orbital parameters and swath width. For instance, periodic interval between repeat passes of Landsat7 TM satellite is usually 16 days. Therefore, placing duplicate satellite in offset orbits such as LandSat7 series (EMT, TM) and RapidEye is a major approach towards minimizing the repeat periodic interval.

2.4.4 Radiometric Resolution

For a sensor's detector to be capable of detecting digital energy characteristic progressive range of incoming energy must be split into a number of distinct levels recorded in integer values. Most of up-to-date satellite systems split data into 256 levels. This element is dependent on the number of levels recorded that is the greater the number the higher the radiometric resolution. On this case, this element provides the system with the ability to discriminate minute differences using the recorded energy. Thus, the finer the radiometric resolution the sensor the higher the sensitivity in detecting minute differences in emitted energy (Nelson, Niemann, & Wulder, 2003).

During the analysis of bands of multispectral images (RapidEye) of Ahipara, high radiometric resolution was relevant when utilizing a computer to manipulate and examine the band's numerical values. Moreover, use of visual analysis of multispectral images with high radiometric resolution is beneficial, this is because a defined variety of wavelength bands can be coalesced to create a color display. Each band is usually assigned to each of the RGB monitor colors (Red, Green, and Blue). With additive color model of the three monitor colors (RGB), they band together to form numerous variety of `subtle colors. On this event, each cell within the multispectral image disparity values in the chosen bands establishes the RGB values that were used to generate the color relayed (Nelson et al., 2003). Through using the 256-color channel, a computer VDU would creates over 16million colors. Recent research indicates that the human visual system can differentiate approximately 7 million colors and is extremely familiar to spatial associations this is in relation to the area under investigation. Notwithstanding the power of the computer system examination, the visual system analyses color present in a multispectral imagery that may still be an effectual device in interpretation.

2.5 The Satellite Imagery Used in This Study

2.5.1 RapidEye

RapidEye AG is an information system provider that was heavily used in the study of the area under investigation, Ahipara. It primarily focuses on aiding in the management administrative through provision of information based on observation made via imagery obtained from the systems. An ocular system, five satellites, five bands, and a 5m resolution (orthorectified) system characterize it. The system usually quantifies the reflectance of UV radiation from the earth in numerous bands (5 bands). On this case, the Red-edge band is highly sensitive concerning the N-status of vegetation. This element is significant in analysis procedures in vegetation monitoring in its various applications (Figure 2.4).
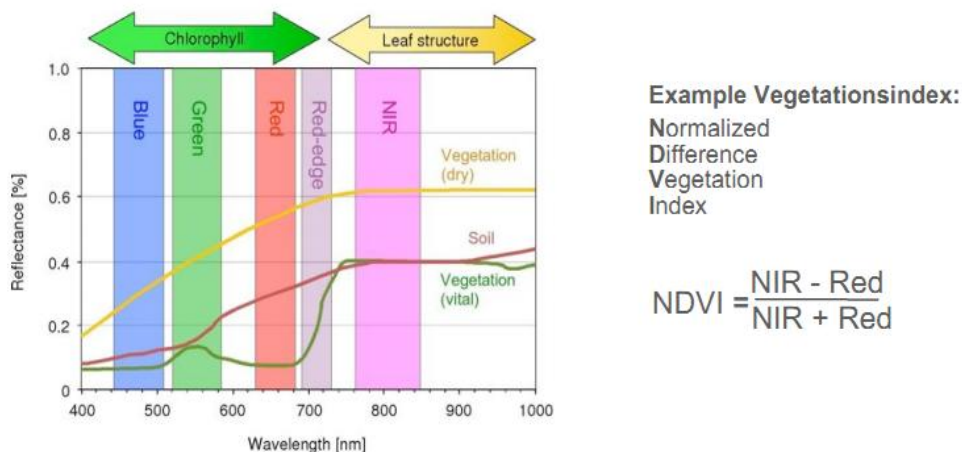
Figure2.4 RapidEye multispectral bands (Losel, 2009).

The system basing on its application in fields such as Agriculture, uses NDVI approach, which is to a large, extend used index in vegetation canopy studies in conjunction with remote sensing methodologies. It is the ratio between near infrared and red reflectance denoted as (NIR-Red) :(NIR + Red) = NDVI (Normalized Difference Vegetation Index). The approach can be also specifically applied on vegetative information (Murakami, Ogawa, Ishitsuka, Kumagai, & Saito, 2001).

As a result, the system provides information based on management remedies in various sectors associated with geospatial information such as Agriculture (effective farming operations), risk assessment, forestry (unlawful logging) and deforestation. On this event RapidEye is AG based which utilizes Red Edge canal that appreciates the efficiency of detecting chlorophyll content, with the 5 satellites the system is able to cover larger geographical area at a much higher interval, hence up-datedness in imagery (Losel, 2009). The system framework is based on:
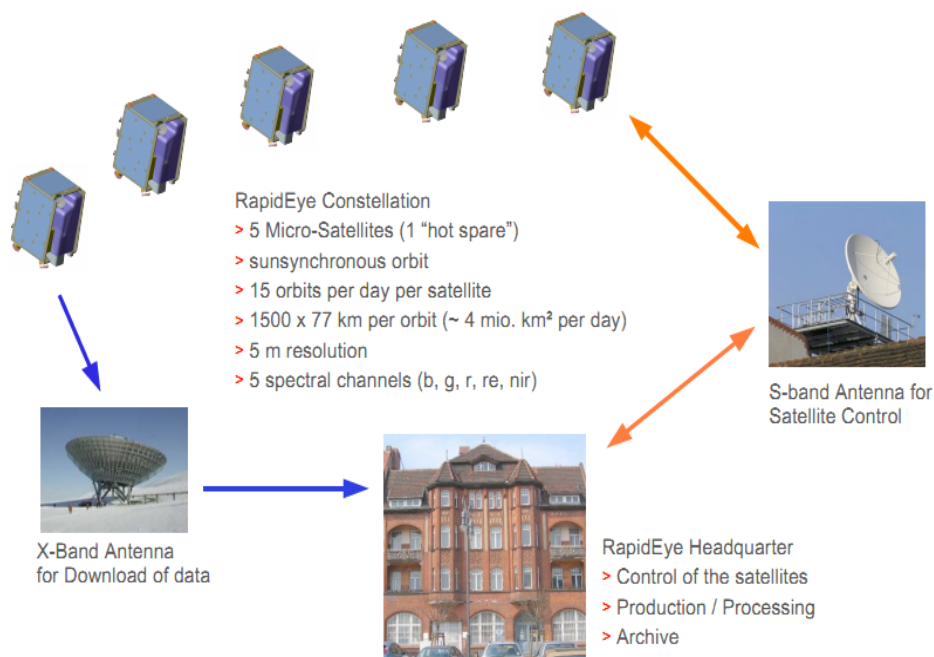
Figure 2.5 RapidEye's framework (Losel, 2009).

2.5.2 LANDSAT 7 (ETM+)

LANDSAT 1-7 series were made and launched by United States which they have the longest record and vastest utilization for investigation of the surface of the Earth. The first of these was launched by NASA, USA in 1972. The different kinds of more advanced multispectral sensors are carried by LANDSAT satellites for example, Thematic Mapper (TM, 1982), Multispectral Scanner (MSS, 1984) and Enhanced Thematic Mapper Plus (ETM+, 1999).

A full coverage of Landsat MSS, TM and ETM+ sensor have acquired millions images that still some of them are nonstop gathering the data from the Earth surface during their

operations and the acquisition data supplied by the United State Geological Service on the USGS website for near to 40 years.

Table 2.2 Landsat ETM+ and TM technical information (Colby & Keating, 1998).

	Thematic Mapper (TM)	Enhanced Thematic Mapper Plus (ETM+)
Platform	Landsat 4 (launched 16 July 1982) Landsat 5 (launched 1 March 1984)	Landsat 6 (failed on launch) Landsat 7 (launched 15 April 1999)
Orbit	16 day/705 km	16 day/705 km
Inclination	98.2°	98.2°
Equatorial crossing time	10:00 am	10:00 am
Swath width	185 km	185 km
Bands	1 (0.45-0.52µm) 2 (0.52-0.60µm) 3 (0.63-0.69µm) 4 (0.76-0.90µm) 5 (1.55-1.75µm) 6 (10.4-12.5µm) 7 (2.08-2.35µm)	1 (0.45-0.52µm) 2 (0.52-0.60µm) 3 (0.63-0.69µm) 4 (0.76-0.90µm) 5 (1.55-1.75µm) 6 (10.4-12.5µm) 7 (2.08-2.35µm) panchromatic band 8 (0.50-0.90µm)
Ground pixel size	30 m (bands 1-5,7) 120 m (band 6)	30 m (bands 1-5,7) 60 m (band 6) 15 m/18 m (band 8)
Quantisation levels	8 bits	best 8 of 9 bits

Landsat series have provided the data for remote sensing and Geographic Information System (GIS) science and remotely sensed the valued multispectral imagery for the natural resources monitoring on the global base and global purpose such as agriculture activities, urban development, forest evaluation, oceanography and hydrobiology considerations.

Enhanced Thematic Mapper Plus (ETM+) instrument is an enhanced version of its earlier sequence of the Thematic Mapper series that sited on Landsat 4 and 5. ETM+ sensor has the capability to acquire data in eight spectral bands including visible/near infrared (VNIR), short-wave infrared (SWIR), long-wave infrared (LWIR), thermal infrared and panchromatic with wavelengths ranging from 0.45 to 12.50 µm and a spatial resolution of 30 meters for visible bands, 60 meters for thermal band and panchromatic band at 15 meters resolution. This satellite was designed to orbit at 705 km in altitude and also has a fixed 16-day repeat coverage with 233 orbits cycle, as is the 185 km (115 mi) swath width for imaging (Table 2.2).

Landsat 7 could supply sufficiently reliable data with indication to special and spectral resolution; acquisition geometry and calibration to approach global change research necessities ensure a sustainable future for the globe and people.

For mapping vegetation largely at the specific area, Landsat series data have been utilized. As Landsat has archived a massive amount of information since it was launched, it is significantly useful to create map for vegetation cover and investigate on its changes. For instance, almost 20 year nonstops Landsat TM/ETM+ imagery covering the Western Oregon were applied to distinguish and differentiate permanent changes in near the beginning forest progression (Schroeder, Canty, &Yang, 2006). Thematic Mapper imagery was used to perform in determinable analyses of wetland region models and changes in the Minjiang River estuary at a long term period from 1986 to 2002 (Zheng, Zeng, & Chen, 2006). As a consequence of the different distinctiveness of spectral resolution of sensors (i.e. TM and ETM+) in the Landsat imagery series, it is required to accurate the spectral reflectance among images acquired by the sensors. For utilizing TM and ETM+ images, it can be particularly crucial in long term vegetation cover observing study. An empirical line method was suggested by Moran, Bryant and Thome (2001) for reflectance factor retrieval (RFR) from Landsat 5 TM and Landsat 7 (ETM+). Due to the medium level of the Landsat spatial resolution, its data are typically applied to map vegetation at small and medium scales. It is a tough undertaking to employ Landsat images for identifying and mapping at species scale, in particular in a case of heterogeneous surface. Nevertheless, when merging with other secondary datasets, it will be possible to determine some species and create a map. In the Amanos Mountains region of southern central Turkey, Landsat imagery was used with the environmental parameters data and a series of forest supervision maps to classify the vegetation species of the study area (Domacx & Suzen, 2006). As the medium level of the Landsat spatial resolution provides a limitation for acquiring data, the comparatively lack of its temporal resolution can confine using Landsat imagery for vegetation mapping.

Landsat satellites are popular and sun synchronous. It takes; 16 days for the satellites to revisit the last location. This inflicts an issue to map vegetation applying Landsat monitoring specifically when the surface is covered by cloud during the winter and it might significantly reduce the image quality.

As a result, for any remote sensing analyst who is interested to study on vegetation map, satellite's repeat coverage interval is very essential to get the mapping function to order a satellite image.

Recent research shows that other versions of Landsat 5,6,7 tremendous developments. For instance the diagram below (Figure 2.6) reveals that ETM+ in high-gain mode verifies up to 1 bit of additional information for explicit bands and vegetation cover variety. Bands 2, 3, and 7 revealed distinct appreciation in information content for various vegetation varieties, on the other hand band 4 revealed an appreciation for grassland and crops. There was a minute change in band 1 and 5 in comparison with Landsat-5 TM of ETM+ bands.
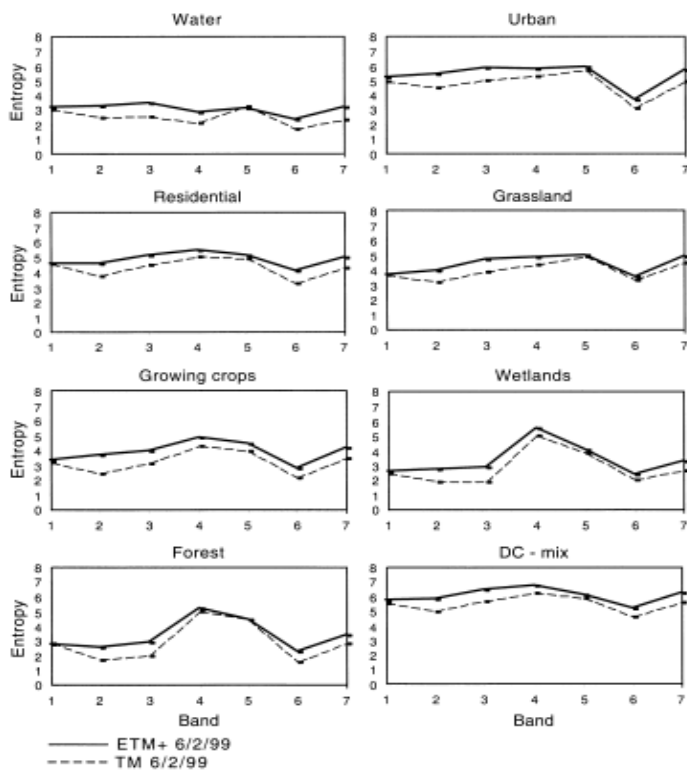
Figure 2.6 Entropy per band (bits) for Landsat-5 TM (dashed line) and Landsat-7 ETM+
Source: (Masek et al., 2001)

The figure depicts the entropy per bit for the systems: Landsat5 shown by dashed lines and Landsat7 ETM+ shown by solid lines from information that was acquired concurrently under fly in 1999 of Washington DC region (Masek et al., 2001).This will be exemplified in the model used in Ahipara. Consequently, employing Landsat TM/ETM+ information from various periods' yields resembling outcomes, however a minute difference is reflected such as land cover conditions in the acquisition process.

2.6 Remote Sensing for Vegetation Mapping

Monitoring and analyzing the environmental changes on the Earth's surface is a crucial fundamental principle of global change research (Jang, Bartholome, & Viau, 2006; Lanbin, Turner, & Helmut, 2001). The survey, classifying and mapping of vegetation is an important baseline inventory for sustainable natural resources management (Lu & weng, 2007; Uluocha, 2003; Luque, 2000).

Satellite data provides valuable information for mapping vegetation and monitoring vegetation change (El-Mezouar, Taleb, Kpalma, & Ronsin, 2011; Peterson, 2008) through measuring and distinguishing vegetation land covers from a small region to worldwide scales using hyper or multispectral imagery (Govender, Dye, Weiersbye, Witkowski, & Ahmed, 2009). The main purpose of remote sensing is to map and monitor the planet earth's resources which is compared with traditional survey techniques, including field surveys, literature reviews, map interpretation and data analysis satellite remote sensing is accurate, timely and cost effective (Sivakumar, Morel, Bencherif, Baray, Baldy, Hauchecorne, & Rao, 2004; Jakomulska, Zagajewski, & Sobczak, 2003).

Applying remote sensing approaches to develop the land cover and land use classification mapping are becoming increasingly useful to detect and observe the large areas of agriculture, forestry, urban as well as it can be used to map submerged aquatic vegetation (SAV) in intertidal zone which is as a environmental indicator in marine or fresh water ecosystem (Olmanson, Bauer, & Brezonik, 2002; Ashraf et al., 2010; Langley, Cheshire, & Humes, 2001; Levin, Ben-Dor, & Singer, 2005).

The Landsat satellite series have been reportedly the largest history and the widely applied model in detecting and monitoring land use/cover so that with introducing Landsat Data Continuity Mission (LDCM) satellite (as known as the Landsat 8), the Landsat program have been observing the Earth's surface for 40 years (NASA, 2011).

As already mentioned in the first chapter, the satellite imagery was available for New-Zealand about in the early 1790s. According to MfE (2012), the national Land Cover Data Bases1 and 2 (LCDB1 and 2) programs have used the Spot 2 imagery data from 1996/1997

and the Landsat 7 ETM+ images from 2001/2002 to map land cover in New Zealand. New Zealand's land cover was classified in nine main categorizes by LCDB1 and LCDB2 datasets, including exotic forest, exotic shrubland, native forest, native vegetation, other native land cover, primarily horticulture, high-producing exotic grassland, low-producing exotic grassland and artificial surfaces. The database series classified land cover into different classes in the North Island (figure 2.7).
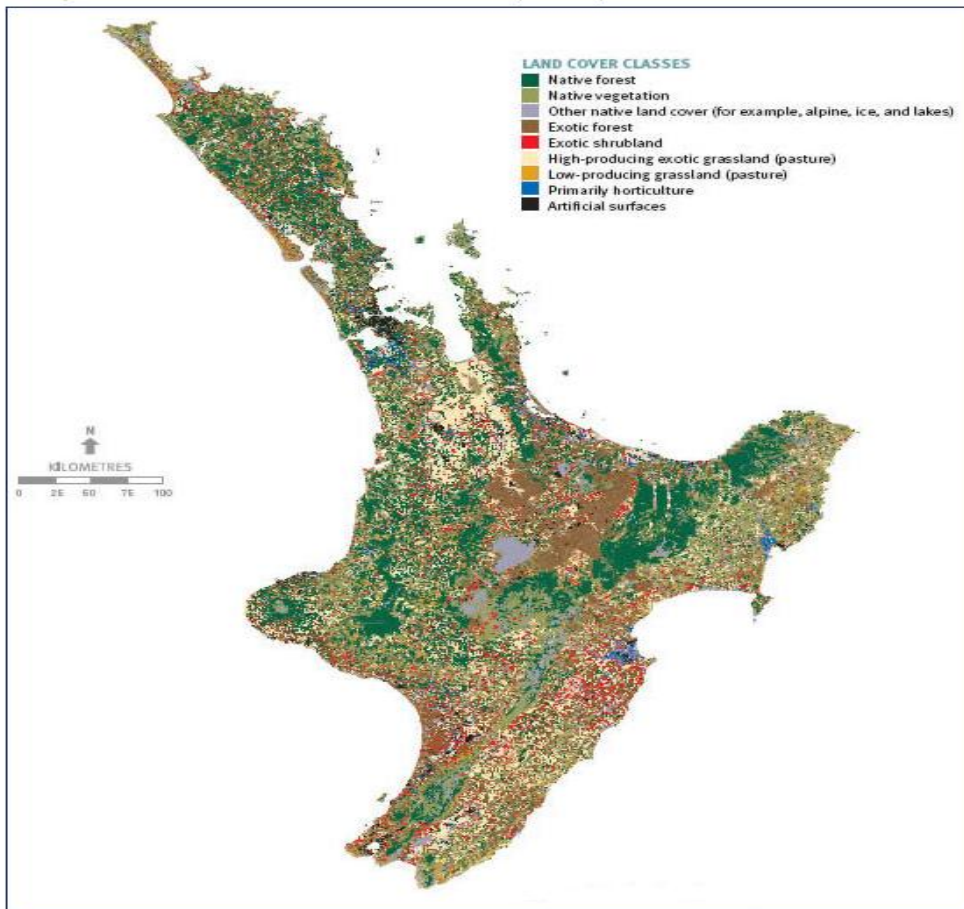
Figure 2.7 Northland land cover classification_LCDB2 (DoC, 2002)

2.6.1 Vegetation Extraction from Remote Sensing Imagery

Identifying, extraction and vegetation classification from remotely sensed data by interpreting satellite image is the main part of digital image processing which is derived from the analysis of land cover features, for instance, texture, shadow, pattern, shape and size, etc. there are different procedures that have been created to use for image processing. Supervised and unsupervised techniques may be used to classify the features extracted and they can be

proposed depending on whether the ground truth data are provided as ground control points or not.

The conventional steps of vegetation mapping comprise pre-processing of the image, classification and post processing of the data. All preliminary stages in an image processing needed to develop the quality of initial images acquired, so that every pixel of the image can be categorized into one of several land cover classes identified in a classification process (Jensen, 2005). Methods used for vegetation evaluation is distinguished in terms of subjective and objective. With each approach reported to have its own advantages over the other. However, the species analysis is reportedly the widely accepted objective model, with most literatures sighting that is deemed free all means of bias operators; however, the information obtained from this model has little significance until communities are separated for identification. RS creates the possibility of having better subjective approach where overriding species is accurately identified based on spectral characteristics of the area under study.

2.6.2 Land Cover and Land Use

Land cover assigns to some objects which cover the Earth's surface, such as water, soil, vegetation and urbanized area etc., in as much as land use assigns for some applied purposes including agriculture field, recreation and pasture area. Remote sensing data provides some useful and accurate information for investigators who working on both land cover and use (Al-Ahmadi & Hames, 2009).

Despite of all desires to land cover classification, there are some uncompromising parameters may affect the performance of the satellite imagery, such as atmospheric conditions (scattering and absorption), the variation of seasonality and the complexity of surface geometrics so that the land use determination process by remotely sensed data may produce insufficient information to apply land use classification.

2.7 Satellite Image Classification

Satellite images have layers, each layer comprise of special information defined under the satellite specification instructions. For example, when using the Landsat satellite images that

has special task in detecting weather patterns, the first layer may for instance contain information on water, the second layer report useful information on soil information and so forth. In fact, each of the layers has to be designed in a pixel matrix can be without difficulty converted to a matrix representing real number values (Richards & Watt, 2006). Matrices are created to store specified information that corresponds to identifiable terrain surface on the area under study. Hence, the superposition of the matrices provides desired surface features on the target area.
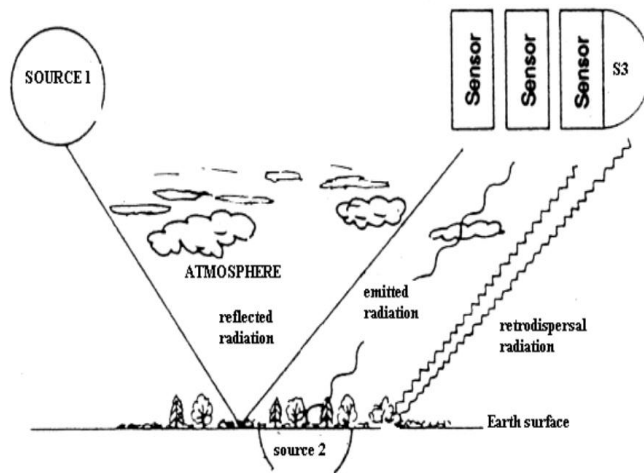
Figure 2.8 Satellite Image Classification through use of self-organized mapping on GRID Computing (Arias et al., 2009)

The figure above (2.8) illustrates a typical method to obtain soil and weather forecasting by use of satellite Image Landsat 7 (Arias, Gomez, Prieto, Boton, & Ramos, 2009).

2.7.1 Supervised and Unsupervised Classifications

It is common that some vagetation type have unlike spectral features as observed in remote sensed images. Similalry, different land surface types contains related spectra, this makes it very hard to achieve accurate classification results (Atmopawiro, 2004). In fact, this may result from use of either the conventional models of unsupervised classifications or from surpervised classification. Search for superior method presents a tough research topic considering all these methods that are utilized in modern times are derived from tradtional models.Thus, this is often used as the basis of classification hence, developing improving

methods usually focus on expanding specific techniques, which leads to enhanced classification results (Yichun, Zongyoa, & Mei, 2008).

2.7.1.1 Unsupervised Classification

a. This model is often applied while defining spectral class identifying images, where previous knowledge on the area under study.

b. Before the classification process, normalization process is used in while collecting the pixels that are readily available on the satellite image. However, only the agent pixels are stored.

In unsupervised classification, clusters of pixels are assigned based on statistically similar spectral response models. Every pixel in an image is matched up to a separate cluster to find out which set as being most similar to it and it is closest to. Colors are then determined to each class and the clusters are interpreted after classification based on information of the image or by ground-truthing.

2.7.1.2 Supervised Classification

Supervised classification method generates data from training dataset. In order to obtain the training data, the process involved collects several sources that are relevant in documentation and may include aerial photography and cartography among other classification models. The collected data has to be representing the area on research (Atmopawiro, 2004).

2.7.1.3 Parallelepiped Supervised Classification

Parallelepiped use uncomplicated decision rule in classifying multispectral data. The adopted decision creates n-dimension within the image data gap. This dimension lies above the lower band and beneath the higher band for all specified n-bands that are to be classified (Richards & Jia, 2006). The statistical modeling is essential in synthetic aperture radar (SAR) image analysis. It provides technical support, which is important for creating a comprehensive

terrain scattering mechanism necessary in developing algorithms to effectively interpret images and help in accurate image simulation.

2.7.1.4 Maximum Likelihood Classification

An elaborate likelihood classification method in handling remotely sensed image is often suggested, it helps in reducing the processing time associated with traditional maximum likelihood when applied to imaging spectrometer data, similarly it important since it aids in coping with preparation of the geographical small clauses. In addition, there are great benefits of large number of spectral per partial, which are presents available data kept through imaging spectrometers such as the AVIRIS. This helps in developing a full reflectance spectrum for an identified ground region whose features can be easily distinguished (Richards & Watt, 2006). To easily interpret images by using features as identified in the spectral, the basis have to either be drawn from theoretical approaches or develop a library based searching model.

However, in cased the identified techniques are absent recourse is still needed to create more conventional approach, for example, the supervised classification on the basis of maximum likelihood methods, this model however, was used in the past and proved a success approach especially in areas where partial number of bands is applied. The maximum likelihood classification is based on assumption considered that the probability distribution for each spectral class is of essence and forms the multivariate a normal model with dimensions that equal the number of spectral bands(Atmopawiro, 2004).

2.8 Remotely Sensed Data Processing

Pre-processing of satellite images proceeding to feature extraction is essential to detect and eliminate noise and error and enhance accuracy in image classification. It can be particularly considered when a time series of images acquired to be applied to enhance recognition accuracy. After doing pre-processing techniques on a time series images the result will be obtained as the data acquired by the similar satellite sensor (Hall, Strebel, & Nickeson, 1991). It can be remembered that the pre-processing methods should not be constantly required, so that some of these procedures might be done by data supplier companies. Therefore, it is

suggested to discuss with the data supplier and find out about the level of data product which is required (0, 1A, 1B, 2A, 2B, 3A, 3B the product quality improved step by step) before obtaining the data. For example, in this project, the different type and sources of the data were obtained, including the RapidEye and the Landsat 7 (ETM+) which level 3A product of the RapidEye imagery has been used. According to the RapidEye supplier company, there are some standard image products which are offered at two different levels to hold up the various requests of the user: 1. RapidEye Basic (Level 1B) products are sensor level products with a minimum quantity of processing (geometrically uncorrected) for user who like better to geo-correct the images themselves; and 2. RapidEye Ortho (Level 3A) are orthorectified products with radiometric, geometric and terrain corrections in a map projection (RapidEye, 2012).

2.8.1 Radiometric Normalization of Multi-Temporal Data

Remote sensing is very significant primarily in the study of environmental dynamics and is widely established by the geospatial community. On this event, remote sensing has become a vital tool in detection of spectral changes affiliated with phenomenon such as land cover and utilization. Landsat has progressively provided a global land surface imagery change since 1972, with depicts the main persistent archive of land history. Spatial harmonization and chronological resolution of large spatial areas have relevant developed quantity and quality of satellite data imagery, which play a significant role in environmental monitoring. Initial processing shortcomings of multispectral satellite information as the core information on the study of land cover within Ahipara persist because of errors due to noise, environmental situations and radiometric and geometric alterations, which are initiated during data attainment and transmission stages (Canty, Nielsen, & Schmidt, 2004).

Various methodologies are employed in radiometric normalization and multispectral analysis of imagery acquired from satellite and can be either absolute or relative. Absolute techniques are less feasible because it is only relevant when a measure of optical properties of the atmosphere taken into consideration in situ and concurrently with the scene recording moment. On the other hand, a relative techniques progresses under the assumption that the affiliation flanked by the at-sensor radiances taken into account at two varying periods from spatial regions of persistent reflectance within Ahipara. This is spatially homogenous and is capable of being estimated by linear functions. The difficulty faced by each technique is the

establishment of appropriate time-invariant features for the basis of normalization (Du & Teillet, 2002).

2.8.1.1 Conversion to Top of Atmosphere Reflectance Units

This is a normalization process, significant in creation of multi-temporal or multispectral mosaics. This is because largely it eradicates inconsistencies between images because of sensor discrepancies, proximity of the sun, earth, and zenith solar angle. The procedure involves two steps: first is characterized by the conversion of measured DN to radiance utilizing in-flight sensor facets. The facets are provided in combination with imagery established from comparisons of in-flight calibration basis in conjunction with pre-flight values of absolute radiance. Radiometric comeback function for every band could probably be established and used practical for normalization of temporal radiometric variations between sensors (Freeman, Chapman, & Siqueira, 2002). Band equation can be given by:

L = Gain × DN + Bias ……………………..eqn: 1

Legend:

L	=	spectral radiance measured over spectral bandwidth of a channel
DN	=	digital number value recorded
Gain	=	$(L_{max} - L_{min})/255$
	=	slope of response function
Bias	=	L_{min}
	=	intercept of response function
L_{max}	=	radiance measured at detector saturation in $mWcm^{-2}sr^{-1}$
L_{min}	=	lowest radiance measured by detector in $mWcm^{-2}sr^{-1}$

Source: (Guyot, 1994)

Secondly: this involves the calculation of TOA (Top of Atmosphere) reflectance for each explicit band. Equation ii used, which corrects illumination differences in and between scenes. This method of correction is applied to each pixel because each scene is in each era and the impacting reflectance is usually scaled to 8-bit data assortment (Guyot & Gu,1994).

.

$\rho_\lambda = (\pi d^d L_\lambda) / (E_{0\lambda} \cos \phi_s)$…………………….. eqn: ii

ρ_λ =   reflectance as a function of bandwidth

d   =   Earth-sun distance correction

L_λ =   radiance as a function of bandwidth

$E_{0\lambda}$ =   exoatmospheric irradiance

θ_s =   solar zenith angle

Source: (Guyot, 1994)

2.8.2 Rectification of Remotely Sensed Data

2.8.2.1 Geometric Correction Approaches

This approach involves modeling the affiliation between the image and ground coordinate systems. This involves non-logical and logical geometric errors that are prone to satellite images (Lillesand et al., 2004). For instance, systematic errors present in Landsat imagery are usually well documeted and are mainly utilities of scan skew, mirror scan speed, panoramic alteration, platform speed, perspective and diurnal motion of the earth (Mather, 1999). Sensor based data charaterstics are modelled then applied to raw satellite image as part of the logical correction that is done by Landsat base station. Non-logocal errors are usually as a result of varition through time in the spatial position and inclination angle of the platform. In absence of accurate sensor platform orientation facets this distortion can only be rectified through image-to-map correction averts (Mather, 1999).

2.8.2.2 Image to Image Rectification

Image to image rectification is a significant methodology in obtaining a fast representation of structuring facades and acquiring measurements directly from rectified frames. Conversely, this techniques is irrelevant when the façades does not entail various plane surfaces, hence the number of measure to be take becomes hurriedly significant and needs thorough topographic survey. Therefore, this method involves the matching of one image to another; on this case, one geographic area is coincidentally positioned in respect to a similar geographic area (Figure 2.9). The techniques is applied when it is not important to each pixel having a unique address that is x, y coordinate in a projection (Lillesand et al., 2004).

a. *Rectified* Landsat TM band 4 image of
Charleston, SC, obtained on November 9, 1982.

b. Unrectified Landsat TM band 4 image
obtained on October 14, 1987.
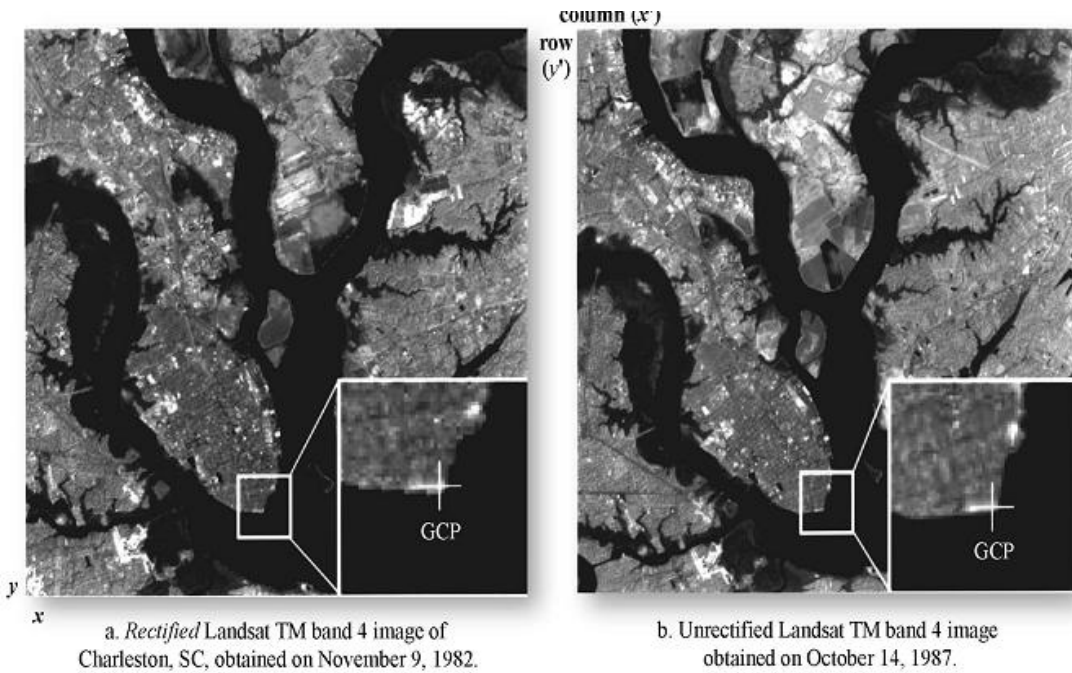
a) Previously rectified TM data with b) Unrectified TM data to be registered to the
rectified 1982 Landsat scene.

Figure 2.9 Image rectifications (Mather, 1999)

2.8.2.3 Image to Map Rectification

This is a rectification procedure, which involves making of the satellite imagery geometry
plan metric. This technique is not 100% reliable in eradication of alteration caused by relief
displacement of satellite images (Jensen, 2005). The method involves the selection of Ground
control point (GCP) image unit element, coordinates in conjunction with their map coordinate
(Figure 2.10).
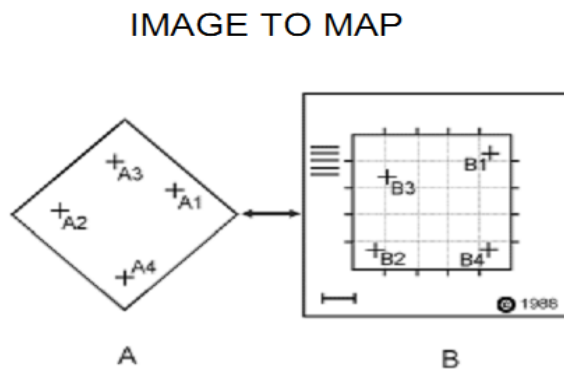
Figure 2.10 Image to map rectification (Jenson, 2005)

2.9 Area of Study (Ahipara, Kaitaia in New Zealand)

Ahipara Ecological District situated on the West coast of the North Island and south of the Kaitaia. It stretches from Tauoa point in the North to Warawaraw forest and Herekino Harbour in the South. This region is connected to Aupouri area in the North, Maungataniwha forest in the East and Hokianga Harbour in the South. This area covers about 27,762 ha, among this land cover 88% comprise natural areas as illustrated. A large area of this ecological district is in a natural or semi-natural condition, including the vast areas under the indigenous vegetation cover for example, kauri forest, broadleaf-podocarps and forests, conifer-broadleaf forests, gumland shrubland, and coastal riparian habitat. The land-cover of this area is described as 71% forest, 22.3% shrubland, 5.6% duneland, and less than 1% wetland (Conning, 1998).

The comprehensive ecological surveys were undertaken by the Department of Conservation from 1994 to 1996. This information is also available on national existing database.
The region is associated with volcanic massifs with steep escarpments and gullies as well as far-reaching wild coastline. Ahipara region has a diversity of vegetation types and plant species. These include some nationally rare kinds of species for example gumlands, dunelands and mature kauri forests, providing the region with distinctive species.
Land use and land cover is a significant component in understanding relations of human activities with the environment, hence necessary to simulate the identified changes, empirical studies have been observation and reveal change in terms of land use/ cover classification. This paper points out different land classification models employed in the study identifying changes in terms of land use/cover in Ahipara region in Kaitaia, New Zealand (DoC, 2009). A region that is extremely rich in biodiversity which has approximately 80,000 diverse species including native animals and plants among others.

The region is legally protected conservation is one of the method that is adopted in order to preserve biodiversity as well as its services. The New Zealand's legally protected land includes land that is protected by the Department of Conservation and regional council and so forth.

Location of Ahipara Ecological District
(Brook 1996)

⊠ Ahipara ED

2.01: Te Paki
2.02: Aupouri
5.01: Maungataniwha
3.01: Whangaroa
3.03: Puketi
3.02: Kerikeri
3.05: Whangaruru
5.02: Ahipara
3.06: Whangarei
4.01: Poor Knights
3.04: Kaikohe
5.03: Hokianga
5.05: Tangihua
3.07: Manaia
5.04: Tutamoe
3.08: Taranga
3.09: Waipu
9.01: Rodney (part)
6.01: Tokatoka
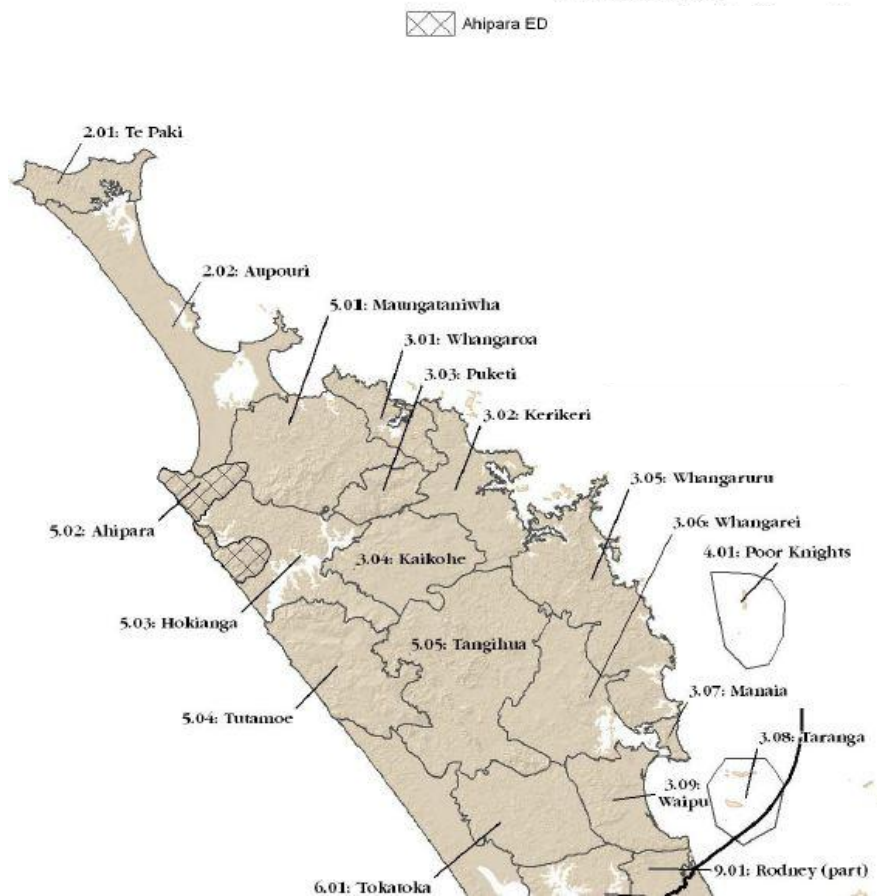
Figure 2.11 The Ahipara Ecological Distric (Doc, 1998).

Recent New Zealand Land Classification Situation by 2009, about 8,763,300 ha of this country was legally protected with the primary purpose being preservation of biodiversity. Of the total protected area, 8,401,500 ha cover native land including land with vegetation. However, the non-vegetative cover for example areas with permanent snow, waterways, regions covered with alpine gravel as well as regions covered with rocks and ice. During this time, the legally conserved public land accounted for 8,525,000 ha, an estimated increase of 4.7% (386,500 ha), this is in contrasted the legally conserved private land accounted 238,300 ha. The figure below clearly identifies the legally protected areas by 2009.

2.9.1 Land Cover Type in Ahipara Region

There are some different types of habitat in Ahipara:

Sand dunes

The Ahipara region contains a large area of comparatively dune-lands leftover in New-Zealand, with huge parts of open sand. The front dunes are covered by Spinifex, Knobby and Pingao. Some other species, like Marram,and Kikuyu can be found.

Wetland

The wetlands include:

o Duneland wetlands, the Tauroa Point Swamp consisting Raupo with sphecelata

o Valley wetlands of raupo with Baumea articulate and irregular cabbage tree, surrounded by manuka

o Coastal seeps, it consist of jointed rush, knobby clubrush, huge umbrella sedge some having Euphorbia glauca.

o Sedge-herb that is associated with sand flats closer to the stream mouths. They include Myriophyllum votschii, Triglochin striata and Lilaeopsis novae-zealandiae (MfE, 2010).

Coastal margins

In this area, the most ordinary vegetation cover types are: Taupata, Tauhinu, the native iceplant, the coastal tussock and brake fern.

Coastal shrubland

The low height manuka is a dominated habitat of shrubland vegetation, and also coastal toetoe, cabbage tree with occasional flax should be discovered. Moreover, Kanuka with Kowhai, landcewood can be appeared on the dunelands' edge.

Coastal forest

In this zone, manuka and kanuka are the most dominated species with rewarewa, mangeao and the other regionally adapted vegetations.

2.9.2 Legally Preserved Native Land Cover in Ahipara (New Zealand)

Most of lands under legal conservation for purposes include public conservation lands under control of the Department of Conservation (DoC), regional parks maintained by authorities and private land conserved under the covenant by QEII National trust.
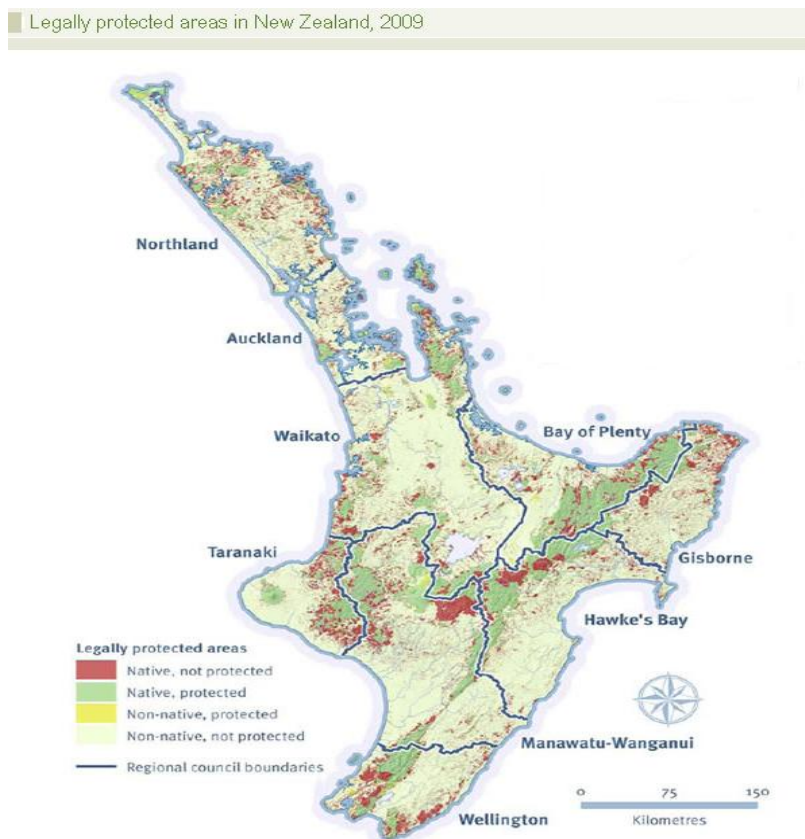
Figure 2.12 Legally protected area(DoC, 2010).

At the end of 2004, 8.06 million hectares preserved in New Zealand, this was specifically set aside for public conserved land. Another study report conducted on October 2007 a total of 8.4M hectares reported to be under legal protection, an increase of about 4.56%. In 2007, approximately 82,933 ha were legally protected through the National Trust Covenants (QEII). This was reported to be an increase since its introduction in 1977.

Chapter 3

Material and Methods

Methodology

The project's research methodology included data preparation and pre-processing, object-based classification, manual revision, accuracy assessment, and landscape analysis. The methodology adapted to conduct this research project is indicated in the flowchart diagram illustrated below in detail:
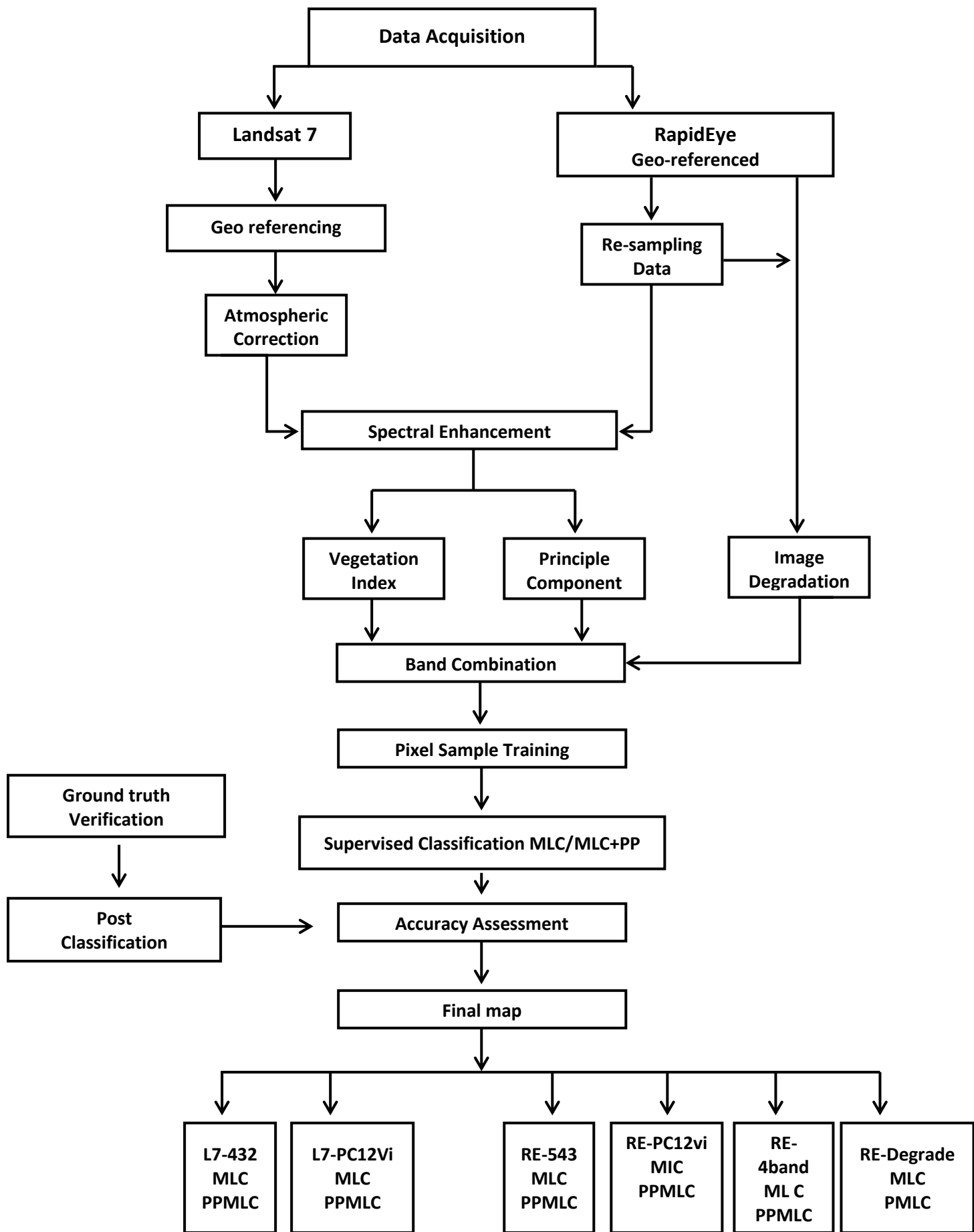
Figure 3.1The flowchart indicating image processing methods and stages.

3.1 Study Area and Satellite Data

3.1.1 Study Area

The study area considered in this project is located from the Ahipara Bay (35º 8' 6" S, 173º 10' 7" E) to Herekino Harbour (35º 22' 26" S, 173º 12' 52" E) in the Western part of New Zealand's North Island. The Landsat7 data was acquired over this area under cloud free condition on 3rd June 2001 (Figure3.2) whereas the RapidEye data was captured on 8th Dec 2010 which their original specifications are listed in table 3.1.

For each of both the ortho-rectification and geo-referencing was done in Universal Transverse Mercator (UTM) zone 59 S with a WGS 84 spheroid, WGS 84 datum.
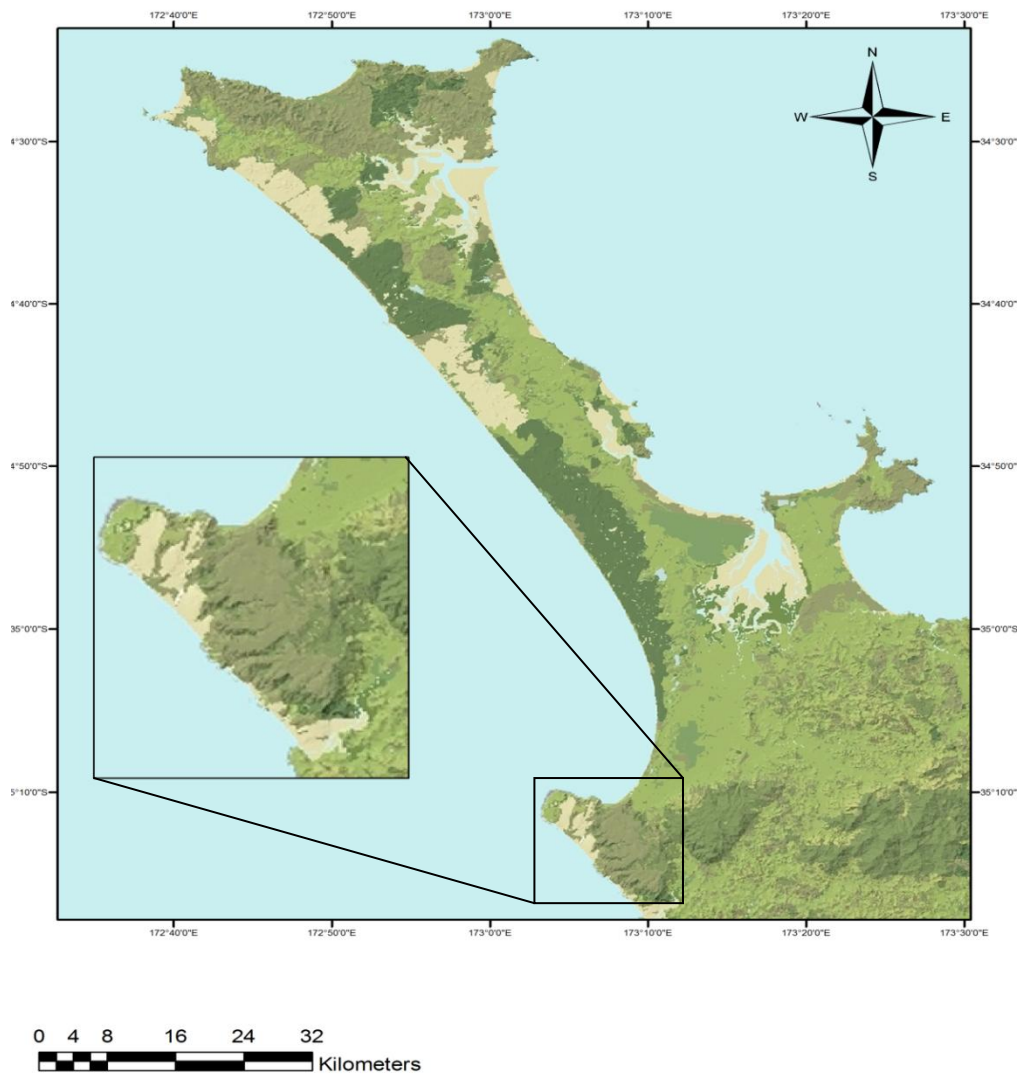
Figure 3.2 Location of the study site, Ahipara region, Northland (Koordinates, n.d.)

3.1.2 Landsat7 Imagery

Landsat7 Enhanced Thematic Mapper Plus (ETM+) image (Path: 075 and Row: 084) with 28.5 m spatial resolution which included eight channels ranging from 1 through 7 multispectral bands (blue, green, red, NIR, 2 x MIR and thermal infrared) and 15 m panchromatic band, was used to perform land cover classification (Figure 3.3 and Table 3.1). For this study, thermal band was excluded due to its low spatial resolution (60 m). The Landsat ETM+ imagery was obtained from the Global Land Cover Facility (GLCF) through the URL: http://glcfapp.glcf.umd.edu:8080/esdi/index.jsp
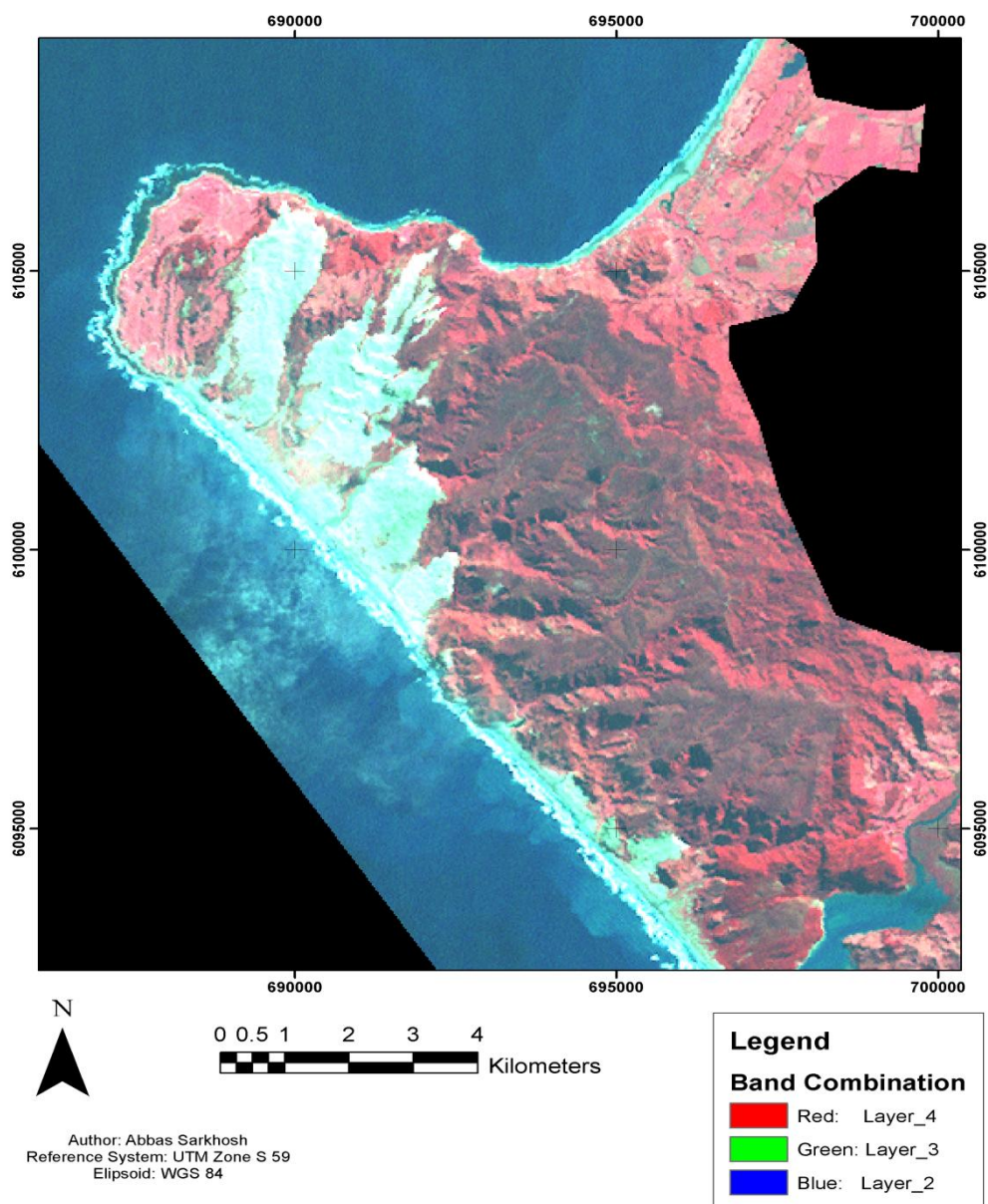
Figure 3.3 Subset of Landsat ETM+ image, Ahipara region

3.1.3 RapidEye Imagery

The high resolution RapidEye multispectral image data was acquired (Figure 3.4) with spatial resolution of 6.5 m (5m_ orthorectified). Its multispectral sensor captures image in 5 spectral bands, including three standard bands (blue, green, red) in the visible part of electromagnetic spectrum as well as 2 further bands in near infrared (NIR) and "red edge" parts of the spectrum. The red edge band is sensitive to transformations in chlorophyll content, and appears for the first time in a commercial satellite. The RapidEye imagery was ordered from RapidEye AG German Company.
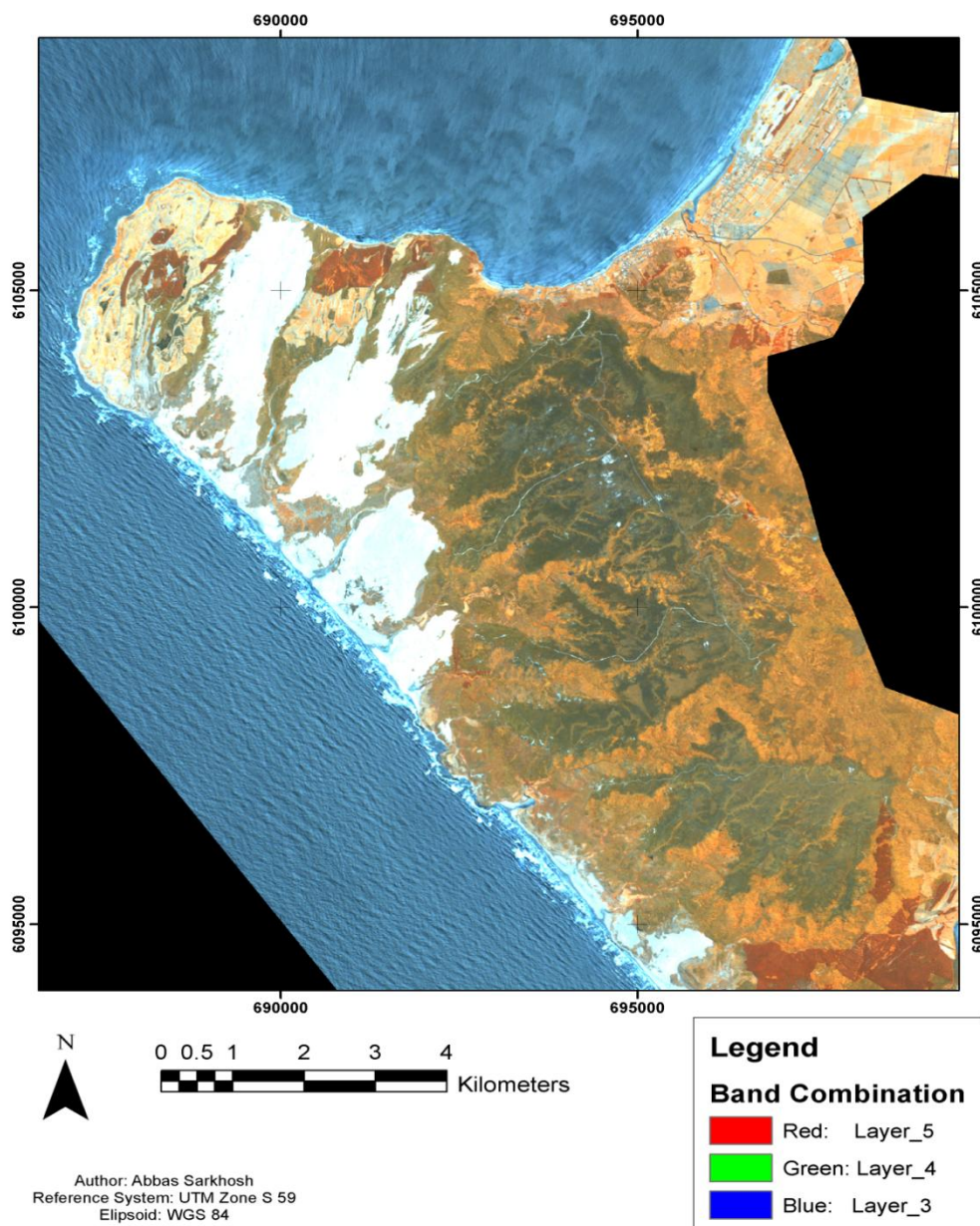
Figure 3.4 Subset of RapidEye image, Ahipara region

Table 3.1 RapidEye and ETM+ specifications (NASA, 2012)

| Band | RapidEye Sensor | | ETM + Sensor | |
	Spectral Range (μm)	Resolution (m)	Spectral Range (μm)	Resolution (m)
1	0.44 - 0.51	5	0.45 - 0.51	30
2	0.52 - 0.59	5	0.53 - 0.60	30
3	0.63 - 0.59	5	0.63 - 0.69	30
4	0.690 - 0.73	5	0.75 - 0.90	30
5	0.76 - 0.85	5	1.55 - 1.75	30
6	-	-	10.40 - 12.50	60
7	-	-	2.09 - 2.35	30
(Panchromatic)		-	0.52 - 0.90	15

Source: NASA 2012

3.2 Land Use and Land Cover Classification Analysis

Satellite image classification is the method of discriminating pixels, which are created in several spectral bands inside a digital image acquired. The procedure generates groups of pixels with similar spectral characteristics into the same categories (Campbell, 2002). The method can be implemented by unsupervised or supervised approaches which are broadly applied for a variety of purposes (Boyle et al., 1998; Campbell, 2002; Formard, Vega, & Proisy, 2004; Lillesand et al., 2004; Jensen, 2005; Carreiras, Pereira, & Shimabukuro, 2006; Lu &Weng, 2007). In this study, a supervised classification method with different type of algorithms, including maximum likelihood and parallelepiped mixed with maximum likelihood were used to classify remotely sensed data of Landsat ETM+ and RapidEye over the Ahipara region. As the image processing steps have been indicated in the flowchart (Figure 3.1), for an accurate comparative study between L7 and RE images, it is required to have different images for each of them to compare the results of the accuracy assessment of classified data, including an image with 4 bands of multispectral of RapidEye imagery (after removing the Red-edge band (B5)) the same as the false colour infrared image of Landsat7 (combination of 4,3 and 2bands) and also a degraded image of RE from 5m to 30m, the same spatial resolution of L7.

After applying some pre-processing techniques, the following approaches have been employed to achieve the final desired results of this project.

3.3 Data Processing

Erdas Imagine application was utilized to process the remotely sensed data. First of all, the layer stack function was used to stack bands 1, 2, 3, 4, 5, 7 for ETM+ image. The seven scenes of RE required data were mosaiced together, then both images, the layer stacked of L7 and mosaiced of RE images were subset to produce a dataset of the study area, and the next step the geometric registration was conducted using image to image registration for both datasets.

3.3.1 Conversion to Radiance and Top of Atmosphere (ToA) Reflectance

In this step, the radiometric correction was applied for conversion of the measured multispectral brightness values to top of atmosphere (ToA) reflectance units. This normalization technique is important to remove or reduce the differentiations in the Earth-Sun distance, solar zenith angle or scene dates, this process involved conversion of rescaled DN to radiance by using the ETM+ sensor calibration parameters (Guyot & Gu,1994). The following equations were used to convert DN to radiance units:

Lλ = Gain * DN + Bias

where: L = spectral radiance measured over spectral bandwidth of a channel

DN   =   digital number value recorded

Gain = $(Lmax – Lmin)/255$

Bias   =   *Lmin*

         =   intercept of response function

Lmax =   radiance measured at detector saturation in *mWcm-2sr-1*

Lmin =   lowest radiance measured by detector in *mWcm-2sr-1*

The second equation that was used for the process:

$$L_\lambda = ((LMAX_\lambda - LMIN_\lambda)/(QCALMAX-QCALMIN)) * (QCAL-QCALMIN) + LMIN_\lambda$$

where: L_λ = Spectral Radiance at the sensor's aperture in watts/(meter squared * ster * μm)

Grescale = Rescaled gain (the data product "gain" contained in the Level 1 product header or ancillary data record) in watts/(meter squared * ster * μm)/DN

Brescale = Rescaled bias (the data product "offset" contained in the Level 1 product header or ancillary data record) in watts/(meter squared * ster * μm)

QCAL = the quantized calibrated pixel value in DN

LMIN$_\lambda$ = the spectral radiance that is scaled to QCALMIN in watts/(meter squared * ster * μm)

LMAX$_\lambda$ = the spectral radiance that is scaled to QCALMAX in watts/(meter squared * ster * μm)

QCALMIN = the minimum quantized calibrated pixel value (corresponding to LMIN$_\lambda$) in DN
= 1 for LPGS products
= 1 for NLAPS products processed after 4/4/2004
= 0 for NLAPS products processed before 4/5/2004

QCALMAX = the maximum quantized calibrated pixel value (corresponding to LMAX$_\lambda$) in DN
= 255

The next step was performed by calculating the atmosphere reflectance for band 1, 2, 3, 4, 5 and band 7 by applying the equation 3. The correction was used on a pixel by pixel and the output reflectance values measured to a float single data range.

According to equation 2:

(191.600 - - 6200) / (255 - 1) * (L7band1_nn10 - 1) + (- 6.200)

(196.500 - - 6.400) / (255 - 1) * (L7band2 _nn20 - 1) + (- 6.400)

(234.400 - - 5.000) / (255 - 1) * (L7band3 _nn30 - 1) + (- 5.00)

(157.400 - - 5.100) / (255 - 1) * (L7band4 _nn40 - 1) + (- 5.100)

(31.060 - - 1.000) / (255 - 1) * (L7band5 _nn50 - 1) + (- 1.000)

(10.800 - - 0.350) / (255 - 1) * (L7band7 _nn70 - 1) + (- 0.350)

Equation 3:

$$\rho_p = \frac{\pi * L\lambda * d^2}{ESUN\lambda * COS\theta S}$$

Where:

ρ_p = Unitless planetary reflectance

L_λ = Spectral radiance at the sensor's aperture

d = Earth-Sun distance in astronomical units

$ESUN$ = Mean solar exoatmospheric irradiances from Table 3.2

θS = Solar zenith angle in degrees

Table 3.2 L7 ETM+ Solar Spectral Irradiances

ETM+ Band	watts/(meter squared * µm)
1	1997
2	1812
3	1533
4	1039
5	230.8
7	84.90

According to the equation 3:

3.14 * \$n1_rad_band1 * (1.01433 * 1.01433) / (1997 * COS(24.1170033))

3.14 * \$n1_rad_band2 * (1.01433 * 1.01433) / (1812 * COS(24.1170033))

3.14 * \$n1_rad_band3 * (1.01433 * 1.01433) / (1533 * COS(24.1170033))

3.14 * \$n1_rad_band4 * (1.01433 * 1.01433) / (1039 * COS(24.1170033))

3.14 * \$n1_rad_band5 * (1.01433 * 1.01433) / (230.8 * COS(24.1170033))

3.14 * \$n1_rad_band7 * (1.01433 * 1.01433) / (84.90 * COS(24.1170033))

3.3.2 Principal Component Analysis

Principal Component Analysis (PCA) is a statistical method which is utilized to compress and transform the original multispectral data bands (they are highly correlated) to uncorrelated output bands as the new principal components axes before using the classification methods with a minimum loss of information (Yuan, Elvidge, & Lunetta, 1998; Lillesand et al., 2004).

By applying PCA approach, the results of land cover classification may improve (Tso et al., 2009). It can increase the segregation land cover in terms of changed and unchanged after used to multi-temporal data (Li et al., 2005; Yuan et al., 1998).

There are two types of PCA, including the procedure which is considered as a standardized PCA when the statistical transformation for the data density is achieved depend on the correlation matrix of the original bands (Yuan et al., 1998), and the second method of PCA that is recognized as unstandardized, can be performed when the variance-covariance matrix is utilized (Tso et al., 2009).

The number of components created in the process is equal to that of the input bands; nevertheless, the first PC band includes the largest part of entire data variance detected in the original dataset. The second PC band has the second highest data variance and the following bands are uncorrelated and orthogonal with the minimum values of variance, thus the final components have a few amount of the data variance (Tso et al., 2009; Richards & Watt, 2006). Therefore, the first two PC bands (1and 2) generally represent spectral data which is the same as along with input bands, whereas the following bands contain the least percentage of data variance which is uncorrelated to the data pattern from the first and second components. The eigenvalue indicate the amount of variance for each component's account (Rogerson, 2001). By applying a PCA plot, it will be possible to recognize which PC bands could represent the multispectral original datasets, so that the maximum amount of eigenvalue for a component can be represented the largest value of variance in the original data.

Principal component analysis was perform to bands 1, 2, 3, 4, 5 and 7 of the Landsat image to reduce the original datasets and calculate the components 1 and 2 for further investigation (Table 3.3). After applying PCA and as it is represented in the scree plot (Figure 3.5) and Table 3.4, the maximum amount eigenvalues and variances were observed for the components band 1 and 2, hence the components 3, 4, 5 and 6 were removed.

Table 3.3 Statistics from the principal component (PC) rotations performed on Lansat7 imagery.

Component	1	2	3	4	5	6
Band 1	0.509826	-0.556873	-0.365435	0.410735	-0.037629	-0.355398
Band 2	0.396341	-0.315202	-0.004507	-0.198295	0.186698	0.818147
Band 3	0.353756	-0.206459	0.427728	-0.694290	-0.045820	-0.406378
Band 4	0.535088	0.667097	-0.451633	-0.186440	-0.172688	-0.010477
Band 5	0.348669	0.312853	0.476494	0.391662	0.625580	-0.093580
Band 6	0.223515	0.070845	0.502461	0.348969	-0.735158	0.174122

Table 3.4The eigenvalues and variances of PCA calculated from Landsat7 imagery

Component	Eignvalue	% Variance	% Accumulative
B1	1998.109	84.758249	84.75
B2	275.467	11.685116	96.45
B3	63.319	2.685926	99.13
B4	17.686	0.750212	99.88
B5	1.671	0.070895	99.95
B6	1.169	0.049608	100
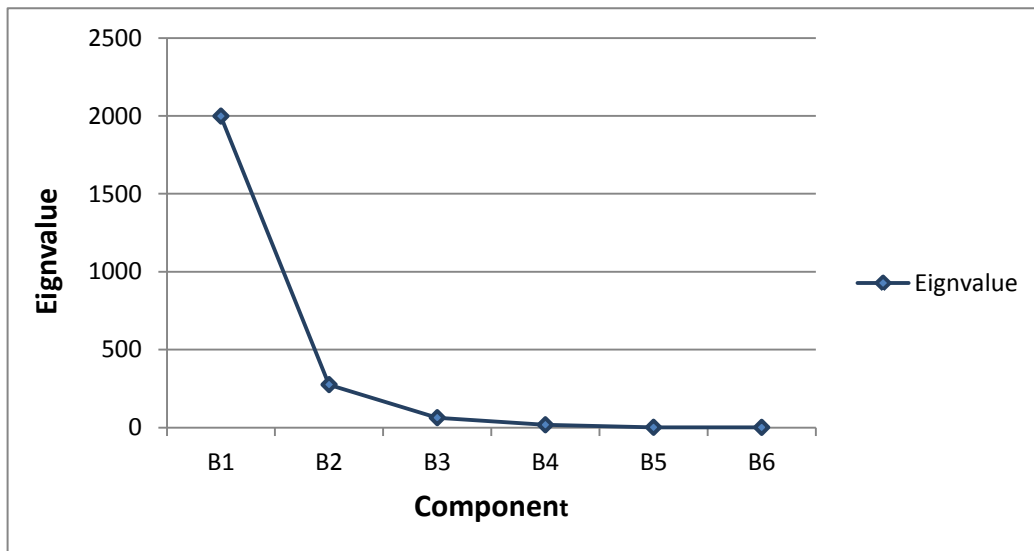
Figure 3.5The Scree Plot of eigenvalue of the PCA transformation (Landsat7)

For the next step, PCA was utilized to band 1, 2, 3, 4 and 5 of the RapidEye dataset to produce components 1 and 2 as the input data for combining with vegetation index layer and applying supervised classification (Table 3.5).

Table 3.5 Statistics from the principal component (PC) rotations performed on RapidEye imagery

Component	1	2	3	4	5
Band 1	0.543320	-0.403664	-0.567220	0.468617	0.227594
Band 2	0.496319	-0.242586	-0.040315	-0.830042	-0.064988
Band 3	0.380837	-0.215390	0.717225	0.216913	0.497099
Band 4	0.364671	0.183116	0.360404	0.210602	-0.811935
Band 5	0.424792	0.835633	-0.179814	-0.004831	0.298181

As the Table 3.6 is shown, more than 98 percent of the variance of the 5 bands data are belong to components 1 and 2, and also the components 3, 4 and 5 were discarded based on the least amount of eigenvalues for those bands (Figure 3.6).

Table 3.6 The eigenvalues and variances of PCA calculated from RapidEye imagery

Component	Eigenvalue	% Variance	% Accumulative
B1	69294867.812	87.386820	87.37
B2	8479516.245	10.693403	98.08
B3	1335774.865	1.684528	99.77
B4	147976.867	0.186612	99.95
B5	38567.877	0.048637	100
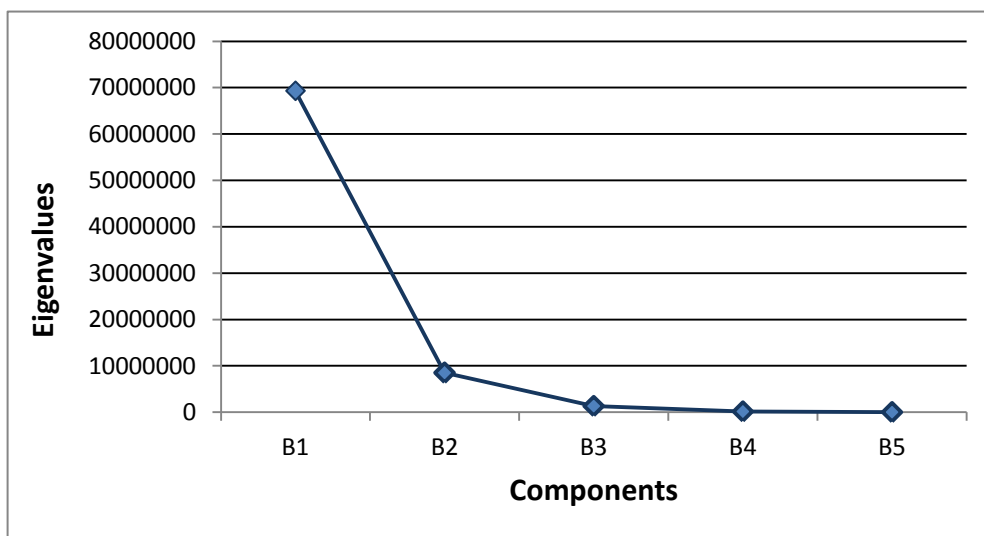
Figure 3.6 The scree plot of eigenvalue of the PCA transformation (RapidEye)

3.3.3 Band Combination

There is some type of layer combinations to discriminate different features on the ground thus the best band combination can be developed for image visualization and an effective supervised classification. For instance, the image for Landsat ETM+ can be displayed with combination of bands 4 (NIR), 3 (Red) and 2(Green) as the standard false colour RGB composite which commonly utilized for vegetation studies and crop growth monitoring. Furthermore, a combination of 4, 5, and 3 (NIR, MIR and Red) can distinguish the level of moisture in the soil or vegetation (NASA, 2011).

For this project, some experiments were done using a variety of band combinations to display and classify Landsat 7 and RapidEye images. As a consequence, the combination of bands 4, 3 and 2 as the standard false colour composite (CIR image) (Figure 3.7) and combination of bands PC1, PC2 and VI as the Principal Component layers (PCs) with combination of the Vegetation Index layer (VI) (Figure 3.8) were selected and applied in the Landsat7 imagery. In addition, from RapidEye imagery the combination of bands 5, 4 and 3 (Figure 3.9, also the combination of PC1, PC2 layers as the Principal Components (PCs) and the Vegetation Index (VI) layer (PC1, PC2, VI) were used (Figure 3.10) to demonstrate classification methods.

The two first principal components (PC1 and PC2) were chosen based on the results of the scree plot and assessment for 98.08 percent of the spectral variance of the original 5-band dataset from RapidEye imagery (Figure 3.6 and Table 3.6) and also the vegetation index (VI) was combined to create a new combination of three layers with the purpose of considering the vegetation distribution. In addition, according to the results of the principal components analysis of Landsat7 ETM+ data, 96.45 percent of the spectral variance of the original 7-band dataset is represented in PC1 and PC2 (Figure 3.5 and Table 3.4). Based on these results, PC1 and PC2 were selected to be added with VI layer for creating a new bands combination.

Figure 3.7 False Colour Infrared (CIR-LandSat7)
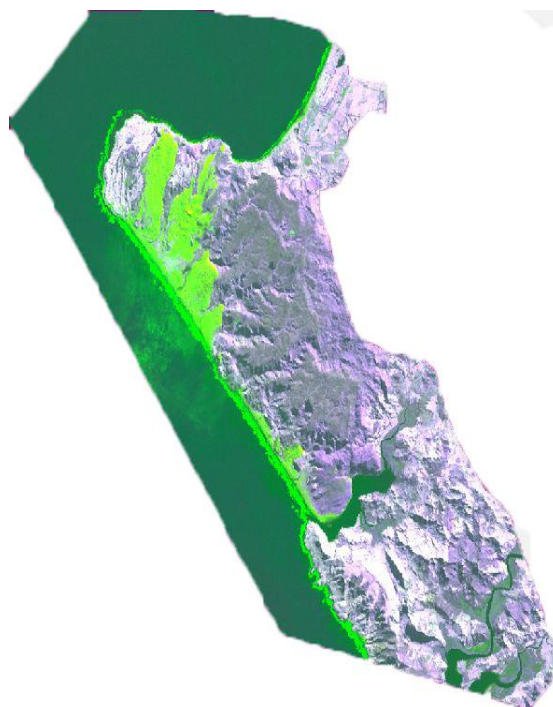
Figure 3.8 PCs and VI Band Combination (ETM+)

Figure 3.9RapidEye 543 (Band Combination)
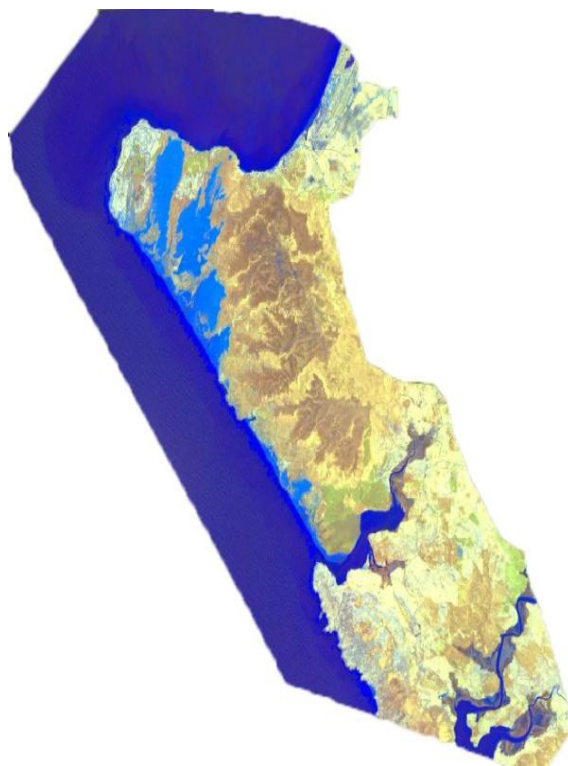
Figure 3.10 PCs and VI combination (RapidEye)

3.3.4 Image Classification Methods

There are many different procedures have been developed to execute supervised classification, the Maximum Likelihood classifier (MLC) method is still one of the most commonly applied supervised classification approaches (Jensen, 2005). Moreover, it is recognized that Parallelepiped classifier (PPC) algorithm can generate the most accurate classification due to its traditional assessment rule although it might abandon large parts in data space and create more unassigned pixels in the image (Campbell, 2002). For this research, Maximum Likelihood (MLC) separately and also a combination of Parallelepiped and Maximum likelihood (PPMLC) classifiers were used for land-cover classification.

3.3.4.1 Supervised Classification

ERDAS IMAGINE software was used to perform image processing functions required to complete the land cover classification. In this method, user has to define the training areas. The specific area of interest (AOI) from the all land cover types in the image was extracted.

The process was done, including:

- The clustering algorithms were used which define the spectral classes from the image.

- The area of interests was selected to assign information classes to the clusters.

- Applying statistics distance approach to evaluate the selected clusters. In this stage after assessment results, some clusters should be merged or deleted.

- At the end, the spectral subclasses were grouped into eleven actual informational categories that were included in Table 3.7. The categories are based on 2001 and 2002 land cover databases version 2 (LCDB2), and then a supervised classification using maximum likelihood (MLC) algorithm and a combination of parallelepiped (PP) with MLC were utilized to produce a thematic image with classified spectral classes.

Table 3.7 land cover categories

Code	Class Name
0	No data
1	Water
2	Mangrove
3	Shallow water
4	Low Producing Grassland
5	Indigenous Forest
6	Coastal Sand and Gravel
7	Manuka/Kanuka
8	Pine Forest
9	Shrubland
10	Grassland
11	Wave

3.3.5 Classification Accuracy Assessment

Accuracy assessment is a crucial part of image classification process, which evaluates the level of agreement between reference and classified data (Tso & Olsen, 2005). The accuracy can be assessed by an error matrix. The error matrices introduce the quality of correctly or incorrectly classified images for each which they would be compared to a reference data. This reference data is taken from different sources, including high resolution satellite image, field survey (ground-truthing), aerial photograph or an existing map. At the end of the error matrix processing, overall accuracy of the land cover classification, the user's and producer accuracy and kappa statistic will be calculated (Campbell, 2002; Lillesand et al., 2004; Jensen, 2005). Before applying the accuracy assessment, some initial alignments should be required that include the number of sample points and sample distribution parameters (Random, Stratified Random and Equalized Random).

In this study, the simple random points were selected as distribution parameter pattern to evaluate the accuracy of classified images. The random pattern represents an equal possibility

of sampling points through the whole area of study without any previous considerations. According to Fitzpatrick-Lins (1981), Congalton (1991) and Jensen (2005) the number of random points can be determined:

$$N = \frac{Z^2\,(p)(q)}{E^2}$$

Where p is the expected percent accuracy of the entire map, $q = 100 - p$, E is the acceptable error, and $Z = 2$ from the standard normal deviate of 1.96 for the 95% two side confidence level.

Or: $\quad N = \frac{B\prod_i(1-\prod_i)}{b_i^2}$

Where Πi is the part of a population in the ith class out of k classes, 50%, bi is the preferred precision, B is the upper percentile of the chi square distribution with 1 degree of freedom ($\alpha/k * 100^{th}$)

At the initial process of accuracy, 1000 sampling points were selected, then the number of classes with no data (Class = 0) were discarded and also some random points considered for the water class were reduced, without any data manipulation or consideration of class distribution. About 350 ± 20 ground truth points were randomly tested on the high resolution aerial photography of the Ahipara region as reference image.

3.3.6 LCDB2 Data

Land cover databases version 2 which was derived from Landsat 7 ETM+ imagery acquired in 2001 and 2002, was used to perform the land cover classification for the New Zealand mainland. This classified data were compared with the results of the highest accurate of the RapidEye classified images. LCDB2 data was obtained from the Koordinates (Ltd) website through the URL: http://koordinates.com/#/layer/1072-land-cover-database-version-2-lcdb2/.

ArcGIS 10 tools were used to subset the LCDB2 data to create a subset of the study area.

The subset datasets included 127 polygon features that represented the land cover type, and then they were converted to the raster dataset which the subclasses were grouped into different nine categories of land cover (Figure 4.19).

Chapter 4

Results

4.1 Image Classification and Processing

The results of the image classification were achieved using supervised classification techniques. Maximum Likelihood Classifier (MLC) and a combination of Maximum Likelihood and Parallelepiped (PP) techniques were applied to classify different band combination images of Landsat ETM+ and RapidEye sensors. The accuracy assessment of classified images was estimated by calculating the error matrices, for example, producer's and user's accuracies and Kappa statistics.

4.2 Assessment of the Classification Accuracy

The accuracy assessment of the classified images is an essential part of the classification analysis. For this project, a simple random sampling method was utilized to assess the accuracy of classified images that produced from different classification approaches and band combinations. To assess the accuracy of the classification result for each image, about 340 ± 30 randomly reference points were determined to attain an accuracy of 70% at acceptable error of 5% (Fitzpatrick, 1981 and Jensen, 2005).

High resolution aerial image from Ahipara region was used (Koordinates, n.d.) as reference to verify the Landsat ETM+ and RapidEye classified images. The results of overall classification accuracy for each of different twelve images were achieved (Figure 4.1). The Maximum likelihood and combination of MLC with Parallelepiped (PP) algorithms were used to classify the false colour image (432) of Landsat 7 and a combination of 2 layers of principle components 1 and 2 with the vegetation index layer. Furthermore, the supervised classification using MLC and combination of MLC with PP were employed on images of RapidEye data, including a combination of 5, 4, 3 bands, the principle components 1, 2 with vegetation index layer, the image with 4 bands (the Red-Edge band was removed) the same

bands as L7 false colour image (4, 3 and 2), and RE degraded image from 5m to 30m spatial resolution the same as L7 spatial resolution.

As the Figure 4.1 shows, the overall accuracies for the RapidEye classified images were 84.72% (543_ MLC), 86.73% (543_ PPMLC), 85.29% (PC12VI _ MLC), 85.94% (PC12VI _ PPMLC), 80.41% (4band_ MLC), 81.67% (4band_ PPMLC), 78.85% (DEGRADED _MLC) and 80.28% (DEGRADED_ PPMLC) with an overall kappa statistic of 0.82, 0.85, 0.83, 0.84, 0.78, 0.79, 0.76 and 0.77, respectively. The overall accuracies derived from the Landsat ETM+ classified images (Table 4.1) were 76.79% (432_ MLC), 78.71% (432_ PPMLC), 74.07% (PC12VI_MLC) and 79.78% (PC12VI _ PPMLC), with the overall Kappa statistics of 0.74, 0.75, 0.71 and 0.77, respectively.

The overall accuracy and the overall Kappa statistics results for the Landsat 7 images indicated (Figure 4.1 and Table 4.1) using the combination of the maximum likelihood (MLC) with Parallelepiped (PP) algorithms produced better accuracy to compare with using only MLC, so that the classified image of L7_PC12VI _PPMLC with 79.78% accuracy and 0.77 overall statistic is more accurate that other L7 images (PC12VI_MLC, 432_ MLC and 432_ PPMLC) and the classification of L7_432_ PPMLC image was more accurate than the L7_432_ MLC image. More details on accuracy assessment are summarized in the error matrices and accuracy statistics from Tables 4.2 to 4.25 and Figures 4.2 to 4.7.

As Jensen (2005) suggested, "the probability of a reference pixel being correctly classified and is a measure of omission error that it is called the producer's accuracy", and the user's accuracy represents the probability of the classified image correctly from the map as a reference data (Congalton, 1991). In this study, K_{hat} Coefficient of classified images was measured to define the accuracy between the classified map and the reference data by chance agreement. The quantity of K_{hat} coefficient amount more than 0.8 signifies high accuracy of classified data while the range of 0.4 and 0.8 identify an average accuracy assessment and less than 0.4 represent poor classification execution.
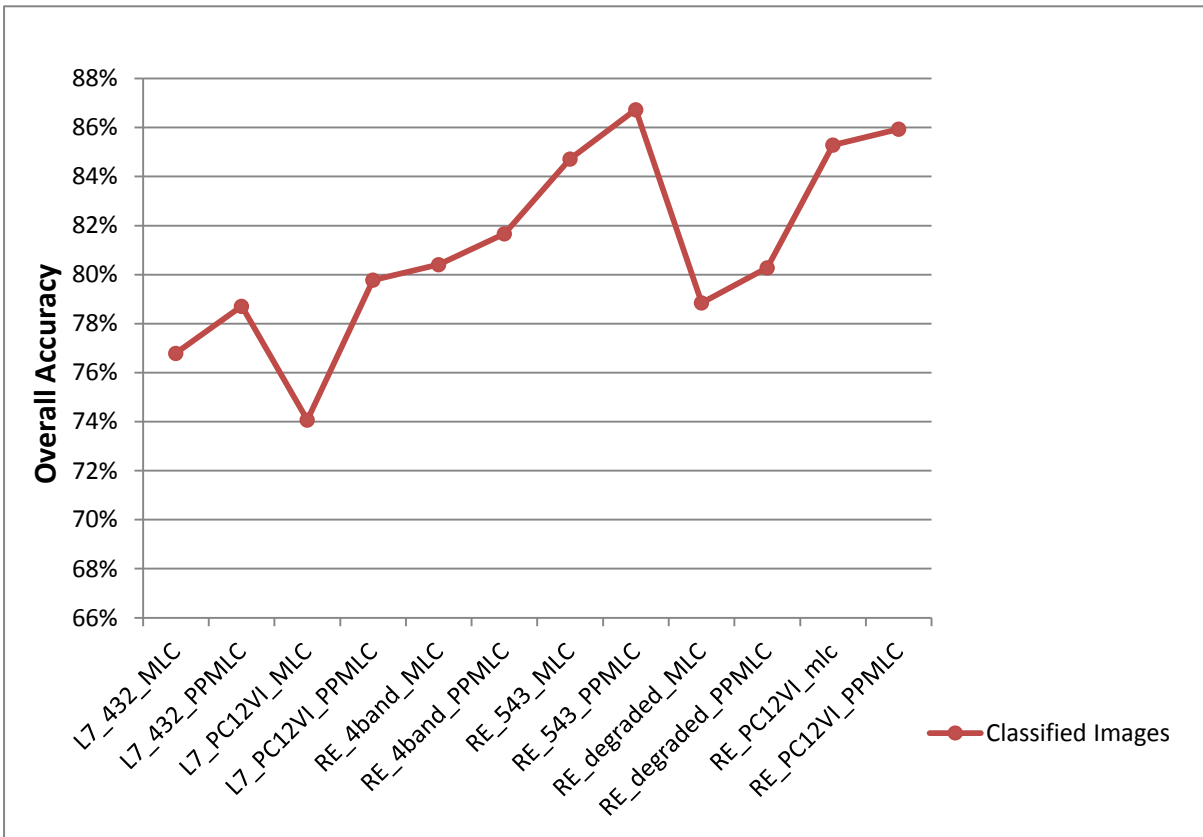
Figure 4.1The results of overall accuracies for the Landsat 7 and RapidEye classified images

Table 4.1 Overall accuracies and Kappa statistics results of Landsat 7 and RapidEye classified images

Classified Images	Overall Accuracy	Overall Kappa Statistic
L7_432_MLC	77%	0.7377
L7_432_PPMLC	79%	0.7585
L7_PC12VI_MLC	74%	0.7062
L7_PC12VI_PPMLC	80%	0.7692
RE_4band_MLC	80%	0.7798
RE_4band_PPMLC	82%	0.7919
RE_543_MLC	85%	0.8249
RE_543_PPMLC	87%	0.8484
RE_DEGRADED_MLC	79%	0.7602
RE_ DEGRADED _PPMLC	80%	0.7755
RE_PC12VI_MLC	85%	0.8323
RE_PC12VI_PPMLC	86%	0.8364

Table 4.2 Error Matrix of Landsat ETM+ (432) image using Maximum Likelihood algorithm

Classified Data	A	B	C	D	E	F	G	H	I	J	K	Row Total
A. Shallow Water	29				5	1					4	39
B. Grassland		43	7				1			8		59
C. Low Producing Grassland		1	19	1	1		1		2	2		27
D. Mangrove			4	15	2		4	4				29
E. Coastal Sand and Gravel	2		1	2	47	1					1	54
F. Wave					1	6						7
G. Pine		1		1			31	5		4		42
H. Manuka/kanuka				5	1		5	59				70
I. Shrubland								1	3			4
J. Indigenous Forest		2	2	1			3		1	22		31
K. Water	3									0	27	30
Column Total	34	47	33	25	57	8	45	69	6	36	32	392

Table 4.3 Accuracy statistics for the classification results of Landsat ETM+ (432) image using Maximum Likelihood algorithm

Class Name	Producer's Accuracy (%)	User's Accuracy (%)	Kappa Statistic
Shallow Water	85%	74%	0.72
Grassland	91%	73%	0.69
Low Producing Grassland	58%	70%	0.68
Mangrove	60%	52%	0.48
Coastal Sand and Gravel	82%	87%	0.85
Wave	75%	86%	0.85
Pine	69%	74%	0.70
Manuka/kanuka	86%	84%	0.81
Shrubland	50%	75%	0.75
Indigenous Fore	61%	71%	0.68
Water	84%	90%	0.89

Overall Classification Accuracy = 76.79%
Overall Kappa Statistics = 0.7377

Table 4.4 Error Matrix of Landsat ETM+ (432) image using combination of Maximum Likelihood with Parallelepiped algorithm

Classified Data	A	B	C	D	E	F	G	H	I	J	K	Row Total
A. Shallow Water	24				2						3	29
B. Grassland		44	4	1						9		59
C. Low Producing Grassland			13	2						3		18
D. Mangrove			1	16			4	2				23
E. Coastal Sand and Gravel	1		1		36	1		1				41
F. Wave					1	13						14
G. Pine				1			24	3	1	1		30
H. Manuka/kanuka	1		1	3			7	62	2	4		80
I. Shrubland		1	1						2			4
J. Indigenous Forest		4	2					4	1	32		43
K. Water	3					1					26	30
Column Total	29	49	23	23	39	15	35	72	6	49	29	371

Table 4.5 Accuracy statistics for the classification results of Landsat ETM+ (432) image using Maximum Likelihood algorithm with Parallelepiped algorithm

Class Name	Producer's Accuracy (%)	User's Accuracy (%)	Kappa Statistic
Shallow Water	83%	83%	0.81
Grassland	90%	75%	0.71
Low Producing Grassland	57%	72%	0.70
Mangrove	70%	70%	0.68
Coastal Sand and Gravel	92%	88%	0.86
Wave	87%	93%	0.93
Pine	69%	80%	0.78
Manuka/kanuka	86%	78%	0.72
Shrubland	33%	50%	0.49
Indigenous Forest	65%	74%	0.71
Water	90%	87%	0.86

Overall Classification Accuracy =   78.71%
Overall Kappa Statistics = 0.7585
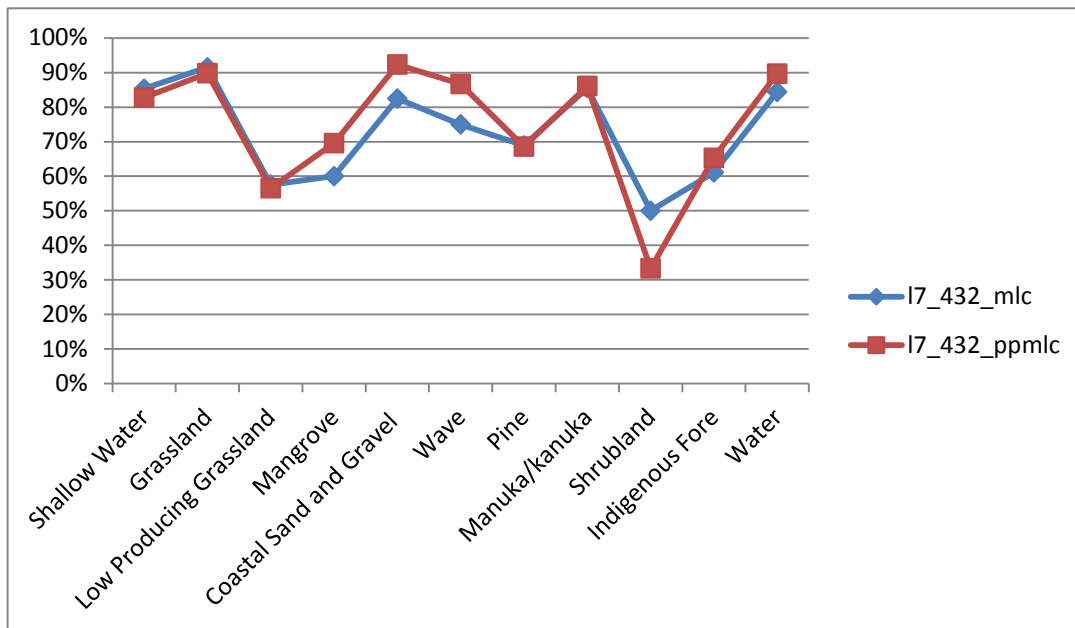
Figure 4.2 Comparing producer's accuracies of Landsat ETM+ classified images (432_mlc/ppmlc)

Table 4.6 Error Matrix of Landsat ETM+ image using combination of PC12 with

Classified Data	A	B	C	D	E	F	G	H	I	J	Raw Total
A. Manuka/Kanuka	47	0	9	1	1	6	0	0	1	0	65
B. Grassland	1	35	0	3	4	5	2	0	0	0	50
C. Mangrove	2	0	4	1	1	0	0	0	0	0	8
D. Pine	2	0	3	21	3	5	0	0	0	0	34
E. Low Producing Grassland	2	7	0	2	43	2	3	0	0	0	59
F. Indigenous Forest	3	2	1	9	2	33	0	0	0	0	50
G. Coastal Sand and Gravel	0	0	0	0	1	0	34	0	2	0	37
H. Wave	0	0	0	0	0	0	2	9	1	0	12
I. Shallow Water	0	0	0	0	0	0	1	2	28	2	33
J. Water	0	0	0	0	0	0	0	1	3	26	30
Column Total	57	44	17	37	55	51	42	12	35	28	378

Table 4.7 Accuracy statistics for the classification results of Landsat ETM+ (432) image using combination of PC12 with Vegetation Index layer and Maximum Likelihood algorithm

Class Name	Producer's Accuracy (%)	User's Accuracy (%)	Kappa Statistic
Shallow Water	80%	85%	83%
Grassland	80%	70%	66%
Low Producing Grassland	78%	73%	68%
Mangrove	24%	50%	48%
Coastal Sand and Gravel	81%	92%	91%
Wave	75%	75%	74%
Pine	57%	62%	58%
Manuka/Kanuka	82%	72%	67%
Indigenous Forest	65%	66%	61%
Water	93%	87%	86%

Overall Classification Accuracy = 74.07%
Overall Kappa Statistics = 0.7062

Table 4.8 Error Matrix of Landsat ETM+ image using combination of PC12 with Vegetation Index layer and Maximum Likelihood with Parallelepiped algorithm

Classified Data	A	B	C	D	E	F	G	H	I	J	Total Raw
A. Manuka/Kanuka	43	1	0	6	0	3	1	0	0	0	54
B. Grassland	2	51	2	0	5	1	4	0	0	0	65
C. Mangrove	0	0	6	2	0	1	0	0	0	0	9
D. Pine	4	0	3	24	1	3	0	0	0	0	35
E. Low Producing Grassland	0	4	0	2	27	1	1	0	0	0	35
F. Indigenous Forest	5	3	2	2	1	49	1	0	0	0	63
G. Coastal Sand and Gravel	0	0	0	0	4	0	32	0	0	0	36
H. Wave	0	0	0	0	0	0	0	8	1	0	9
I. Shallow Water	0	0	0	0	0	0	0	1	27	3	31
J. Water	0	0	0	0	0	0	0	0	3	21	24
Column Total	54	59	13	36	38	58	39	9	31	24	361

Table 4.9Accuracy statistics for the classification results of Landsat ETM+ image using combination of PC12 with Vegetation Index layer and Maximum Likelihood with Parallelepiped algorithm

Class Name	Producer's Accuracy (%)	User's Accuracy (%)	Kappa Statistic
Shallow Water	87%	87%	0.86
Grassland	86%	78%	0.74
Low Producing Grassland	71%	77%	0.74
Mangrove	46%	67%	0.65
Coastal Sand and Gravel	82%	89%	0.88
Wave	89%	89%	0.89
Pine	67%	69%	0.65
Manuka/Kanuka	80%	80%	0.76
Indigenous Forest	84%	78%	0.74
Water	88%	88%	0.87

Overall Classification Accuracy = 79.78%
Overall Kappa Statistics = 0.7692
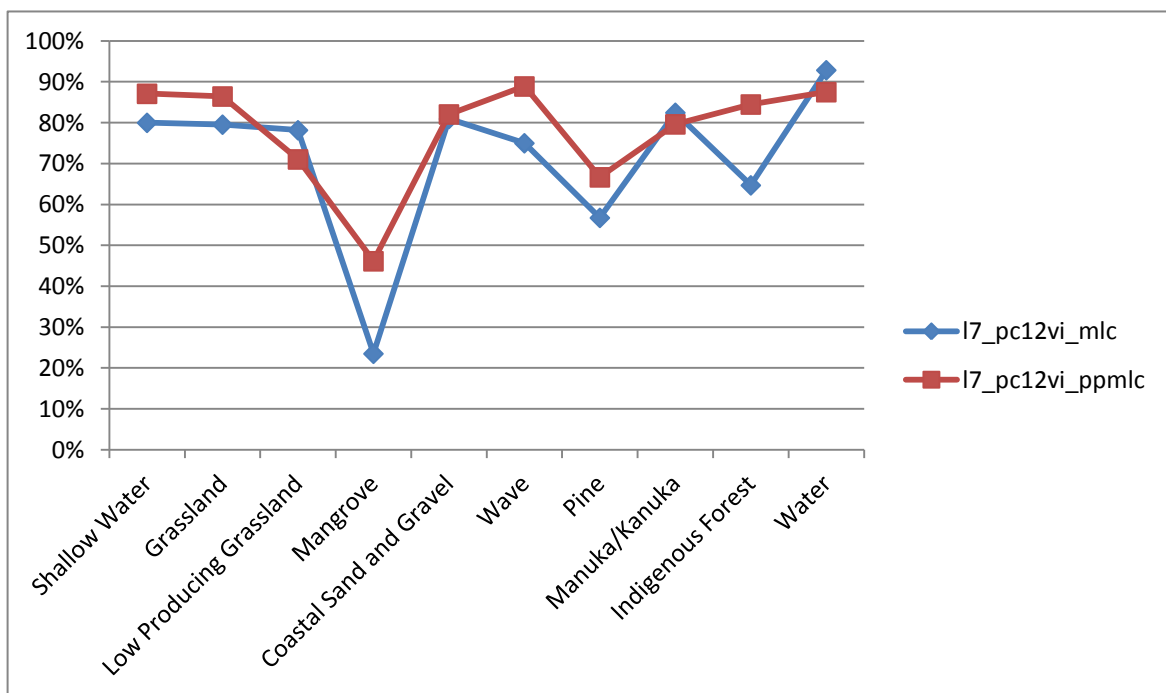
Figure 4.3 Comparing producer's accuracies of Landsat ETM+ classified images (pc12vi_mlc/ppmlc)

Table 4.10 Error Matrix of RapidEye (543) image using Maximum Likelihood algorithm

Classified Data	A	B	C	D	E	F	G	H	I	J	K	Raw Total
A. Coastal Sand and Gravel	24	2	0	0	0	0	0	0	0	0	0	26
B. Low Producing Grassland	0	26	2	0	0	0	0	0	0	4	0	32
C. Shrubland	0	0	10	1	0	2	0	0	0	0	0	13
D. Indigenous Forest	0	0	3	62	0	0	3	2	0	0	0	70
E. Wave	0	0	0	0	4	0	0	0	0	0	0	4
F. Mangrove	1	0	3	0	0	7	0	0	0	0	0	11
G. Manuka/Kanuka	0	1	1	3	0	0	35	2	0	0	0	42
H. Pine	0	0	0	0	0	0	1	10	0	0	0	11
I. Water	0	0	0	0	1	0	0	0	26	0	2	29
J. Grassland	2	1	0	3	0	0	0	0	0	34	0	40
K. Shallow water	0	0	0	0	1	0	0	0	3	0	17	21
Column Total	27	30	19	69	6	9	39	14	29	38	19	299

Table 4.11 Accuracy statistics for the classification results of RapidEye (543) image using Maximum Likelihood algorithm

Class Name	Producer's Accuracy (%)	User's Accuracy (%)	Kappa Statistic
Water	90%	87%	0.85
Mangrove	78%	64%	0.63
Shallow water	89%	81%	0.80
Low Producing Grassland	87%	81%	0.79
Indigenous Forest	90%	87%	0.84
Coastal Sand and Gravel	89%	92%	0.92
Manuka/Kanuka	90%	83%	0.81
Pine	71%	91%	0.90
Shrubland	53%	77%	0.75
Grassland	89%	85%	0.83
Wave	67%	100%	1.00

Overall Classification Accuracy = 84.72%
Overall Kappa Statistics = 0.8249

Table 4.12 Error Matrix of RapidEye (543) image using combination of Maximum Likelihood with Parallelepiped algorithm

Classified Data	A	B	C	D	E	F	G	H	I	J	K	Row Total
A. Coastal Sand and Gravel	18	2	0	0	1	1	0	0	0	1	0	23
B. Low Producing Grassland	1	42	4	0	0	0	0	0	0	1	0	48
C. Shrub	0	0	20	1	0	1	1	0	0	1	0	24
D. Indigenous Forest	0	0	2	56	0	1	4	1	0	0	0	64
E. Wave	0	0	0	0	8	0	0	0	1	0	0	9
F. Mangrove	0	0	1	0	0	7	2	0	0	0	0	10
G. Manuka/Kanuka	0	0	1	1	0	1	43	0	0	0	0	46
H. Pine	0	0	0	1	0	0	0	12	0	0	0	13
I. Water	0	0	0	0	2	0	0	0	22	0	1	25
J. Grassland	1	2	0	0	0	0	0	0	0	34	0	37
K. Shallow Water	0	0	0	0	0	0	0	0	3	0	6	9
Column Total	20	46	28	59	11	11	50	13	26	37	7	308

Table 4.13 Accuracy statistics for the classification results of RapidEye (543) image using Maximum Likelihood algorithm with Parallelepiped algorithm

Class Name	Producer's Accuracy (%)	User's Accuracy (%)	Kappa Statistic
Water	85%	88%	0.87
Mangrove	64%	70%	0.69
Shallow Water	86%	67%	0.66
Low Producing Grassland	91%	88%	0.85
Indigenous Forest	95%	88%	0.85
Coastal Sand and Gravel	90%	78%	0.77
Manuka/Kanuka	86%	93%	0.92
Pine	92%	86%	0.85
Shrubland	71%	83%	0.82
Grassland	92%	92%	0.91
Wave	73%	89%	0.88

Overall Classification Accuracy = 86.73%
Overall Kappa Statistics = 0.8484
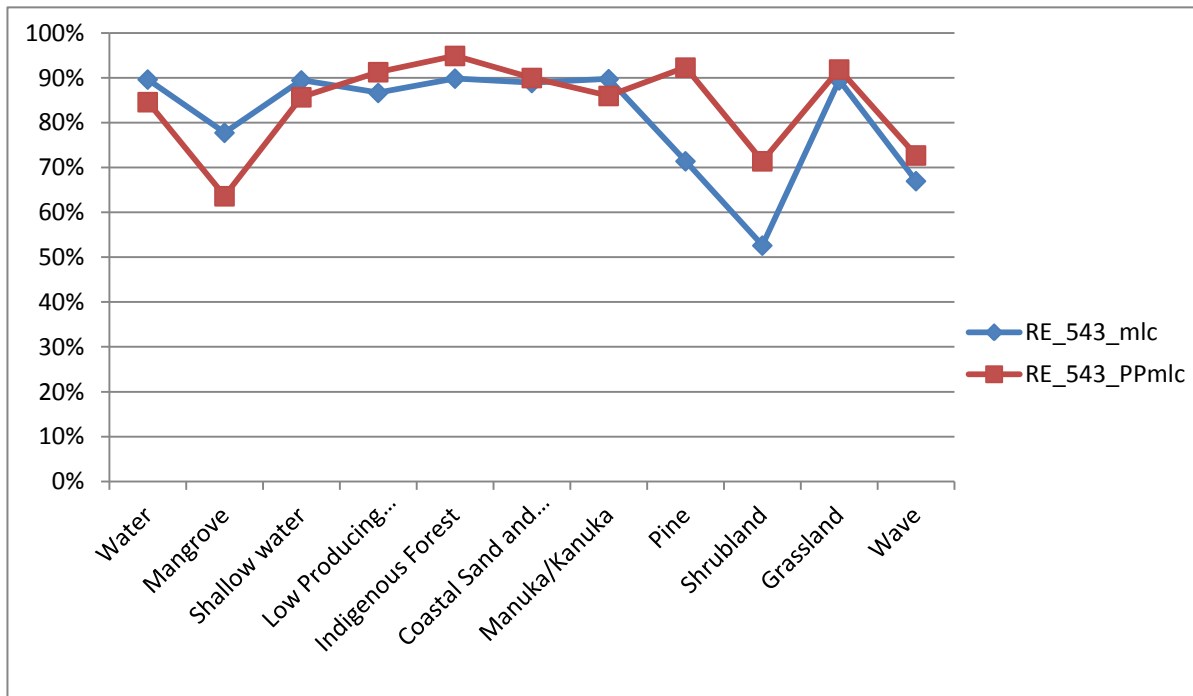
Figure 4.4 Comparing producer's accuracies of RapidEye classified images (543_mlc/ppmlc)

Table 4.14 Error Matrix of RapidEye image using combination of PC12 with Vegetation Index layer and

Classified Data	A	B	C	D	E	F	G	H	I	J	K	Raw Total
A. Shallow water	15	0	0	0	0	0	0	0	2	0	0	17
B. Water	2	26	0	0	0	0	0	0	1	0	0	29
C. Low Producing Grassland	0	0	53	1	0	0	7	0	0	0	1	62
D. Coastal Sand and Gravel	0	0	2	22	0	0	0	0	0	0	0	24
E. Indigenous Forest	0	0	0	0	54	0	0	3	0	1	3	61
F. Mangrove	0	0	0	0	0	9	0	0	0	0	3	12
G. Grassland	0	0	3	0	0	0	31	0	0	1	0	35
H. Manuka/Kanuka	0	0	0	0	4	3	0	48	0	6	0	61
I. Wave	2	0	0	0	0	0	0	0	7	0	0	9
J. Pine	0	0	0	0	1	0	0	0	0	7	0	8
K. Shrubland	0	0	0	0	1	2	0	0	0	0	16	19
Column Total	19	26	58	23	60	14	38	51	10	15	23	339

Table 4.15Accuracy statistics for the classification results of RapidEye image using combination of PC12 with Vegetation Index layer and Maximum Likelihood algorithm

Class Name	Producer's Accuracy (%)	User's Accuracy (%)	Kappa Statistic
Coastal Sand and Gravel	96%	92%	0.91
Pine	47%	88%	0.87
Grassland	82%	89%	0.87
Shallow water	79%	88%	0.88
Water	100%	90%	0.89
Wave	70%	78%	0.77
Low Producing Gravel	91%	85%	0.83
Shrubland	70%	84%	0.83
Manuka/Kanuka	94%	79%	0.75
Indigenous Forest	90%	87%	0.84
Mangrove	64%	75%	0.74

Overall Classification Accuracy = 85.29%
Overall Kappa Statistics = 0.8323

Table 4.16 Error Matrix of RapidEye image using combination of PC12 with Vegetation Index layer and Maximum Likelihood with Parallelepiped algorithm

Classified Data	A	B	C	D	E	F	G	H	I	J	K	Raw Total
A. Shallow water	12	4	0	0	0	0	0	0	0	0	0	16
B. Water	2	23	0	0	0	0	0	0	0	0	0	25
C. Low Producing Grassland	0	0	60	0	0	0	5	0	0	1	0	66
D. Coastal Sand and Gravel	0	1	0	15	0	0	0	0	0	0	0	16
E. Indigenous Forest	0	0	0	0	51	0	1	4	0	1	5	62
F. Mangrove	0	0	0	0	0	3	0	0	0	0	1	4
G. Grassland	0	0	5	2	1	0	28	0	0	0	0	36
H. Manuka/Kanuka	0	0	0	0	2	1	0	51	0	2	0	56
I. Wave	0	0	0	1	0	0	0	0	8	0	0	9
J. Pine	0	0	0	0	0	0	0	0	0	9	0	9
K. Shrubland	0	0	1	0	0	0	0	1	0	0	9	11
Column Total	14	28	66	19	54	4	34	56	8	13	15	311

Table 4.17 Accuracy statistics for the classification results of RapidEye image using combination of PC12 with Vegetation Index layer and Maximum Likelihood algorithm with Parallelepiped algorithm

Class Name	Producer's Accuracy (%)	User's Accuracy (%)	Kappa Statistic
Coastal Sand and Gravel	79%	94%	0.93
Pine	69%	100%	1.00
Grassland	82%	78%	0.75
Shallow water	86%	75%	0.74
Water	82%	92%	0.91
Wave	100%	89%	0.89
Low Producing Grassland	91%	90%	0.87
Shrubland	60%	82%	0.81
Manuka/Kanuka	91%	89%	0.87
Indigenous Forest	94%	82%	0.79
Mangrove	75%	75%	0.75

Overall Classification Accuracy = 85.94%
Overall Kappa Statistics = 0.8364
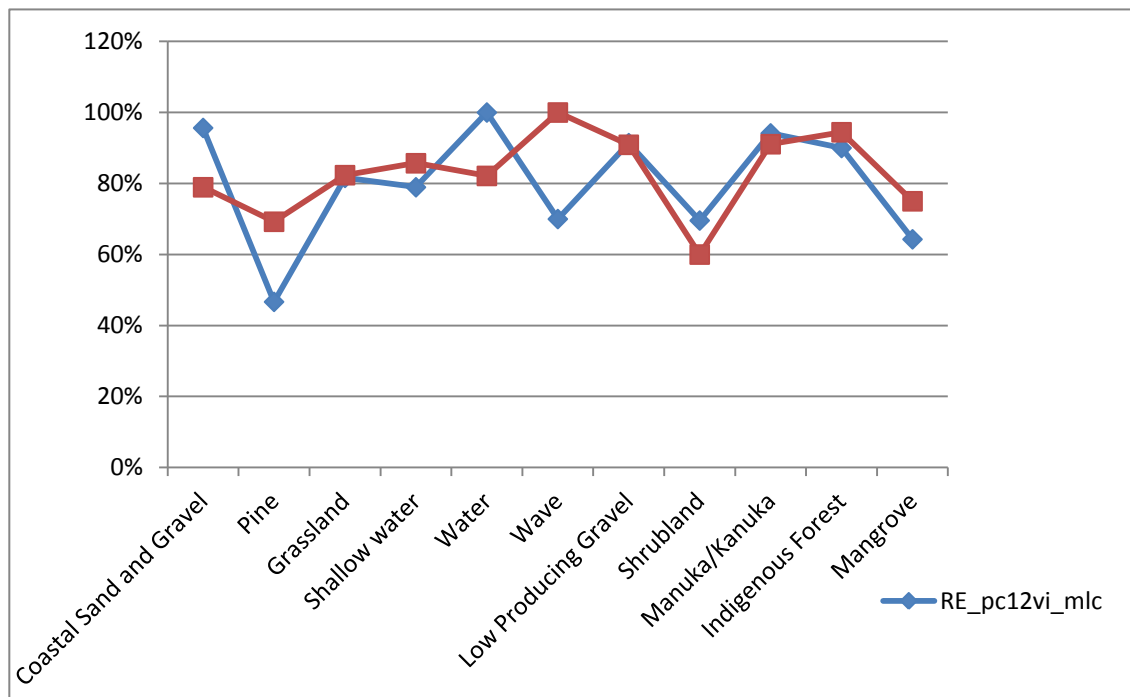
Figure 4.5 Comparing producer's accuracies of RapidEye classified images (pc12vi_mlc/ppmlc)

Table 4.18 Error Matrix of RapidEye (543) degraded image using Maximum Likelihood algorithm

Classified Data	A	B	C	D	E	F	G	H	I	J	K	Raw Total
A. Coastal Sand and Gravel	20			1		1						22
B. Pine		11						1		2		14
C. Grassland		1	48				15					64
D. Shallow water	1			56	4	5					1	67
E. Water				3	27							30
F. Wave				1	1	2					1	5
G. Low Producing Grassland	1		9				32		1	1		44
H. Shrubland							2	19		3	3	27
I. Manuka/Kanuka	1							3	32	2	1	39
J. Indigenous Forest		2					2	1	3	47	3	58
K. Mangrove	1			1				1	1		8	12
Column Total	24	14	57	61	33	8	51	25	37	55	17	382

Table 4.19 Accuracy statistics for the classification results of RapidEye degraded image using Maximum Likelihood algorithm

Class Name	Producer's Accuracy (%)	User's Accuracy (%)	Kappa Statistic
Coastal Sand and Gravel	83%	91%	0.90
Pine	79%	79%	0.78
Grassland	84%	75%	0.71
Shallow water	92%	84%	0.80
Water	82%	90%	0.89
Wave	25%	40%	0.39
Low Producing Grassland	63%	73%	0.69
Shrubland	76%	70%	0.68
Manuka/Kanuka	86%	82%	0.80
Indigenous Forest	85%	80%	0.76
Mangrove	47%	67%	0.65

Overall Classification Accuracy = 78.85%
Overall Kappa Statistics = 0.7602

Table 4.20 Error Matrix of RapidEye (543) degraded image using combination of Maximum Likelihood with Parallelepiped algorithm

Classified Data	A	B	C	D	E	F	G	H	I	J	K	Raw Total
A. Coastal Sand and Gravel	18	0	0	0	0	1	0	0	0	1	0	20
B. Pine	0	19	0	0	1	0	0	0	1	2	1	24
C. Grassland	0	0	44	2	0	0	4	3	1	1	2	57
D. Shallow water	0	0	1	47	3	4	0	0	0	0	0	55
E. Water	0	0	0	1	22	1	0	0	0	0	0	24
F. Wave	0	0	0	1	2	3	0	0	0	0	0	6
G. Low Producing Grassland	1	0	5	1	0	0	24	0	1	0	1	33
H. Shrubland	1	0	1	0	0	0	1	13	0	1	1	18
I. Manuka/Kanuka	0	1	0	0	0	0	1	1	36	5	0	44
J. Indigenous Forest	0	3	1	0	0	0	2	1	6	57	1	71
K. Mangrove	0	0	0	0	0	0	0	2	0	0	6	8
Column Total	20	23	52	52	28	9	32	20	45	67	12	360

Table 4.21 Accuracy statistics for the classification results of RapidEye degraded image using Maximum Likelihood algorithm with Parallelepiped algorithm

Class Name	Producer's Accuracy (%)	User's Accuracy (%)	Kappa Statistic
Coastal Sand and Gravel	90%	90%	0.89
Pine	83%	79%	0.78
Grassland	85%	77%	0.73
Shallow water	90%	85%	0.83
Water	79%	92%	0.91
Wave	33%	50%	0.49
Low Producing Grassland	75%	73%	0.70
Shrubland	65%	72%	0.71
Manuka/Kanuka	80%	82%	0.79
Indigenous Forest	85%	80%	0.76
Mangrove	50%	75%	0.74

Overall Classification Accuracy = 80.28%
Overall Kappa Statistics = 0.7755
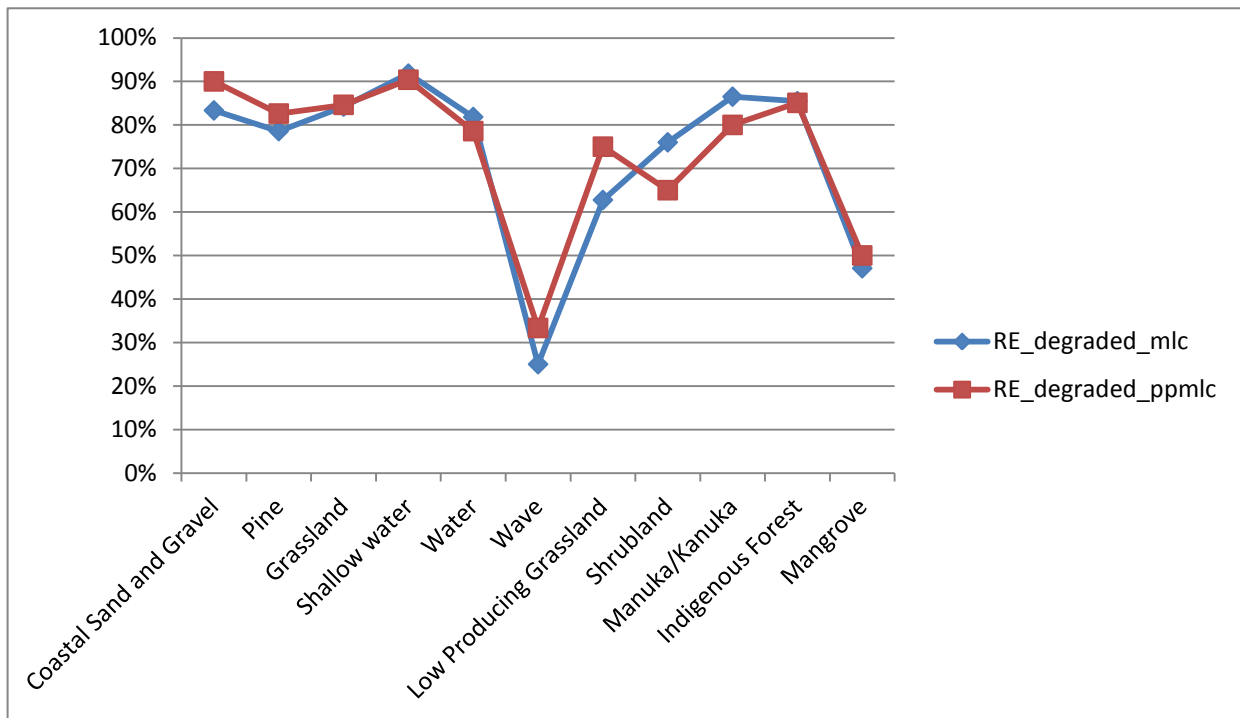
Figure 4.6 Comparing producer's accuracies of RapidEye classified images (degraded_mlc/ppmlc)

Table 4.22 Error Matrix of RapidEye (432) 4 bands image using Maximum Likelihood algorithm

Classified Data	A	B	C	D	E	F	G	H	I	J	K	Raw Total
A. Water	20		1									21
B. Mangrove		7			1	1						9
C. Shallow water	3		24							1	1	29
D. Low Producing Grassland				34	2			2	1			39
E. Indigenous Forest				2	40	2	2	1				47
F. Manuka/Kanuka						23	3	2				28
G. Pine					1	18	10					29
H. Shrubland		1		3	1	1		23	1			30
I. Grassland				2	1			1	34			38
J. Wave										2		2
K. Coastal Sand and Gravel				1						1	17	19
Column Total	23	8	25	42	46	45	15	29	36	4	18	291

Table 4.23 Accuracy statistics for the classification results of RapidEye (432) 4 bands image using Maximum Likelihood algorithm

Class Name	Producer's Accuracy (%)	User's Accuracy (%)	Kappa Statistic
Water	87%	95%	0.95
Mangrove	88%	78%	0.77
Shallow water	96%	83%	0.81
Low Producing Grassland	81%	87%	0.85
Indigenous Forest	87%	85%	0.82
Coastal Sand and Gravel	94%	89%	0.89
Manuka/Kanuka	51%	82%	0.79
Pine	67%	34%	0.31
Shrubland	79%	77%	0.74
Grassland	94%	89%	0.88
Wave	50%	100%	1.00

Overall Classification Accuracy = 80.41%
Overall Kappa Statistics = 0.7798

Table 4.24 Error Matrix of RapidEye (432) 4 bands image using combination of Maximum

Classified Data	A	B	C	D	E	F	G	H	I	J	K	Raw total
A. Water	19		3									22
B. Mangrove		4										4
C. Shallow water	1		15									16
D. Low Producing Grassland				37		2	1			2		42
E. Indigenous Forest				4	47	1	2	2	1			57
F. Coastal Sand and Gravel				2		21						23
G. Manuka/Kanuka					2		28	12	2	1		45
H. Pine				1	1		5	21	1			29
I. Shrubland		1			1			2	17	1		22
J. Grassland				2	1					33		36
K. Wave		1									3	4
Column Total	20	6	18	46	52	24	36	37	21	37	3	300

Table 4.25 Accuracy statistics for the classification results of RapidEye (432) 4 bands image using Maximum Likelihood algorithm with Parallelepiped algorithm

Class Name	Producer's Accuracy (%)	User's Accuracy (%)	Kappa Statistic
Water	95%	86%	0.85
Mangrove	67%	100%	1.00
Shallow water	83%	94%	0.93
Low Producing Grassland	80%	88%	0.86
Indigenous Forest	90%	82%	0.79
Coastal Sand and Gravel	88%	91%	0.91
Manuka/Kanuka	78%	62%	0.57
Pine	57%	72%	0.69
Shrubland	81%	77%	0.76
Grassland	89%	92%	0.90
Wave	100%	75%	0.75

Overall Classification Accuracy = 81.67%
Overall Kappa Statistics = 0.7919
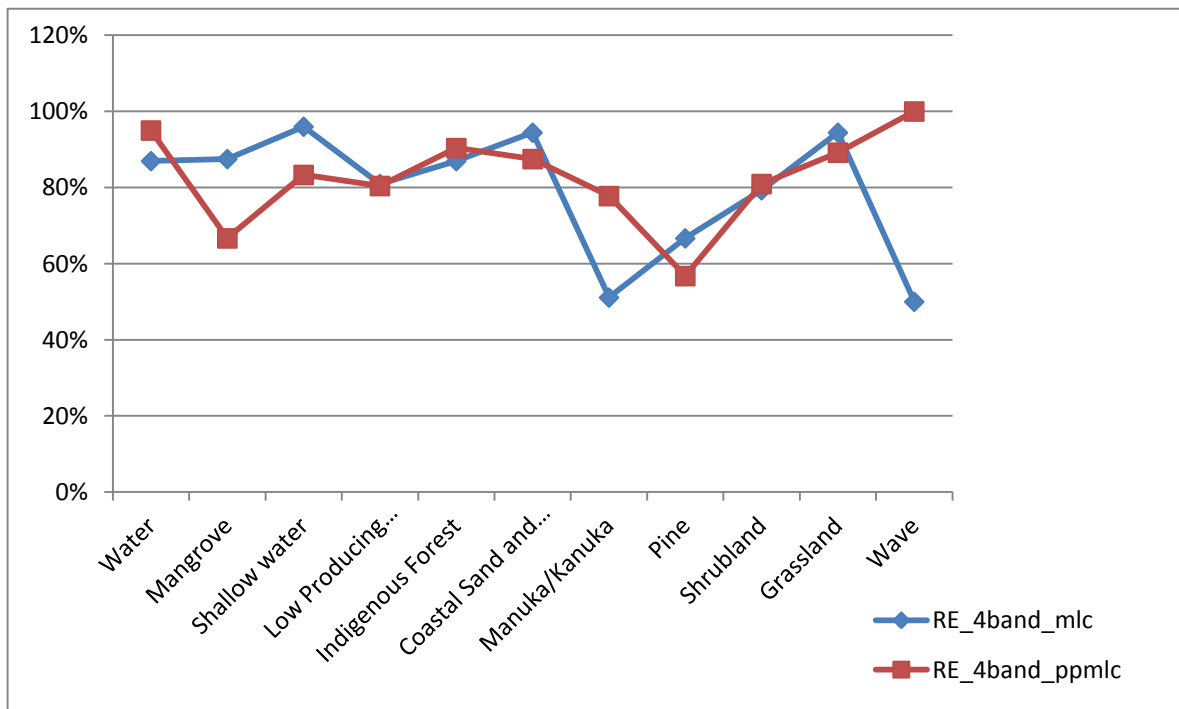
Figure 4.7 Comparing producer's accuracies of RapidEye classified images (4band_mlc/ppmlc)
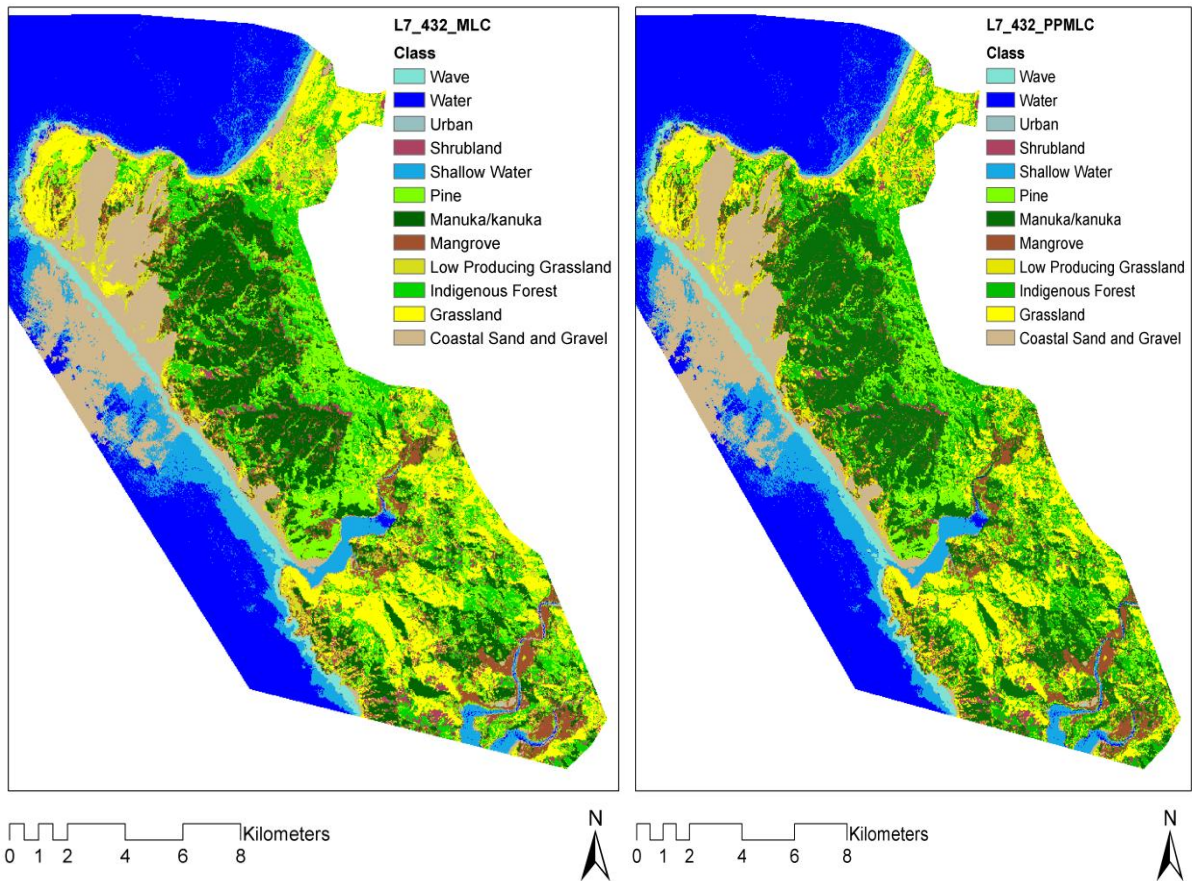
Figure 4.8 Landsat classified images (432_MLC/PPMLC)

For classified image of Landsat7 with band combination of 432, the maximum likelihood classifier provided a moderate overall classification accuracy of 76.79% (Table 4). The overall Kappa statistic of 0.73 is also shows a moderate classification performance. High producer's accuracies were identified in the grassland (91%), manuka/ kanuka forest (86%), shallow water (85%) and water (84%), categories. For the remaining classes, moderate producer's accuracy was occurred between 50% and 70%. High user's accuracies were distinguished in the water (90%), coastal sand and gravel (87%), wave (86%) and manuka/ kanuka (84%) categories, and for the other classes, moderate user's accuracies were observed ranging between 52% and 75% (Table 4.3). The classes of water, manuka/kanuka and coastal sand and gravel had high accuracy, because of the constantly high accuracy in both producers' and users' points.

The Kappa statistics identified good classification execution in water, coastal sand and wave classes; while for the rest of the classes, moderate classification accuracies were achieved. Forest contained several errors from grassland, low producing grassland, pine and shrub land.

Mangrove class showed errors from low producing grassland, coastal sand, pine and manuka/kanuka.

The combination of maximum likelihood with parallelepiped algorithm on the Landsat ETM+ identified moderate overall accuracy of 78.71% with Kappa statistic of 0.75. The results show slightly better accuracy than the classified data created by MLC procedure (Tables 4.1 and 4.5, Figure 4.1). In this classification performance more classes with high producer's and user's accuracy were observed in water (90%, 87%), coastal sand and gravel (92%, 88%), wave (87%, 93%), respectively. In addition, the grassland and pine classes assigned high accuracy of 90% for producer and 80% for user. Low producers accuracy of 33% was indicated in the shrub-land class.

The high value of Kappa were estimated for wave (0.93), coastal sand and gravel (0.86), water (0.86) and shallow water (0.81%) (Table 4.5).The accuracy assessment results indicate that using a combination of MLC with parallelepiped algorithm show improved image classification accuracy (Table 4.1 and Figure 4.2).
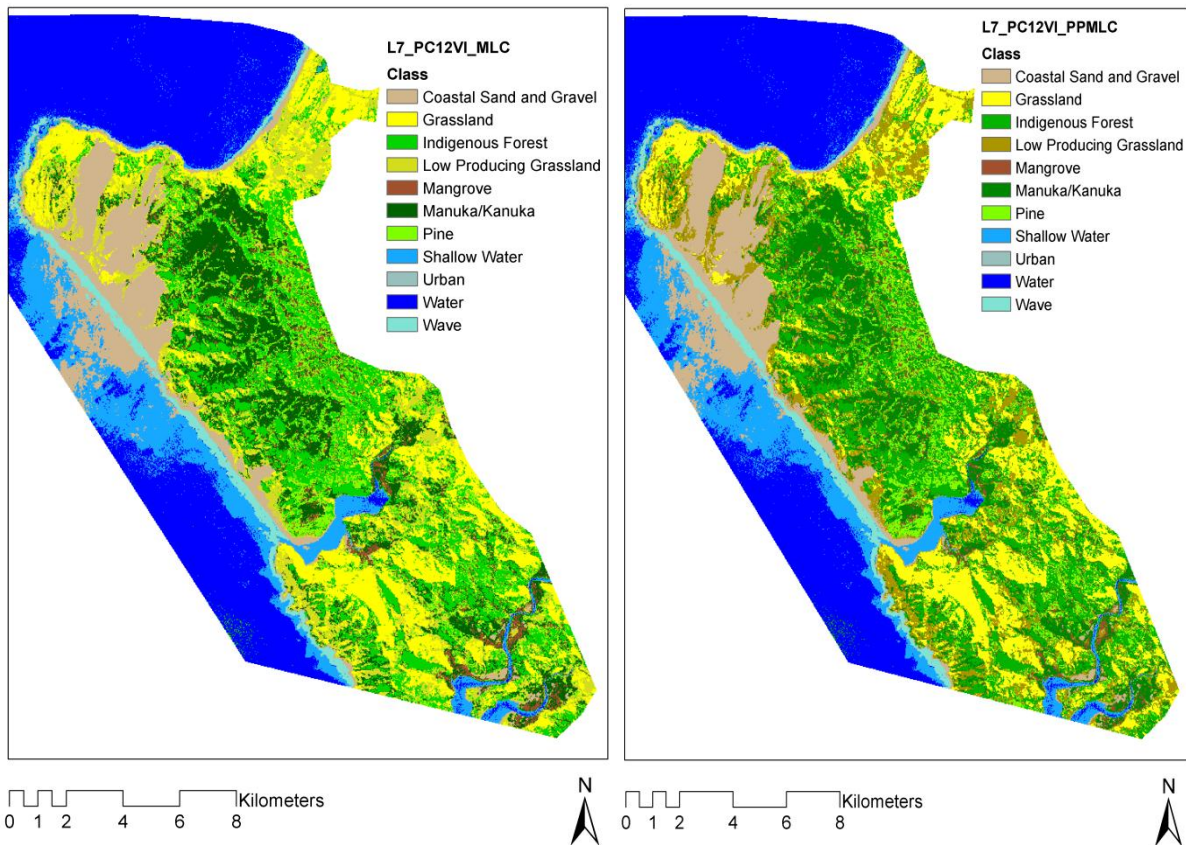
Figure 4.9 Landsat classified images (PC12VI_MLC/PPMLC)

A combination of principle components 1 and 2 with vegetation index and MLC algorithm showed lower accuracy than L7_MLC and L7_PPMLC classified images (Figure 4.1 and table 4.1); whereas L7_PC12VI combined with PPMLC achieved the highest classification accuracy for several approaches that classify L7 images (Figure 4.3). The overall classification accuracies for L7_PC12VI_ MLC was 74.07% with a Kappa statistic of 0.70 (table 4.7) and 79.78% overall accuracy was for L7_PC12VI_PPMLC with a Kappa statistic of 0.77 (table 4.9).

The combination of PC12VI with PPMLC method provided the best classification performance (Table 4.9) for all L7 data. For both accuracies; producer's and use's high percentages were observed in wave, water, shallow water, costal sand and manuka/kanuka classes (Table 4.7). The mangrove category had the lowest producers of 24% accuracy for PC12VI with MLC method and 46% for PPMLC combination. The remaining categories had moderate classification accuracies for both images (Figure 4.3).
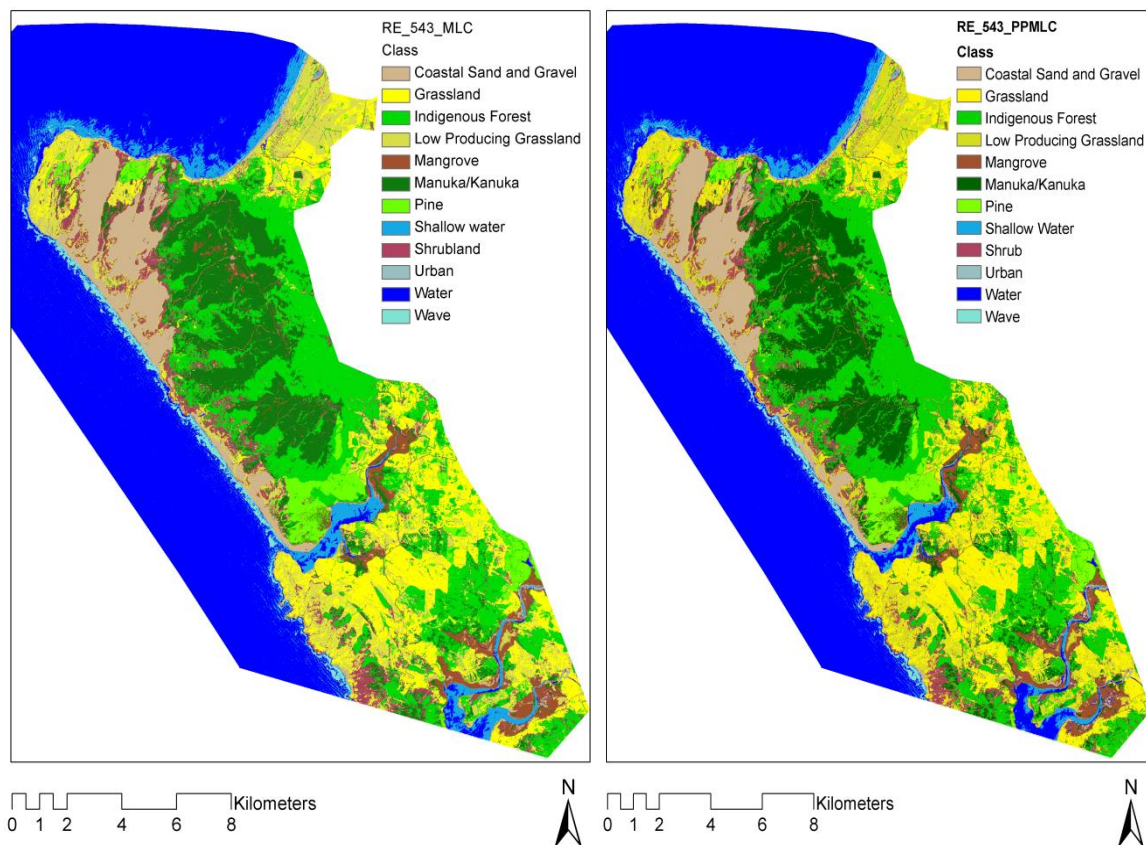
Figure 4.10 RapidEye Classified images (543_MLC/PPMLC)

Applying the maximum likelihood classification algorithm on 543 band combination of RE image generated a high overall accuracy of 84.72% with a Kappa statistic of 0.82 (Table 4.11). The high producer's accuracies were estimated for manuka/ kanuka (90%) indigenous forest (90%), water (90%) shallow water (89%), coastal sand and gravel (89%), grassland (89%) and low producing grassland (87%), while other categories showed moderate accuracies. For user's accuracy, wave class had the highest accuracy of 100%, whereas mangrove (64%) and shrub-land (77%) classes had moderate accuracies. All remaining classes had high level of use's accuracies (Table 4.11). The Kappa statistic of 1.00 in wave represented that the classification of this class was the most accurate. Mangrove and shrub-land had moderate Kappa value of 0.64 and 0.75, respectively. For the other remaining classes the high kappa values were observed.

The combination of MLC with PP for RE (543) image generated highest overall classification accuracy of 86.73% and Kappa statistic of 0.85 among all the classified images (Table 4.13 and 4.1, Figure 4.4). High producer's accuracies were recorded for the most of classes, including indigenous forest (95%), grassland (92%), pine (92%), low producing grassland (91%), coastal sand and gravel (90%), manuka/kanuka (86%), shallow water (86%) and water (85%). The mangrove, shrub-land and wave classes had moderate producer's accuracies. On the other hand, high user's accuracies were observed for manuka/kanuka, grassland, wave, water, low producing grassland, indigenous forest, pine and shrub-land while shallow water (67%), mangrove (70%) and coastal sand and gravel (78%) showed moderate user's accuracies. Shallow water mangrove and coastal sand and gravel had moderate Kappa statistics of 0.60, 0.69 and 0.77 respectively that showed moderate classification results. For the remaining classes, Kappa statistics indicate good classification performance (Table 4.13).
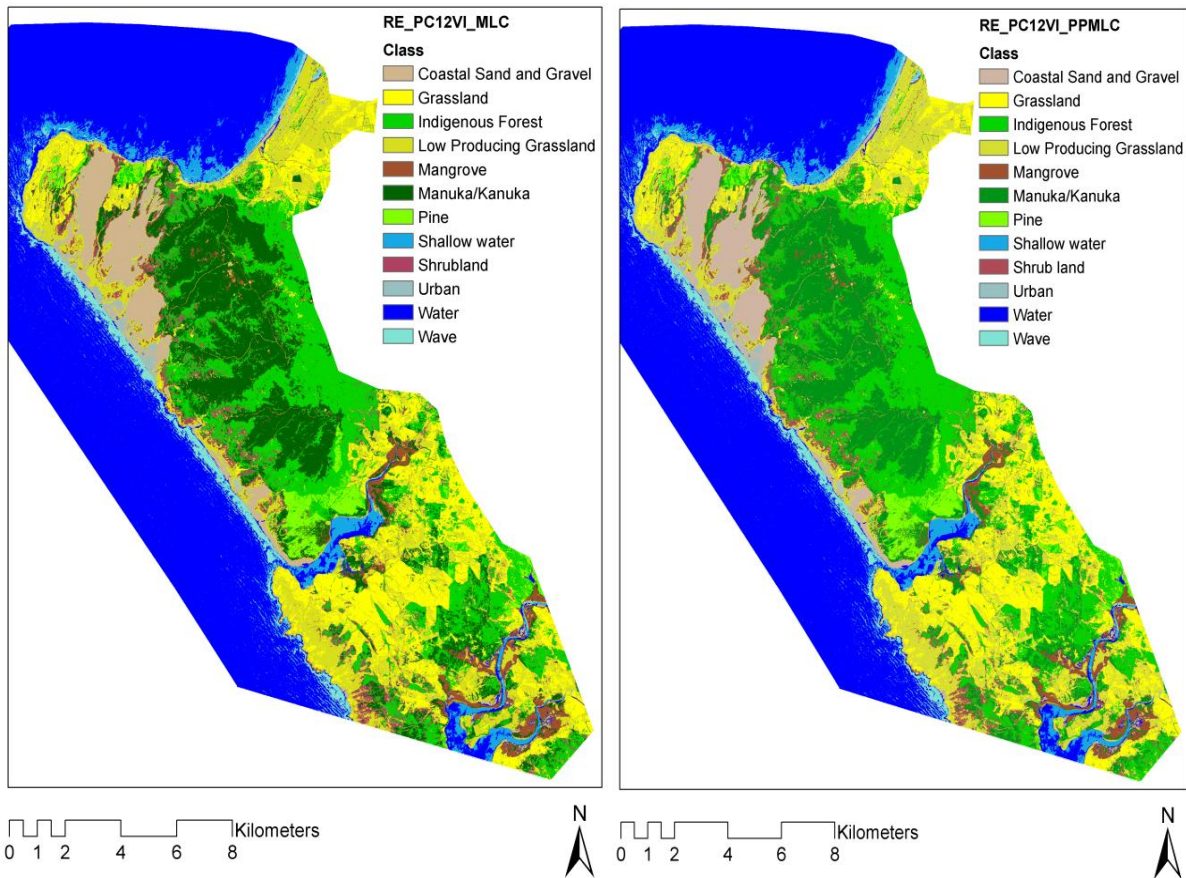
Figure 4.11 RapidEye Classified images (PC12VI_MLC/PPMLC)

The second and third high accuracy assessment performances were observed for the RapidEye classified image using a combination of principle components 1 and 2 (PC12) with vegetation index (VI) layer for maximum likelihood (MLC) and parallelepiped (PP) classification algorithm and MLC (Table 4.1, Figure 4.1).The classification performed on RapidEye's PC12VI image using MLC and PPMLC algorithms generated overall accuracies of 85.29% with a Kappa value of 0.83, and 85.94% with a Kappa value of 0.84, respectively that determined a good classification execution (Table 4.15 and 4.17, Figure 4.5). For both RE classified images using PC12VI _MLC and PPMLC methods high producer's accuracies were distinguished in same categories; including indigenous forest (90%, 94%), manuka/ kanuka (94%, 91%), low producing grassland (91%, 91%), water (100%, 82%), grassland (82%, 82%), coastal sand and gravel (96%, 79%) and shallow water (79%, 86%) classes (Table 4.15 and 4.17). The moderate producer's accuracies were observed in mangrove (64%, 75%), shrub-land (70% , 60%) and pine (47%, 69%), respectively. similarly, high user's accuracies were observed for both the RE classified images (PC12VI _MLC & PC12VI_ PPMLC) in coastal sand and gravel (92%, 94%), water (90%, 92%), low producing grassland

(85% , 90%), shrub-land (84%, 82%), indigenous forest (87%, 82%), manuka/kanuka (79%, 89%) and pine (88%, 100%) classes respectively.

Moreover, high individual accuracies were observed in the grassland (89%), shallow water (88%) classes for PC12VI _MLC image and in the wave (89%) class for PC12VI _PPMLC image. Kappa statistics for both classified images (MLC, PPMLC) were indicated as good classification performances for some same classes, such as costal sand and gravel (91%, 93%), pine (87%, 1%), water (89%, 91%) and low producing grassland (83%, 87%) (Table 4.15 and 4.17).
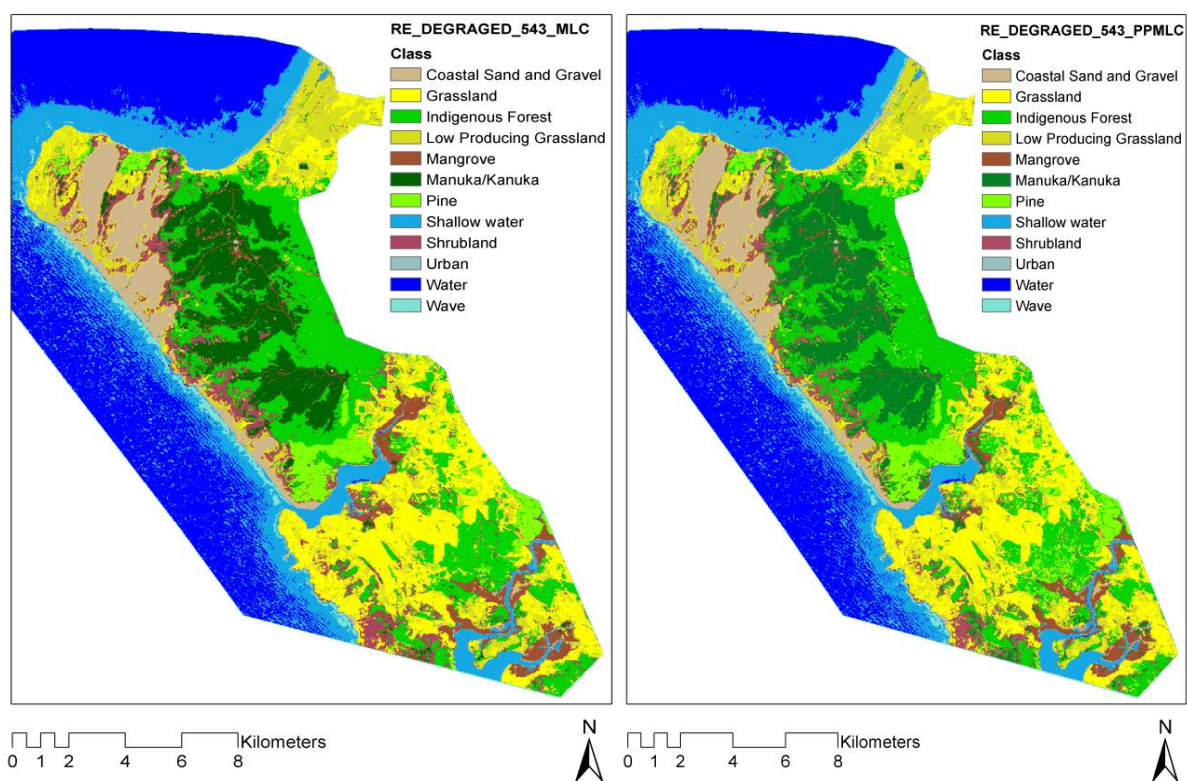
Figure 4.12 RapidEye Classified images (DEGRADED_543_MLC/PPMLC)

The RE_degraded (30 m) image with band combination of 543 was classified using MLC and PPMLC classifiers. For the RE_degraded classified image using PPMLC combination, the accuracy assessment was higher than the RE_degraded classified image using MLC (Figure 4.1). The combination of maximum likelihood with parallelepiped algorithms produced a high overall accuracy of 80.28% with Kappa statistic of 0.78 (Table 4.21) that showed a good classification performance. The RE_degraded classified image using MLC generated moderate overall accuracy of 78.85% with Kappa value of 0.76 (Table 4.19).

80

For both classified images high or moderate producer's accuracies were observed among the same categories. For RE_degraded classified images (MLC/ PPMLC), high producer's accuracies were estimated (MLC, PPMLC) in the shallow water (92%, 90%), coastal sand and gravel (83%, 90%), indigenous forest (85%, 85%), grassland (84%, 85%) , manuka/kanuka (86%, 80%), pine (79%, 83%) and water (82%, 79%) categories (Figure 4.6) respectively. Whereas, moderate accuracies were observed for same classes for both RE _degraded classified images, which included low producing grassland (63%, 75%), shrub-land (76%, 65%) and mangrove (47%, 50%). However, the wave class for both images had a low producer's accuracy of 25% and 33%, respectively. The tables 4.19 and 4.21revealed high and moderate user's accuracies for both classified images in the same classes. The Kappa values showed good classification implementation in the coastal sand and gravel, shallow water, water, manuka/ kanuka categories for both RE-degraded images (MLC/PPMLC).
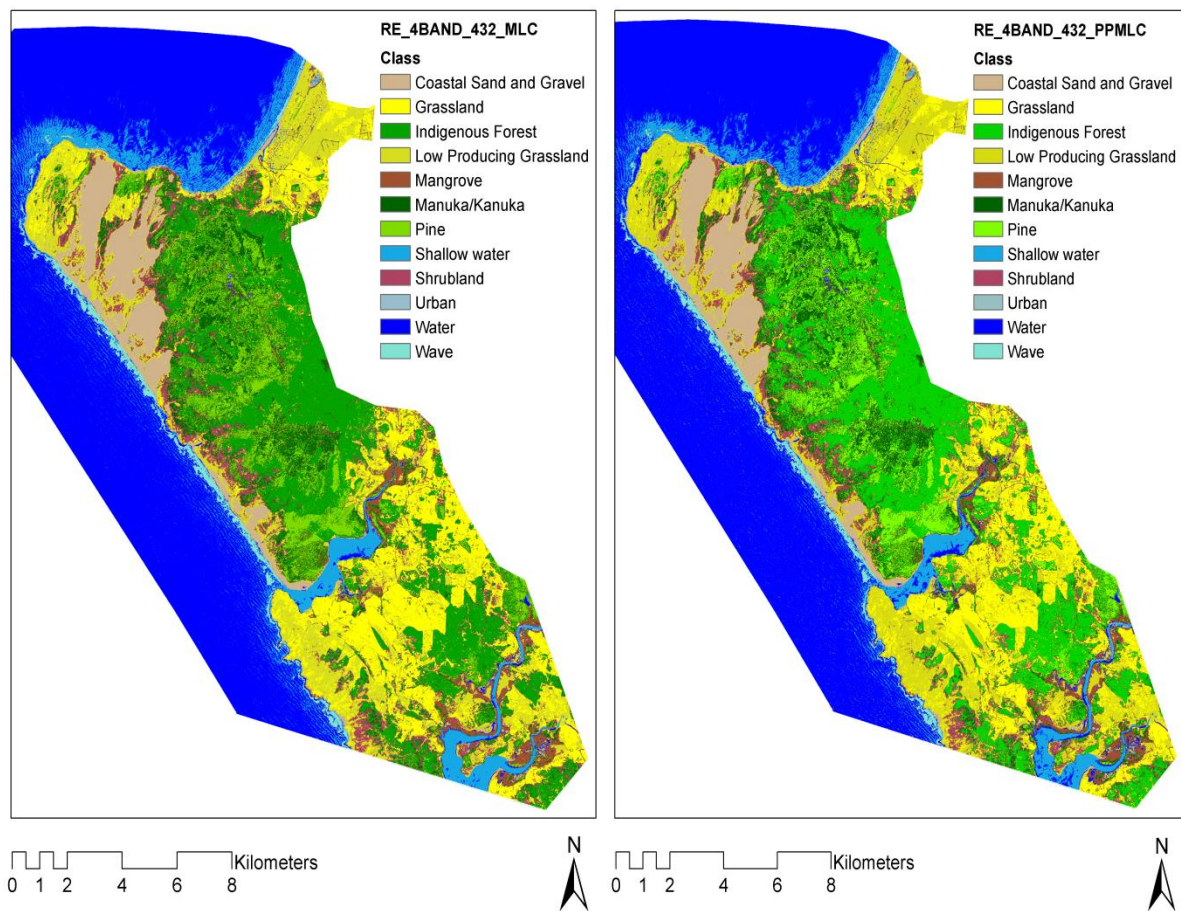
Figure 4.13 RapidEye Classified images (4BAND_432_MLC/PPMLC)

The RapidEye image (432) without the Red-Edge band (same as L7 with 432 band combination) was classified by MLC and PPMLC classifiers. The accuracy assessment of RE _4band (PPMLC) classified image was higher than RE_4band (MLC) image (Figure 4.1).The mixture of PP and MLC algorithm generated slightly higher overall accuracy of 81.67% with Kappa of 0.79 while for the RE_4band (432) image using MLC algorithm only achieved 80.41% of overall accuracy with Kappa value of 0.77. Both images had high producer's accuracies for grassland, shrub-land, coastal sand and gravel, low producing grassland, shallow water and water classes (Tables 4.23 and 4.25). For the pine and manuka/kanuka classes, the moderate accuracies were recorded while the wave class for RE_4band (PPMLC) showed highest accuracy of 100%.

The high user's accuracies were observed for similar classes of both classified images (RE_4band_ ML/PPMLC) (table 4.23 and 4.25). The mangrove class from RE_PPMLC image and the wave class from RE_MLC image showed highest accuracies (100%) but the pine category had a low user's accuracy of 34% in the maximum likelihood classifier. Kappa statistics indicated good classification performance for water, shallow water, low producing indigenous forest, coastal sand and gravel classes for both classified images while pine had low classification execution.

4.3 The Comparison of the RapidEye Classified Data with the LCDB2 Data

According to the results obtained in this study, the best classification performance including the combination of maximum likelihood with parallelepiped algorithm (PPMLC) in terms of the highest accuracy assessment result was considered as classifier to classify the RapidEye data with different band combinations (5,4,3 and PC12VI). The land cover databases (LCDB2) from the Ahipara region were used to compare with the RapidEye classified images.

Three different classification approaches were implemented and the results were indicated in Tables 4.26, 4.27 and Figure 4.14. For both RapidEye classified images RE_543_PPMLC and RE_PC12VI_PPMLC, 13 classes were identified including low producing grass, wave, grassland, pine forest, water, rock, wetland, shallow water, mangrove, coastal sand and

gravel, indigenous forest, shrubland and manuka/kanuka while the classes of low producing grass, grass, pine forest, water, mangrove, coastal sand and gravel, indigenous forest, shrubland and manuka/kanuka were observed for LCDB2 classified data. The rock, wetland and shallow water classes were the most typical and specific features extracted from the RapidEye classified data while these features were not indicated in the LCDB2 classification (Table 4.26 and Figure 4.16).

Table 4.26 The area of the classified data by different approaches (ha)

Class Name	RapidEye_543_PPMLC	LCDB2 Classification	RapidEye_PC12VI_PPMLC
Low Producing Grassland	596.32	806.26	930.45
Wave	150.96	0	221.70
Grassland	1137.03	980.02	570.52
Pine Forest	110.76	141.70	96.68
Water	362.26	271.46	232.05
Rock	7.69	0	8.69
Wetland	26.02	0	123.58
Shallow water	143.08	0	182.62
Mangrove	158.05	161.86	233.29
Coastal Sand and Gravel	663.26	727.22	565.45
Indigenous Forest	197.58	286.10	444.66
Shrubland	368.19	109.76	493.75
Manuka/Kanuka	712.56	809.13	530.29

For Re_543_PPMLC and RE_PC12VI_PPMLC, the rock class's area was 7.69 and 8.69 (ha) respectively (Table 4.26), and similarly, the same percentage of 0.2% of rock area was estimated for both RE classified images (Table 4.27).

Moreover, for RE_PC12VI_PPMLC image more area of wetland (123.58 ha with 2.7%) and shallow water (185.26 ha with 3.9%) classes were observed than the classified data of RE_543_PPMLC in the same classes on the amount of area in 26.02 ha with 0.6% and 143.08 ha with 3.1% (Tables 4.26, 4.27 and Figure 4.14).

Table 4.27 The percentage of the area of the classified data by different approaches (ha)

Class Name	RapidEye_543_PPMLC % of Area	LCDB2 Classification % of Area	RapidEye_PC12VI_PPMLC % of Area
Low Producing Grassland	12.9	18.8	20.1
Wave	3.3	0	4.8
Grassland	24.5	22.8	12.3
Pine Forest	2.4	3.3	2.1
Water	7.8	6.3	5
Rock	0.2	0	0.2
Wetland	0.6	0	2.7
Shallow water	3.1	0	3.9
Mangrove	3.4	3.8	5
Coastal Sand and Gravel	14.3	16.9	12.2
Indigenous Forest	4.3	6.7	9.6
Shrubland	7.9	2.6	10.7
Manuka/Kanuka	15.4	18.8	11.4
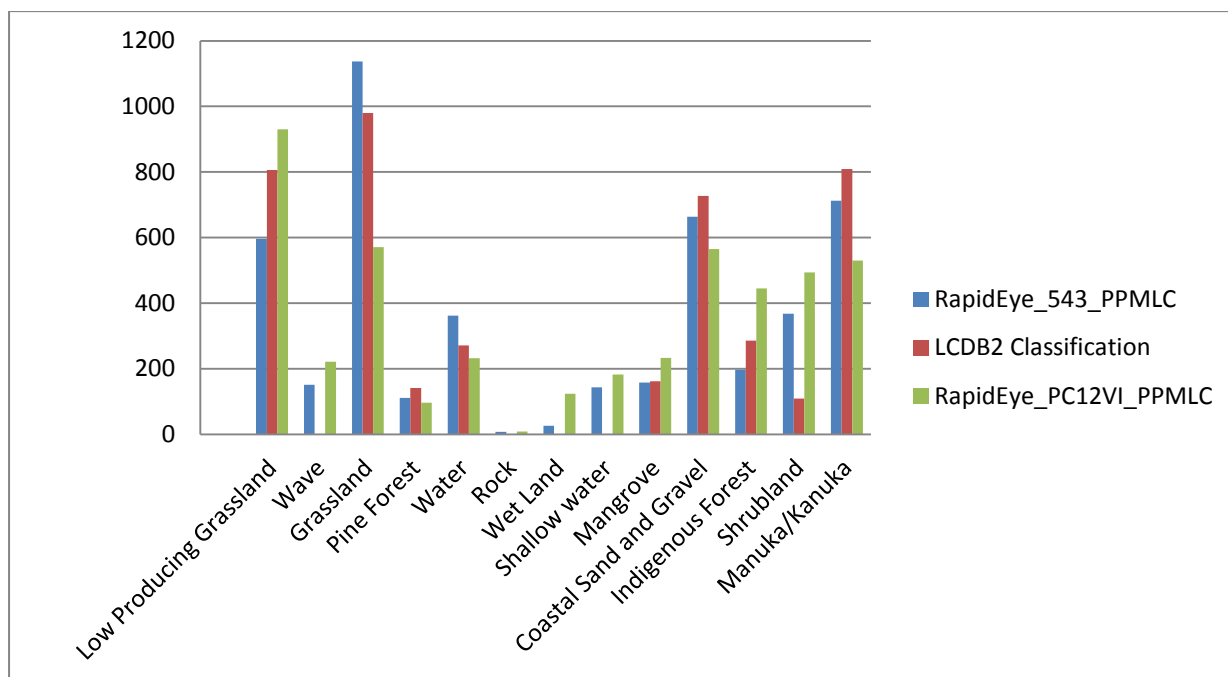
Figure 4.14 The results of the area of the classified data for the Landsat 7 (LCDB2) and RapidEye images

The mixture of parallelepiped with maximum likelihood algorithms created good results when they were applied on the RapidEye data with the band combination of red-edge, IR, red and also PC1, 2 and vegetation index (Figures 4.17 and 4.18). The results were accurate in determining the rock (along the coastline), wetland and shrubland classes (Figure 4.15 A and B), while these features were not revealed in the results of LCDB2 classification (Figures 4.15 C and 4.19).
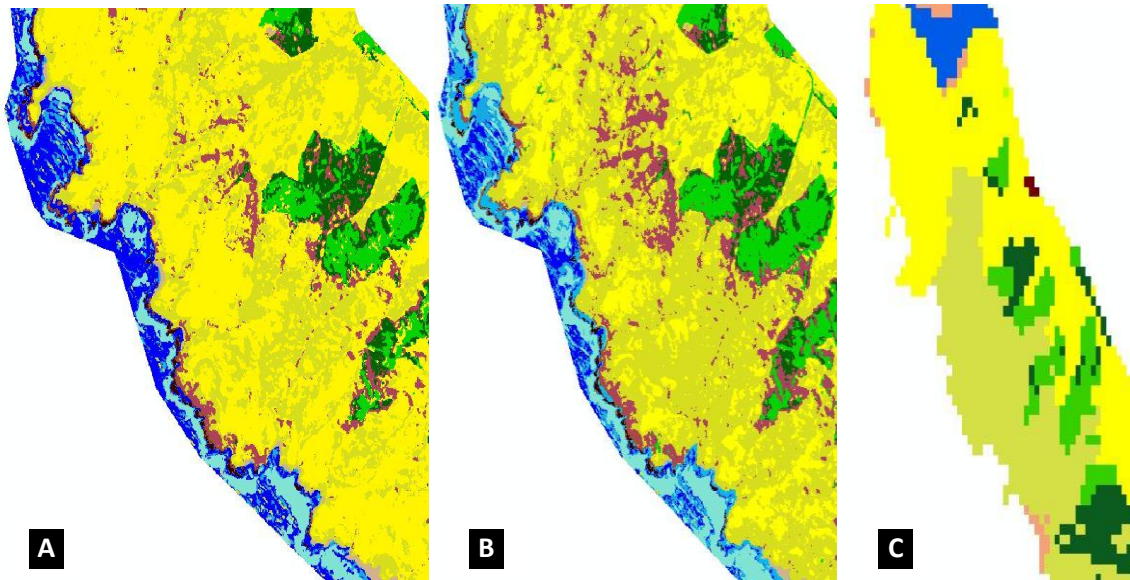
Figure 4.15 The classified images of RE_543_PPMLC (A), RE_PC12VI_PPMLC (B) and LCDB2 (C) from the South of Herekino Harbour area.

The Figure 4.16 indentified the difference between the distributions of features extracted from the RE_543_PPMLC, RE_PC12VI_PPMLC and Landsat 7 (LCDB2) classified images. For the LCDB2 classification the features such as coastal sand and gravel, pine forest, grass, low producing grassland, indigenous forest and shrubland were classified homogeneity into the separate patches (Figure 4.16 C). Whereas, applying the combination of maximum likelihood and parallelepiped classifiers on RE_543 and RE_PC12VI images produced more accurate classification results in distinguishing variations in vegetation covers, for instance, the grass, low producing grass and shrubland classes were identified as they were extracted from the remotely sensed data (Figure 4.16 A and B).
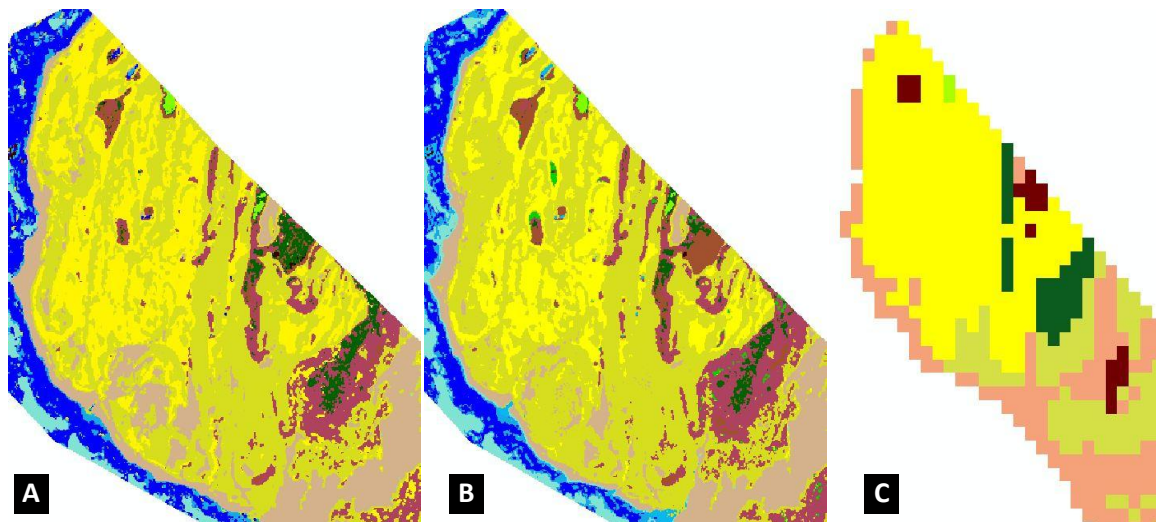
Figure 4.16 The classified images of RE_543_PPMLC (A), RE_PC12VI_PPMLC (B) and LCDB2 (C) from the North of Ahipara region.
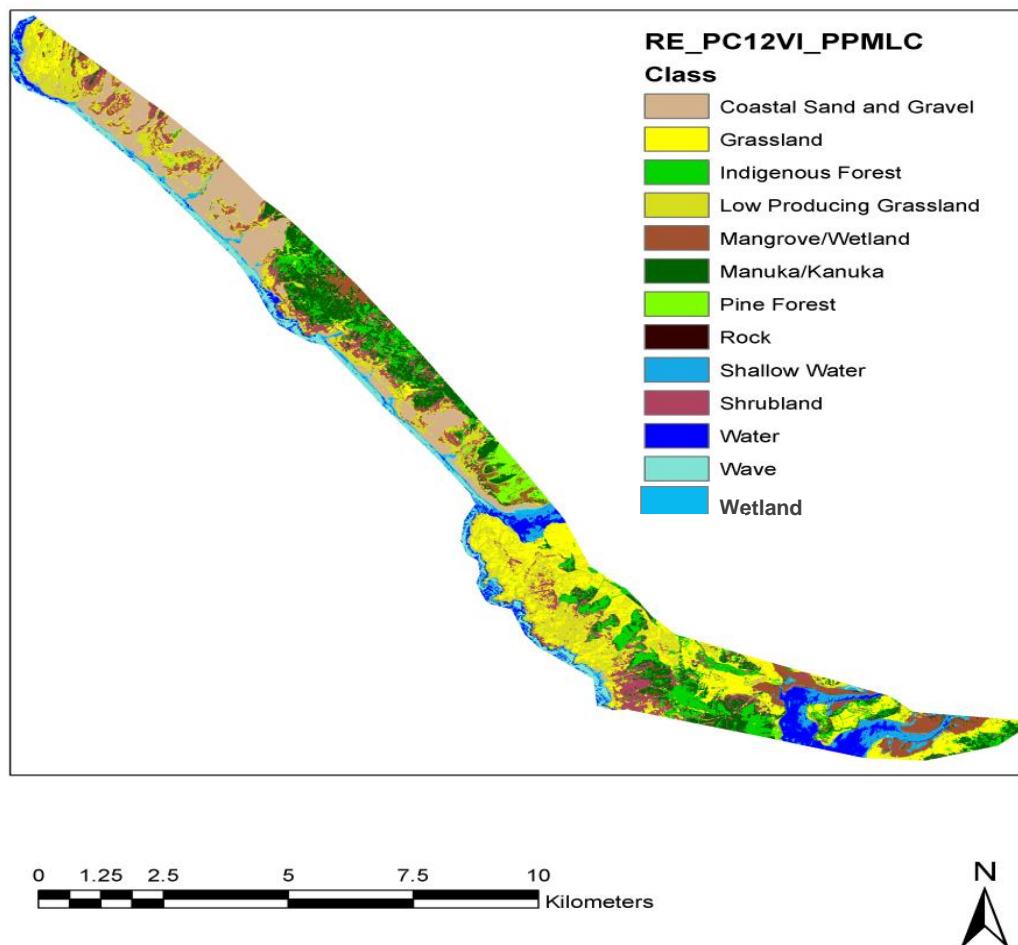
Figure 4.17 RapidEye classified image (PC12VI_ PPMLC) – Ahipara region
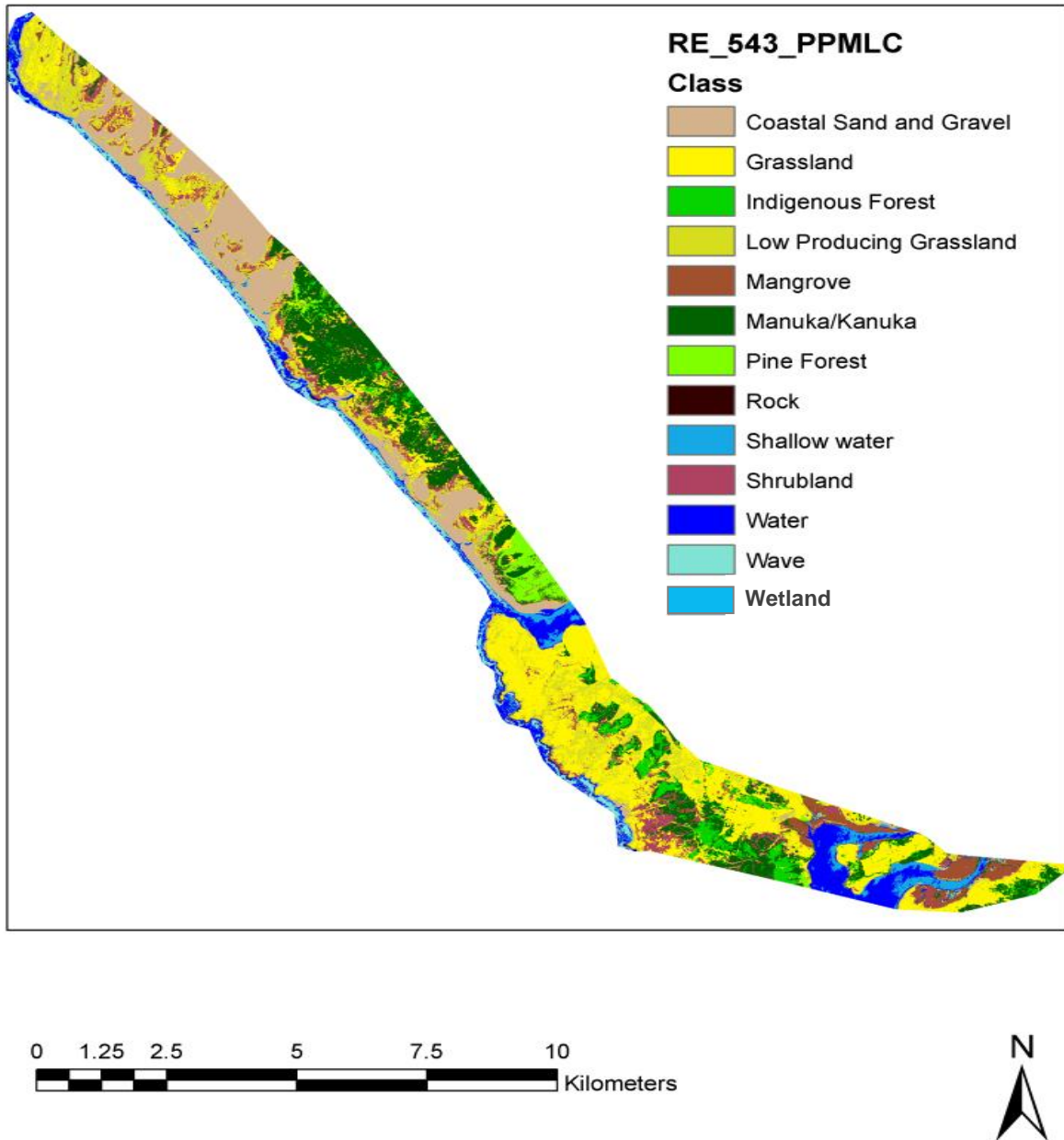
Figure 4.18 RapidEye classified image (543_ PPMLC) – Ahipara region
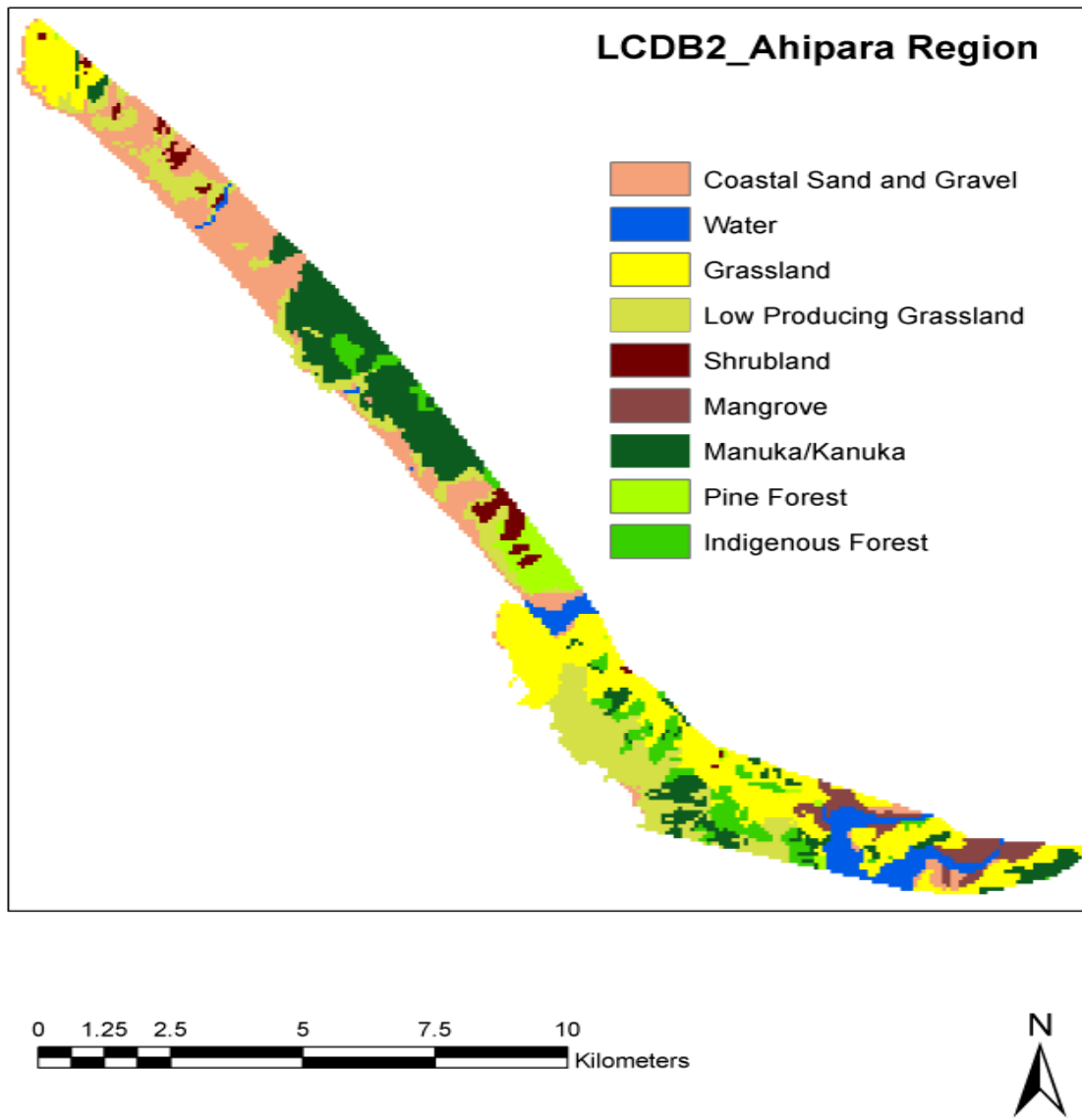
Figure 4.19 Landsat 7 classified image (LCDB2) – Ahipara region

Chapter 5

Discussion and Conclusion

5.1 Image Classification and Analysis

This study demonstrated the use of remote sensing and GIS techniques to classify the land-cover over the Ahipara region as well as the evaluation of the Landsat 7 and RapidEye classified images accuracies from different supervised classification algorithms and multi band combinations.

5.2 Accuracy Assessment of RapidEye and Landsat 7 Classified Images

A false colour image (band combination 4, 3, 2) and a combined image of principle component 1 and 2 layers with vegetation index layer of Landsat 7 data were utilized. After employing MLC and combination of MLC with PP algorithms on each image, the land-cover areas were classified into eleven categories, including shallow water, grassland, low producing grassland, mangrove, coastal sand and gravel, wave, pine forest, manuka/kanuka, shrub-land, indigenous forest and water.

The accuracy assessment results indicated that the classified images of L7_ PPMLC (432) and L7_ PC12VI_PPMLC with 78.71% and 79.78% overall accuracies with the overall Kappa statistics of 0.76 and 0.77, respectively had higher overall classification accuracies than the classified images of L7_MLC (432) and L7_ PC12VI_MLC with 76.79% and 74.07% overall accuracies with the overall Kappa statistics of 0.74 and 0.71, respectively. As the results represent that higher accuracy of the Landsat ETM+ image classification is generated when the combination of layers, which contain of the first and second principal components and vegetation index with the combined of maximum likelihood and parallelepiped algorithms were applied. As the Kappa statistic results assign highest classification performance was distinguished for L7_PC12VI_PPMLC classified image to compare with other Landsat classified images. According to Landis and Koch (1977) the

values of Kappa between 0.4 and 0.8 indicate moderate agreement. For the Landsat classified images the results of accuracy assessments were acceptable in discriminating the Ahipara land-cover features and classes. The studies have shown that the Landsat satellite acquired data with applying post processing remote sensing procedures can provide a significant source and method to classify the land use and land cover over in the study area. The overall accuracy was identified from 74% to 93% using Landsat imagery to classify LULC included forests, wetlands, grasslands, shrubs, water, urban areas, croplands and so on (MfE, 2012; Munoz-Villers & Lopez-Blanco, 2008 and Paiboonvorachat, 2008).

In addition, the accuracy classification performances were assessed for the RapidEye classified images. The RapidEye images, including a degraded spatial resolution image (30m_similar to L7 imagery), 4 layer stacked bands (Red-Edge band was excluded) with 4, 3 and 2 band combination (similar to L7 false colour image (432)), a combination of the NIR, Red-Edge (specifically considered for vegetation characterization) and Red band (543), and the mixture of the principle components 1, 2 with the vegetation index layer (PC12VI). The supervised classification approach utilizing MLC and a combination of MLC and PP algorithms were employed to classify all four different images, so that after classification process, eight RE classified images were generated.

The accuracy assessment results signified that almost all classified RapidEye images except RE_ DEGRADED _MLC (78%) had high overall classification accuracy over 80% (Table 4.1 and Figure 4.1). However, the overall Kappa statistic of over 0.8 identified for four RE classified images, including RE_543_PPMLC (0.85), RE_PC12VI_PPMLC (0.84), RE_PC12VI_MLC (0.83) and RE_543_MLC (0.82), which distinguished a high level of classification performance, while for RE_ degraded and 4band classified images applying MLC/PPMLC classifiers assigned moderate accuracies in terms of Kappa value of 0.76, 0.77, 0.78 and 0.79, respectively.

In this study as the results for twelve different classification approaches have revealed that using a combination of maximum likelihood with parallelepiped algorithm (PPMLC) can improve the accuracy classification performance for the Landsat ETM+ and RapidEye images. According to Younggu (2007) utilizing the mixture of MLC and PP classifiers provided higher accuracy of the classification for Landsat7 and Quickbird images.

For RE_543_PPMLC and RE_PC12VI_PPMLC images, almost all vegetation classes, including pine forest, grassland, low producing grassland, manuka/kanuka, indigenous forest had high Kappa statistics, producer's and user's accuracies. The higher accuracies were indicated due to using red-edge band (Bindel, Hese, Berger, & Schmullius, 2011) that combined with NIR and red band for RE_543 image and also applying principle component layers 1 and 2 with vegetation index layer on RE image. The RapidEye satellite was specifically designed to monitor vegetation, cropland and agriculture purposes with its red-edge band that is especially sensitive to detect vegetation condition (Losel, 2009).

For the Landsat ETM+ classified images, some classification errors characterized among vegetation classes that can be caused by low spatial resolution and lack of Red-Edge band, so that the separability of vegetation classes were not signified as high accuracy classification performance. The same misclassifications were reported in classifying the land cover in Mediterranean area (Ozdemir, Asan, Koch, Yesil, Ozkan, & Hemphill, 2005). In other study, Baskent and Keles (2005) identified some errors in the results of classification between cropland and forest. As the results indicated the lowest classification accuracy among the all the RapidEye classified images were recorded for the RE_DEGRADED_MLC and RE_ DEGRADED _PPMLC image with 78.85% and 80.28% overall accuracy and Kappa statistics of 0.76 and 0.77, respectively that it can be due to the lower spatial resolution of the degraded RE image (30m) compared to orthorectified RapidEye image (5m).

In summary, the classified images of RE_543_PPMLC, RE_PC12VI_PPMLC, RE_PC12VI_MLC and RE_543_MLC with over 80% overall accuracy and Kappa statistic of over 0.8 represented the highest accuracy assessment results among other images, as well as they indicated good classification performance between all the classified images of RapidEye and Landsat ETM+ data.

5.3 LCDB2 and RapidEye Classified Data Comparison

The land cover classification of the Ahipara region from the subset of LCDB 2 data identified the nine categories of land cover (Table 4.27). For RapidEye data (543 and PC12VI), a combination of maximum likelihood with parallelepiped algorithm (PPMLC) was applied to classify remotely sensed data over the study area. As the results of RE classified data

signified, the most accurate classification performances were determined for RE_543_PPMLC, RE_PC12VI_PPMLC images, so that these images were considered to compare with LCDB2 classification.

As the results revealed, the classes of rock, shallow water and wetland were extracted and identified from both RapidEye images while for LCDB2, the data were determined into nine land cover classes including low producing grassland, grassland, pine forest, water, mangrove, coastal sand and gravel, indigenous forest, shrubland and manuka/kanuka, so that the classes of rock, wetland and shallow water were not observed. According to the results of the classification processes and comparative assessments between LCDB2 and RE data, it was concluded that the images of RE_543_PPMLC and RE_PC12VI_PPMLC had higher classification performance in discriminating land cover types than the LCDB2 classification.

5.4 Conclusions

This study demonstrated the benefits of using higher resolution imagery (represented by RapidEye imagery with 5m orthorectified, multispectral data) compared to lower resolution imagery (free of charge Landsat-7 ETM+ data at 30m resolution) and applying different classification approaches to classify remotely sensed data (RE & L7). The classification approaches were compared in terms of classification accuracy and included different band combinations, and different classification algorithms. Moreover, a comparative analysis of land cover classified using RapidEye imagery and the Land Cover Databases Version 2 (LCDB 2) from the Ministry for the Environment were conducted.

In this study, different methods of image classification were tested to classify the Landsat 7 and RapidEye acquired data over the Ahipara region. In addition, a comparative analysis of the results of the accuracy assessment for each of the classified images was conducted.

Four images from the Landsat 7 data and eight images from the RapidEye data were generated by applying different band (432, 543) and layer (PC12VI) combinations. In addition, the supervised classification algorithms were used to classify twelve remotely sensed images by the maximum likelihood classifier (MLC) and combination of MLC with

the parallelepiped algorithm. The results of the classified images for both sensors (L7 and RE) indentified that all classified images by PPMLC had a higher accuracy and Kappa statistic than the classified images used by MLC approach. Furthermore, the Kappa statistics and the overall accuracies represented that the Red-Edge band from the RapidEye system combined with NIR and Red can improve the classification performance as it is sensitive to distinguish in vegetation cover.

This study revealed that one of the most accurate procedure for classifying the RapidEye image of the study area was a combination of principal components and vegetation index layers (PC12VI) while the degraded images (RE with 30m spatial resolution) and also the RE images with 432 band combination had lower accuracy assessment results.

High spatial, spectral and temporal resolution of The RapidEye data represented more accurate classification performance (PC12VI_PPMLC and 543_PPMLC) with useful information in classifying the study area in Ahipara region whereas the Landsat 7 image indicated moderate classification accuracy, as well as the LCDB2 data had lower performance in identifying the land cove types.

5.5 Recommendations

The results of this research revealed that due to the heterogeneous landscape characteristics of the study area, the use of RapidEye multispectral images will improve land use/land cover classification. The five RE satellites have advantages because of their unique ability to acquire high spatial resolution (5m, orthorectified) data, the high temporal resolution, which have a daily revisit capability anywhere on Earth, so that RE imagery can provide a good coverage of seasonal changes of vegetation phenology (Bahls and Kleinschmit, 2011).

In addition, the mixture of maximum likelihood and parallelepiped algorithms applied to remotely sensed data can improve the classification accuracy assessment results. Also, it is recommended that high classification performance can be achieved when the combination of first and second of principle components with vegetation index layer (PC12VI) are used for classifying the satellite image.

Finally, the methods used in this study for the land cover and land use classification should be applied in other areas in New Zealand instead of using Landsat 7 ETM+ or Spot imagery (LCDB1 and 2).

References

Al-Ahmadi, F. S., & Hames, A. S. (2009). Comparison of four classification methods to extract land use and land cover. *Earth Sci., 20*(1), 167-191. Retrieved from http://www.cob.rb.kau.edu.sa/

Aggarwal, S. (2003). Principles of Remote Sensing. Satellite Remote Sensing and GIS Applications in Agricultural Meteorology. *Proceedings of a Training Workshop, Dehra Dun, India,* 23-38. Retrieved from http://www.wmo.int/pages/prog/wcp/agm/publications/AGM8_en.php

Arias, S., Gomez, H., Prieto, F., Boton, M., & Ramos, R. (2009). *Satellite Image Classification by Self-Organized Maps on GRID Computing Infrastructures*. Paper presented at the second EELA-2 Conference. Retrieved from http://www.cetaciemat.es/attachments/320_Satellite_Image_Classification_by_%20SOM_on_GRID.pdf

Ashraf, S., Brabyn, L., Hicks, B. J., & Collier, K. (2010). Satellite remote sensing for mapping vegetation in New Zealand freshwater environments: A review. *New Zealand Geographer, 66*(1), 33-43.

Atmopawiro, Y. A. (2004). *Sub-Pixel And Maximum Likelihood Classification Of Landsat Etm+ Images For Detecting Illegal Logging And Mapping Tropical Rain Forest Cover Types In Berau, East Kalimantan, Indonesia*. Retrieved April 28th, 2012, from www.itc.n: http://www.itc.nl/library/Papers_2004/peer_conf/hussin_sub.pdf

Bahls, A., & Kleinschmit, B. (2011, June). *Using RapidEye data for detecting vegetation changes caued by exteme hydrological events in the Elbe estuary*. Paper presented at CoastGIS, Oostende, Belgium.

Bajjouk, T., Populus, J. & Guilaumont, B. (1998). Quantification of subpixel cover fractions using principal component analysis and a linear programming method: Application to the coastal zone of Roscoff (France), *Remote Sensing of Environment, 64*(2)*,* 153-165. doi: 10.1016/S0034-4257(97)00175-2

Bajjouk,T., Guilaumont, B., & Populus, J. (1996). Application of airborne imaging spectrometry system data to intertidal seaweed classification and mapping, *Hydrobiologia*, *327*, 463-471.

Banko, G. (1998). *A review of assessing the accuracy of classifications of remotely sensed data and of methods including remote sensing data in forest inventory* (Interim Report: IR-98-081). Laxenburg, Austria: International Institute for Applied System Analysis. Retrieved from http://www.iiasa.ac.at/Publications/Documents/IR-98-081.pdf

Baskent, E. Z., Keles, S. (2005). Spatial forest planning: A review. *Ecol. Model, 188*, 145-173.

Behnia, P. (2005). Comparison between four methods for data fusion of ETM+ multispectral and pan images. *Geo-Spatial Inf Sci, 8*, 98-103.

Belluco, E., Camuffo, M. and Ferrari, S. (2006). Mapping salt-marsh vegetation by multispectral and hyperspectral remote sensing. *Remote Sensing of Environment, 105*, 54-67.

Bindel, M., Hese, S., Berger, C., & Schmullius, C. (2011). Evaluation of red-edge spectral information for biotope mapping using RapidEye. *Proc. of SPIE, 8174.* doi: 10.1117/12.898007

Boyle, S. J., Tsanis, I. K., & Kanaroglou, P. S. (1998). Developing Geographic Information Systems for Land Use Impact Assessment in Flooding Condition. *Journal of Water Resources Planning and Management, 124*(2), 89-97.

Cakir, H.I., Khorram, S., & Nelson, S.A.C. (2006). Correspondence analysis for detecting land cover change. *Remote Sens Environ, 102*, 306-17.

Campbell, J. B. (2002). *Introduction to remote sensing* (3rd ed). New York: The Guilford Press.

Canty, M. J., Nielsen. A., & Schmidt, M. (2004). Automatic radiometric normalization of multitemporal satellite imagery. *Remote Sensing of Environment , 91*, 4411-451.doi: 10.1016/j.rse.2003.10.024

Carreiras, J.M.B., Pereira, J.M.C., & Shimabukuro,Y.E. (2006). Land-cover mapping in the Brazilian Amazon using SPOT-4 vegetation data and machine learning classification methods. *Photogrammetric Engineering and Remote Sensing, 72*, 897-910.

Carreiras, J.M.B., Pereira, J.M.C., Campagnolo, M.L., & Shimabukuro, Y.E., (2006b). Assessing the extent of agriculture/pasture and secondary succession forest in the Brazilian Legal Amazon using SPOT VEGETATION data. *Remote Sensing of Environment, 101*(3), 283-298. doi:10.1016/j.rse.2005.12.017

Chandra, S., Ziemke, J. R., Bhartia, P. K., & Martin, R. V. (2002). Tropical tropospheric ozone: Implications for dynamics and biomass burning. *J. Geophys. Res., 107*(D14), 4188. doi:10.1029/2001JD000447

Chavez, P. S. (1996). Image-based atmospheric corrections-revisited and improved. *Photogrammetric engineering and remote sensing, 62*(9), 1025-1036. Retrieved from www.asprs.org/a/publications/pers/ 96journal/september/1996_sep_1025-1036.pdf

Colby, J. D., & Keating, P. L. (1998). Land Cover Classification Using Landsat TM Imagery in the Tropical Highlands: the Influence of Anisotropic Reflectance. *International Journal of Remote Sensing , 19*(8), 1479-1500.doi: 10.1080/014311698215306

Combe, JP., Launeau, P., Carrere, V., Despan, D., & Meleder, V. (2005). Mapping microphytobenthos biomass by non-linear inversion of visible-infrared hyperspectral images. *Remote Sensing of Environment, 98*, 371-387.

Congalton, R. G. (1991). A review of assessing the accuracy of classifications of remotely sensed data. *Remote Sensing of Environment, 37*, 35-40.doi: 10.1016/0034-4257(91)90048-B

Conning, L. (1998). *Natural areas of Ahipara Ecological District* (New Zealand protected natural areas programme No. 39). Retrieved from www.conservation.net.nz/.../ahipara-ecological-district.pdf

Coppin, P., & Bauer, M. (1996). Digital Change Detection in Forest Ecosystems with Remote Sensing Imagery. *Remote Sensing Reviews, 13*, 207-234.

Coppin, P., Jonckheere, I., Nackaerts, K., & Muys, B. (2004). Digital change detection methods in ecosystem monitoring: a review. *International Journal of Remote Sensing, 25*(9), 1565-1596.

Czaplewski, R. (2003). Can a sample of Landsat sensor scenes reliably estimate the global extent of tropical deforestation? *International Journal of Remote Sensing, 24*(6), 1409-1412.

Defries, R.S., & Chan, J. (2000). Multiple criteria for evaluating machine-learning algorithms for land cover classification from satellite data. *Remote Sensing of Environment, 74*, 503-515doi:10.1016/S0034-4257(00)00142-5

Department of Conservation. (2010). *Land cover Database* . Retrieved May 2012, from www.mfe.govt.nz/environmental-reporting: http://www.mfe.govt.nz/environmental-reporting/about/tools-guidelines/classifications/land/

Deysher, L. E. (1993). Evaluation of remote sensing techniques for monitoring giant kelp Population. *Hydrobiologia*, *260/261*, 307-312.

Domacx, A, Suzen, ML. (2006). Integration of environmental variables with satellite images in regional scale vegetation classification. *Int J Remote Sens, 27*,1329-1350

Du, Y., & Teillet, P. M. (2002). Radiomettric normalization of multitemporal high-resolution images with quality control for land cover change detection. *Remote Sensing of Environment*, *82*, 123-134.doi: 10.1016/S0034-4257(02)00029-9

El-Mezouar, M. C., Taleb, N., Kpalma, K., & Ronsin, J. (2011). An IHS-based fusion for color distortion reduction and vegetation enhancement in IKONOS imagery. *Geoscience and Remote Sensing*, *49*(5): 1590-1602.

Fitzpatrick-Lins, K. (1981). Comparison of sampling procedures and data analysis for a land use and land-cover map. *Photogrammetric Engineering and Remote Sensing, 47*(3), 343-351.

Foody, G. M. (2002). Status of land cover classification accuracy assessment. *Remote Sensing of Environment, 80*(1), 185-201. doi: 10.1016/S0034-4257(01)00295-4

Franklin, S.E., & Wulder, M.A. (2002). Remote sensing methods in medium spatial resolution satellite data land cover classification of large areas. *Progress In Physical Geography, 26*(2), 173-205.doi: 10.1191/0309133302pp332ra

Freeman, A., Chapman, B., & Siqueira, P. (2002). The JERS-1 Amazon Multi-season Mapping Study (JAMMS): Science Objectives and Implications for Future Missions. *International Journal of Remote Sensing*, *23*(7), 1447-1460. doi:10.1080/01431160110092975

Fromard, F.,Vega, C., & Proisy, C. (2004). Half a century of dynamic coastal affecting mangrove shoreline of French Guiana: A case study based on remote sensing data analyses and field surveys. *Marine Geology, 208*(2), 265-280. doi: 10.1016/j.margeo.2004.04.018

Fussell, J., D. Rundquist, and J. A. Harrington, 1986. On Defining Remote Sensing. *Photogrammetric Engineering and Remote Sensing, 52*,1507-1511.

Fyfe, J.E., & Israel, S.A. (1996, July). *A widow an underwater habitat: Quantifying differences in giant kelp beds using colour aerial photographs and image processing software*. Paper presented at 8th Colloquium of the Spatial Information Research Centre (SIRC '96), Dunedin, University of Otago. Retrieved from http://divcom.otago.ac.nz/conferences/geocomp97/cd-rom/sirc96/papers/fyfe.pdf

Gao, J. (1999). A comparative study on spatial and spectral resolutions of satellite data in mapping mangrove forests. *International Journal of Remote Sensing, 20*, 2823-33.

Gao, J., Chen, H.F., Zhang, Y., & Zha, Y. (2004). Knowledge based approaches to accurate mapping of mangroves from satellite data. *Photogrammetric Engineering and Remote Sensing, 70*, 1241-48.

Goetz, S.J. (1997). Multi-sensor analysis of NDVI, surface temperature and biophysical variables at a mixed grassland site. *International Journal of Remote Sensing, 18*(1), 71-94. doi: 10.1080/014311697219286

Govender, M., Dye, P. J., Weiersbye, I. M., Witkowski, E. T. F., & Ahmed, F. (2009). Review of commonly used remote sensing and ground-based technologies to measure plant water stress, *Water SA*, *35*(5), 741-752.

Guillaumont, B., Bajjouk, T., & Talec, P. (1997). Seaweed and remote sensing: a critical review of sensors and data processing. In: Round FE, Chapman DJ (eds) Progress in Phycological Research. *Biopress*, pp 213-282

Guillaumont, B., Callens, L., & Dion, P. (1993). Spatial-Distribution and Quantification of Fucus Species and Ascophyllum-Nodosum Beds in Intertidal Zones Using Spot Imagery. *Hydrobiologia, 261,* 297-305.

Guyot, G., & Gu, x. (1994). Effect of Radiometric Corrections on NDVI-Determined from SPOT-HRV and Landsat-TM Data. *Remote Sensing of Environment, 49,169-180.* doi: <u>10.1016/0034-4257(94)90012-4</u>

Hagness, S.C., & Taflove, A. (2005). *Computational Electrodynamics: The Finite-Difference Time-Domain Method* (3rd ed). London, UK: Artech House Publishers.

Hall, F. G., Strebel, D. E., & Nickeson, J. E. (1991). Radiometric rectification: toward a common radiometric response among multidate, multisensor images. *Remote Sens Environ, 35*, 11-27.

Hansen, M., Dubayah, R., & Defries, R. (1996). Classification trees: An alternative to traditional land cover classifiers. *International Journal of Remote Sensing, 17*(5), 1075-1081.doi: <u>10.1080/01431169608949069</u>

Harvey, K., & Hill, J.E. (2001). Vegetation mapping of a tropical freshwater swamp in the Northern Territory, Australia: a comparison of aerial photography, Landsat TM and SPOT satellite imagery. *Remote Sens Environ, 22*, 2911-2925.

Henry, J.B., Chastanet, P., Fellah,K. & Desnos, Y.L. (2006). Envisat multi-polarized ASAR data for flood mapping, *International Journal of Remote Sensing,* 27(10), 1921-1929.

Hester, D. B., Cakir, H. I., Nelson, S. A. C., & KHorram, S. (2008). Per-pixel classification of high spatial resolution satellite imagery for urban land cover mapping, *Photogrammetric Engineering and Remote Sensing*, *74*, 463-471.

Hixson, M., Scholz, D., Fuhs, N., & Akiyama, T. (1980). Evaluation of several schemes for classification of remotely sensed data. *Photogrammetric Engineering and Remote Sensing, 46*(12), 1547-1553.

Holden, H. & LeDrew, E. (1998). Spectral discrimination of healthy and nonhealthy corals based on cluster analysis, principal components analysis and derivative spectroscopy. *Remote Sensing of Environment, 65*, 217-224.

Huang, S. & Siegert, F. (2006). Land cover classification optimized to detect areas at risk of desertification in North China based on SPOT vegetation imagery. *Journal of Arid Environments, 67*, 308-327 doi: <u>10.1016/j.jaridenv.2006.02.016</u>

Hurd, C. L., Nelson, W. A., Falshaw, R., & Neill, K.F. (2004). History, current status and future of marine macroalgal research in New Zealand: Taxonomy, ecology, physiology and human uses. *Phycological Research, 52,* 80-106. Retrieve February 25, 2012.

Israel, S. A., Fyfe, J. E. (1996). *Determining the sensitivity of SPOT XS imagery for monitoring intertidal and sublittoral vegetation of Otago Harbour.* Wellington

Jakomulska, A., Zagajewski, B., & Sobczak, M. (2003). Field remote sensing techniques for mountains vegetation investigation. In M. Habermeyer, A. Mueller & S. Holzwarth (Eds.), *3rd EARSeL Workshop on Imaging Spectroscopy* (580-596). Paris: EARSeL.

Jang, J. D., Bartholome, E., Viau, A.A., et al. (2006). Neural network application for cloud detection in SPOT VEGETATION images. *Int J Remote Sens, 27*, 719-36.

Jensen, J. R. (1996). *Introductory Digital Image Processing: A remote Sensing Perspective* (2nd ed.). Englewood Cliffs, New Jersey: Prentice-Hall.

Jensen, J. R. (2005). *Introductory Digital Image Processing: A Remote Sensing Perspective* (3rd ed.). New Jersy: Pearson Education, Inc.

Kerr, J., & Ostrovsky, M. (2003). From space to species: Ecological applications for remote sensing. *Trends in Ecology and Evolution, 18*, 299–314.

Koordinates. (n.d). *Northland Aerial Photography - Areas of Kaitaia, Karikari Peninsula to the Bay of Islands Far North 2000.* Retrieved September 14, 2011, from http://koordinates.com/layer/1203-northland-aerial-photography-areas-of-kaitaia-karikari-peninsula-to-the-bay-of-islands-far-north-2000

Lambin, E. F., Turner, B. L., & Helmut, J. (2001). The causes of land-use and land-cover change: moving beyond the myths. *Glob Environ Chang, 11*, 261-9.

Landis, J. R., & Koch, G. G. (1977). An application of hierarchical kappa-type statistics in the assessment of majority agreement among multiple observers. *Biometrics,* 33(2), 363- 374.

Langley, S.K., Cheshire, H. M., & Humes, K. S. (2001). A comparison of single date and multitemporal satellite image classifications in a semi-arid grassland. *J Arid Environ ,490,* 401-11.

Lefsky, M. A., Turner, D. P., Guzy, M., & Cohen, W. B. (2004). Combining lidar estimates of aboveground biomass and Landsat estimate of stand age for spatially extensive validation of modelled forest productivity. *Remote sensing of Environment, 95*, 549-558.

Levin, N., Ben-Dor, E., Singer, A. (2005). A digital camera as a tool to measure color indices and related properties of sandy soils in semi-arid environments. *International Journal of Remote Sensing, 26*(24), 5475-5492.

Li, L., Ustin, S.L., & Lay, M. (2005). Application of multiple end-member spectral mixture analysis (MESMA) to AVIRISimagery for coastal salt marsh mapping: a case study in China Camp, CA, USA. *Int J Remote Sens, 26,* 5193-5207.

Lillesand, T. M., Kiefer, R. W., & Chipman, J. W. (2004). *Remote sensing and image interpretation* (5th ed.). United States: John Wiley & Sons, Inc.

Lin, C., & Päivinen, R. (1999, June). *Remote sensing and forestry information needs in the 21st century.* Paper presented at the Remote Sensing and Forest Monitoring Conference, Poland.

Liu, X., Skidmore, A. K. & Van Oosten, H. (2002). Integrationof classification methods for improvement of land cover map accuracy. *ISPRS Journal of Photogrammetry and Remote Sensing, 56*, 257-268.

Losel, D. G. (2009). *Earth Observation Solutions from RapidEye for Agriculture Needs*. Retrieved from www.fieldfact.com/LinkClick.aspx?fileticket...tabid=601

Lu, D., & Weng, Q. (2007). A survey of image classification methods and techniques for improving classification performance. *International Journal of Remote Sensing, 28*(5), 823- 870. doi: 10.1080/01431160600746456

Lunneta, R. S. & Elvidge, C. D. (1999). *Remote Sensing Change Dectetion: Environmental Monitoring Methods and Applications.* London: Tailor and Franscis, Ltd.

Luque, S.S. (2000). The challenge to manage the biological integrity of nature reserves: a landscape ecology perspective. *International Journal of Remote Sensing, 21*, 2613-1643.

Luzi, G., Monserrat, O., Crosetto, M., Copons, R., & Altimir, J. (2010). *Ground-Based SAR Interferometry applied to landslides monitoring in mountainous areas*. Proceedings of the International Conference 'Mountain Risks', Florence.

Manandhar, R., Odeh, I. O. A., & Ancev, T. (2009). Improving the accuracy of land use and land cover classification of landsat data using post-classification enhancement. *Remote Sens, 1*(3), 330-344. doi:10.3390/rs1030330

Marcus, W. (2002). Mapping of stream microhabitats with high spatial resolution hyperspectral imagery. *Journal of Geographical Systems, 4*, 113–126.

Masek, J. G., Honzak, M., Goward. S.N., Liu, P., & Pak, E. (2001). Landsat-7 ETM+ as an observatory for land cover initial radiometric and geometric comparis ons with Landsat-5 Thematic Mapper. *Remote Sensing of Environment, 78*(2001), 118-130. Retrieved from http:// www.glcf.umiacs.umd.edu/library/pdf/rse78_p118.pdf

Mather, P. (1999). *Computer Processing of Remotely Sensed Images: An Introduction* (2 th ed)*. West Sussex, England: John Wiley & Sons.

Mather, P.M. (2004). *Computer Processing of Remotely-Sensed Images: An Introduction*. England: John Wiley & Sons Ltd.

May, A. M. B., Pinder, J. E., & Kroh, G. C. (1997). A comparison of Landsat Thematic Mapper and SPOT multi-spectral imagery for the classification of shrub and meadow vegetation in northern California, U.S.A. *International Journal of Remote Sensing, 18*, 3719-3728.

Méléder, V., Launeau, P., Barillé, L., & Rincé, Y. (2003). Microphytobenthos assemblage mapping by spatial visible-infrared remote sensing in a shellfish ecosystem. *Comptes Rendus Biologies, 11*, 437-451.

Meyer, P., Staenz, K., & Itten, K. I. (1996). Semi-automated procedures for tree species identification in high resolution data from digitized color infrared aerial photography. *ISPRS Journal of Photogrammetry and Remote Sensing, 51*, 5–16.

Meyer, W. B. (1995). Past and Present Land-use and Land-cover in the U.S.A. *Consequences, 1*(1), 24-33.

Ministry for the Environment. (2010, April). *Legally Protected Conservation land in New Zealand* . Retrieved May 3rd, 2012, from www.mfe.govt.nz: http://www.mfe.govt.nz/environmental-reporting/report-cards/biodiversity/2010/protected-land.pdf

Ministry for the Environment. (2012, May). *Land Classification System.* Retrieved from http://www.mfe.govt.nz/environmental-reporting/about/tools-guidelines/classifications/land/index.html

Moran, M. S., Bryant, R., & Thome, K. (2001). A refined empirical line approach for reflectance factor retrieval from Landsat-5 TM and Landsat-7 ETM+. *Remote Sens Environ, 78*, 71-82.

Mumby, P. J., & Edwards, A. J. (2002). Mapping marine environments with IKONOS imagery:Enhanced spatial resolution can deliver greater thematic accuracy. *Remote Sensing of Environment, 82*, 248-257.

Munoz-Villers, L. E. and J. Lopez-Blanco. 2008. Land use/cover changes using Landsat TM/ETM images in a tropical and biodiverse mountainous area of central-eastern Mexico. *International Journal of Remote Sensing, 29*(1), 71-93. doi:10.1080/01431160701280967

Murakani, T., Ogawa, S., Ishitsuka, N., Kumagai, K., & Saito, G. (2001). Crop Discrimination with Multi-temporal SPOT/HRV data in the saga Plains, Japan. *International Journal of Remote Sensing , 22*(7), 1335-1348.

Myers, V.I. (1983). Remote Sensing Applications in Agriculture. In R.N. Colwell (Ed.), *Manual of Remote Sensing* (2nd ed.). Falls Church: American Soc. of Photogrammetry.

NASA. (2011). *The Landsat 7 Compositor*. Retrieved from http://landsat.gsfc.nasa.gov/education/compositor

Nelson, T., Niemann, K.O., & Wulder, M. (2003). Spatial statistical techniques for aggregating point objects extracted from high spatial resolution remotely sensed imagery. *Journal of Geographical Systems, 4*, 423-433.doi: 10.1007/s101090300092

Olmanson, L. G., Bauer, M. E., & Brezonik, P. L. (2002, November). *Water quality monitoring of 10,000 Minnesota Lakes: statewide classification of lake water clarity using Landsat imagery.* Proceedings, 15th William T. Pecora Memorial Remote Sensing Symposium, Denver, Colorado.

Ozdemir, I., Asan, U., Koch, B., Yesil, A., Ozkan, U. Y., & Hemphill, S. (2005). Comparison of Quickbird-2 and Landsat-7 ETM+ data formapping of vegetation cover in Fethiye Kumluova coastal dune in the Mediterranean region of Turkey. *Fresenius Environ. Bull., 14* (9), 823-831.

Paiboonvorachat, C. (2008). *Using remote sensing and GIS techniques to assess land use/land cover change in the Nan watershed* (Master's thesis, Southern Illinois University Carbondale, USA).

Pengra, B. W., Johnston, C. A., & Loveland, T. R. (2007). Mapping an invasive plant, Phragmites australis, in coastal wetlands using the EO-1 Hyperion hyperspectral sensor. *Remote Sensing of Environment,* 108, 74-81.

Peterson, E. B. (2008). *A synthesis of vegetation maps for Nevada (Initiating a living vegetation map)* (1st ed.). Nevada Natural Heritage Program, Carson City, Nevada.

Phinn, S., Roelfsema, C., Brando, V., & Anstee, J. (2008). Mapping seagrass species, cover and biomass in shallow water: An assessment of satellite multi-spectral and airborne hyper spectral imaging system in Moreton Bay (Australia). *Remote Sensing of Environment, 112,* 3413-3425.

RapidEye. (2012). *High resolution satellite imagery.* Retrieved February 12, 2012, from http://www.rapideye.com/products/ortho.htm

Reitz, G., Facius, R., Bilski, P., & Olko, P. (2002). Investigation of radiation doses in open space using TLD detectors. *Radiat Prot Dosim, 100*, 533-536.

Richards, J.A., & Jia, X. (2006). *Remote Sensing Digital Image Analysis*. Germany: Springer Verlag Berlin Heidelberg.

Richards, J.A., & Watt, J. C. (2006). *Remote Sensing Digital Image Analysis: An Introduction* (4th ed.). Berlin, Germany: Springer.

Riebsame, W. E., Meyer, W. B., & Turner, B. L. (1994). Modeling Land-use and Cover as Part of Global Environmental Change. *Climate Change, 28*, 45-64.

Rogerson, P. A. (2001). *Statistical Methods for Geography: A student's guide* (2nd ed.). London, UK: Sage Publications.

Rosso, P. H., Ustin, S. L., & Hastings, A. (2005). Mapping marshland vegetation of San Francisco Bay, California, using hyperspectral data. *Int J Remote Sens, 26*, 5169-91.

Schroeder, T.A., Canty, M. J., & Yang, Z. (2006). Radiometric correction of multi-temporal Landsat data for characterization of early successional forest patterns in western Oregon. *Remote Sens. Environ., 103*, 16-26.

Shirish, A. R., Roy, P. S. & Sharma, C. M. (1995). Space remote sensing for spatial vegetation characterization. *J. Biosci, 20*(3), 427-438. Retrieved from http://www.ias.ac.in/jarch/jbiosci/20/427-438.pdf

Sholtz, D., Fuhs, N., & Hixson, M. (1979, April). *An evaluation of several different classification schemes_ Their parameters and performance (maximum likelihood decision for crop identification)*. Paper presented at the International Symposium on Remote Sensing of Environment, United States.

Sivakumar,V., Morel, B., Bencherif, H., Baray, J. L., Baldy, S., Hauchecorne, A., & Rao, P.B. (2004). Rayleigh lidar observation of a warm stratopause over a tropical site, Gadanki (13.5_ N; 79.2_ E). *Atmos. Chem. Phys., 4*, 1989-1996.

Skidmore, A. K. (2002). *Land use and Land cover*. New York: Mrcel Dekker, Inc.

Stephens, P.R. (1991). Remote sensing in New Zealand. *Geocarto International, 6*, 90-2.

Sundarakumar, K., Harika, S. K., Begum, A., Yamini, S., & Balakrishna, K. (2012). Land use and cover change detection and urban sprawl analysis of Vijayawada city using multitemporal Landsat data. *International Journal of Engineering Science and Technology, 4*(1), 170-178. Retrieved from http:// www.ijest.info/docs/IJEST12-04-01-114.pdf

Tekinary, C. (2009). *Classification of remotely sensed data by using 2D local discriminant base* (Masters's thesis, Middle East Technical University, Ankara, Turkey). Retrieved from http:// www.etd.lib.metu.edu.tr/upload/3/12610782/index.pdf

Thomas, C. J., Davies, G., & Dunn, C. E. (2004). Mixed Picture for Changes in Stable Malaria Distribution with Future Climate in Africa. *Trends in Parasitology, 20*(5), 216–220.

Thompson, S., Grüner, I., & Gapar, N. (2003). *New Zealand Land Cover Database Version 2: Illustrated Guide to Target Classes*._ Ministry for the Environment, Wellington.

Tso, B., & Mather, P. M. (2009). *Classification methods for remotely sensed data* (2nd ed.). Boca Raton, US: Taylor & Francis Group, CRC Press.

Tso, B., & Olsen, R. (2005). Combining spectral and spatial information into hidden Markov models for unsupervised image classification. *Int J Remote Sens, 26*, 2113–33.

Tucker, C. J. (1979). Red and photographic infrared linear combinations for monitoring vegetation. *Remote Sens. Environ*, *8*, 127-150. Retrieved January 22, 2012.

Turner, D. P, Ollinger, S. V, & Kimball, J. S. (2004). Integrating remote sensing and ecosystem process models for landscape to regional scale analysis of the carbon cycle. *BioScience, 54*, 573-584.

Uluocha, N. O. (2003). *Interfacing indigenous knowledge and GIS for sustainable rural mapping and development*. Paper presented at the 21st International Cartographic Conference (ICC), Durban, South Africa.

Vaiphasa, C., Ongsomwang, S., Vaiphasa, T., & Skidmore, A. K. (2005). Tropical mangrove species discrimination using hyperspectral data: a laboratory study. *Estuarine Coastal Shelf Sci,* 65, 371-379.

Vitousek, P. M. (1994). Beyond Global Warming: Ecology and Global Change. *Ecology, 75*, 1861-1876.

Vogelmann, J. E. (1999). Effects of Landsat Thematic Mapper radiometric and geometric calibrations on selected land cover analyses. *American Society for Photogrammetry and Remote Sensing, 46*, 143-153.

Vogelmann, J. E., Helder, D., Morfitt, R., Choate, M. J., Merchant, J. W., & Bulley, H. (2001). Effects of Landsat 5 Thematic Mapper and Landsat7 Enhanced Thematic Mapper Plus radiometric and geometric calibrations and corrections on landscape characterization. *Remote Sensing of Environment, 78*(1), 55-70. doi: 10.1016/S0034-4257(01)00249-8

Vogelmann, J.E., T. Sohl, and S.M. Howard. (1998). Regional characterization of land cover using multiple sources of data. *Photogrammetric Engineering and Remote Sensing, 64*(1), 45-57.

Walker, S., Price, R., Rutledge, D., Stephens, R.T.T., & Lee, W.G. (2006). Recent loss of indigenous cover in New Zealand. *New Zealand Journal of Ecology, 30*, 169-77.

Wulder, M. A., Hall, R. J., Coops, N. C., & Franklin, S. E. (2004). High spatial resolution Remotely Sensed Data for Ecosystem Characterization. *BioScience, 54*(6), 511-521. doi: 10.1641/0006-3568(2004)054[0511:HSRRSD]2.0.CO;2

Xie,Y., Sha, Z., & Yu, M. (2008). Remote sensing imagery in vegetation mapping: a review. *Journal of Plant Ecology, 1*(1), 9-23.doi: 10.1093/jpe/rtm005

Yichun, X., Zongyao, S., & Mei, Y. (2008). Remote sensing imagery in vegetation mapping: a review. *Journal of Plant Ecology*, *1*(1), 9-23. doi: 10.1093/jpe/rtm005

Younggu, H. (2007, June). *Land use classification in Zambia using Quickbird and Landsat imagery*. Paper presented at the American society of Agriculture and Biological Engineers, Minnesota, US. Retrieved from http://www.pdf.usaid.gov/pdf_docs/PNADL355.pdf

Yuan, D., Elvidge, C. D., & Lunetta, R. S. (1998). Survey of multispectral methods for land cover change analysis. R. S. Lunetta and C. D. Elvidge (Eds.), *In Remote Sensing Change Detection: Environmental Monitoring Methods and Applications* (pp. 21-39). Chelsea, MI: Ann Arbor Press.

Zheng, C. H., Zeng, C. S., & Chen, Z.Q. (2006). A study on the changes of landscape pattern of estuary wetlands of the Minjiang river. *Wetland Sci, 4*, 29-35.

Appendix

Original Data and Processing

Appendix1.1Landsat 7 Metadata

```
GROUP = METADATA_FILE
      PRODUCT_CREATION_TIME = 2004-02-12T14:51:10Z
      PRODUCT_FILE_SIZE = 703.5
      STATION_ID = "EDC"
      GROUND_STATION = "EDC"
      GROUP = ORTHO_PRODUCT_METADATA
            SPACECRAFT_ID = "Landsat7"
            SENSOR_ID = "ETM+"
            ACQUISITION_DATE = 2001-06-03
            WRS_PATH = 075
            WRS_ROW = 084
            SCENE_CENTER_LAT = -34.6058947
            SCENE_CENTER_LON = +172.9906758
            SCENE_UL_CORNER_LAT = -33.6506199
            SCENE_UL_CORNER_LON = +172.2282297
            SCENE_UR_CORNER_LAT = -33.9390168
            SCENE_UR_CORNER_LON = +174.2085713
            SCENE_LL_CORNER_LAT = -35.2610079
            SCENE_LL_CORNER_LON = +171.7532610
            SCENE_LR_CORNER_LAT = -35.5555498
            SCENE_LR_CORNER_LON = +173.7707419
            SCENE_UL_CORNER_MAPX = 613890.000
            SCENE_UL_CORNER_MAPY = -3724095.000
            SCENE_UR_CORNER_MAPX = 796575.000
            SCENE_UR_CORNER_MAPY = -3760033.500
            SCENE_LL_CORNER_MAPX = 568518.000
            SCENE_LL_CORNER_MAPY = -3902248.500
            SCENE_LR_CORNER_MAPX = 751146.000
            SCENE_LR_CORNER_MAPY = -3938187.000
            BAND1_FILE_NAME = "p075r084_7t20010603_z59_nn10.tif"
            BAND2_FILE_NAME = "p075r084_7t20010603_z59_nn20.tif"
            BAND3_FILE_NAME = "p075r084_7t20010603_z59_nn30.tif"
            BAND4_FILE_NAME = "p075r084_7t20010603_z59_nn40.tif"
            BAND5_FILE_NAME = "p075r084_7t20010603_z59_nn50.tif"
            BAND61_FILE_NAME = "p075r084_7k20010603_z59_nn61.tif"
            BAND62_FILE_NAME = "p075r084_7k20010603_z59_nn62.tif"
            BAND7_FILE_NAME = "p075r084_7t20010603_z59_nn70.tif"
            BAND8_FILE_NAME = "p075r084_7p20010603_z59_nn80.tif"
            GROUP = PROJECTION_PARAMETERS
                  REFERENCE_DATUM = "WGS84"
                  REFERENCE_ELLIPSOID = "WGS84"
                  GRID_CELL_ORIGIN = "Center"
                  UL_GRID_LINE_NUMBER = 1
                  UL_GRID_SAMPLE_NUMBER = 1
                  GRID_INCREMENT_UNIT = "Meters"
                  GRID_CELL_SIZE_PAN = 14.250
                  GRID_CELL_SIZE_THM = 57.000
                  GRID_CELL_SIZE_REF = 28.500
                  FALSE_NORTHING = 0
                  ORIENTATION = "NUP"
                  RESAMPLING_OPTION = "NN"
                  MAP_PROJECTION = "UTM"
            END_GROUP = PROJECTION_PARAMETERS
            GROUP = UTM_PARAMETERS
```

```
            ZONE_NUMBER = +59
        END_GROUP = UTM_PARAMETERS
        SUN_AZIMUTH = 35.2678391
        SUN_ELEVATION = 24.1170033
        QA_PERCENT_MISSING_DATA = 0
        CLOUD_COVER = 0
        PRODUCT_SAMPLES_PAN = 17714
        PRODUCT_LINES_PAN = 15852
        PRODUCT_SAMPLES_REF = 8857
        PRODUCT_LINES_REF = 7926
        PRODUCT_SAMPLES_THM = 4429
        PRODUCT_LINES_THM = 3963
        OUTPUT_FORMAT = "GEOTIFF"
    END_GROUP = ORTHO_PRODUCT_METADATA
    GROUP = L1G_PRODUCT_METADATA
        BAND_COMBINATION = "123456678"
        CPF_FILE_NAME = "L7CPF20010401_20010630_07"
        GROUP = MIN_MAX_RADIANCE
            LMAX_BAND1 = 191.600
            LMIN_BAND1 = -6.200
            LMAX_BAND2 = 196.500
            LMIN_BAND2 = -6.400
            LMAX_BAND3 = 152.900
            LMIN_BAND3 = -5.000
            LMAX_BAND4 = 157.400
            LMIN_BAND4 = -5.100
            LMAX_BAND5 = 31.060
            LMIN_BAND5 = -1.000
            LMAX_BAND61 = 17.040
            LMIN_BAND61 = 0.000
            LMAX_BAND62 = 12.650
            LMIN_BAND62 = 3.200
            LMAX_BAND7 = 10.800
            LMIN_BAND7 = -0.350
            LMAX_BAND8 = 243.100
            LMIN_BAND8 = -4.700
        END_GROUP = MIN_MAX_RADIANCE
        GROUP = MIN_MAX_PIXEL_VALUE
            QCALMAX_BAND1 = 255.0
            QCALMIN_BAND1 = 1.0
            QCALMAX_BAND2 = 255.0
            QCALMIN_BAND2 = 1.0
            QCALMAX_BAND3 = 255.0
            QCALMIN_BAND3 = 1.0
            QCALMAX_BAND4 = 255.0
            QCALMIN_BAND4 = 1.0
            QCALMAX_BAND5 = 255.0
            QCALMIN_BAND5 = 1.0
            QCALMAX_BAND61 = 255.0
            QCALMIN_BAND61 = 1.0
            QCALMAX_BAND62 = 255.0
            QCALMIN_BAND62 = 1.0
            QCALMAX_BAND7 = 255.0
            QCALMIN_BAND7 = 1.0
            QCALMAX_BAND8 = 255.0
            QCALMIN_BAND8 = 1.0
        END_GROUP = MIN_MAX_PIXEL_VALUE
        GROUP = PRODUCT_PARAMETERS
```

```
                        CORRECTION_METHOD_GAIN_BAND1 = "CPF"
                        CORRECTION_METHOD_GAIN_BAND2 = "CPF"
                        CORRECTION_METHOD_GAIN_BAND3 = "CPF"
                        CORRECTION_METHOD_GAIN_BAND4 = "CPF"
                        CORRECTION_METHOD_GAIN_BAND5 = "CPF"
                        CORRECTION_METHOD_GAIN_BAND61 = "CPF"
                        CORRECTION_METHOD_GAIN_BAND62 = "CPF"
                        CORRECTION_METHOD_GAIN_BAND7 = "CPF"
                        CORRECTION_METHOD_GAIN_BAND8 = "CPF"
                        CORRECTION_METHOD_BIAS = "IC"
                        BAND1_GAIN = "H"
                        BAND2_GAIN = "H"
                        BAND3_GAIN = "H"
                        BAND4_GAIN = "H"
                        BAND5_GAIN = "H"
                        BAND6_GAIN1 = "L"
                        BAND6_GAIN2 = "H"
                        BAND7_GAIN = "H"
                        BAND8_GAIN = "L"
                        BAND1_GAIN_CHANGE = "0"
                        BAND2_GAIN_CHANGE = "0"
                        BAND3_GAIN_CHANGE = "0"
                        BAND4_GAIN_CHANGE = "0"
                        BAND5_GAIN_CHANGE = "0"
                        BAND6_GAIN_CHANGE1 = "0"
                        BAND6_GAIN_CHANGE2 = "0"
                        BAND7_GAIN_CHANGE = "0"
                        BAND8_GAIN_CHANGE = "0"
                        BAND1_SL_GAIN_CHANGE = "0"
                        BAND2_SL_GAIN_CHANGE = "0"
                        BAND3_SL_GAIN_CHANGE = "0"
                        BAND4_SL_GAIN_CHANGE = "0"
                        BAND5_SL_GAIN_CHANGE = "0"
                        BAND6_SL_GAIN_CHANGE1 = "0"
                        BAND6_SL_GAIN_CHANGE2 = "0"
                        BAND7_SL_GAIN_CHANGE = "0"
                        BAND8_SL_GAIN_CHANGE = "0"
                END_GROUP = PRODUCT_PARAMETERS
                GROUP = CORRECTIONS_APPLIED
                        STRIPING_BAND1 = "NONE"
                        STRIPING_BAND2 = "NONE"
                        STRIPING_BAND3 = "NONE"
                        STRIPING_BAND4 = "NONE"
                        STRIPING_BAND5 = "NONE"
                        STRIPING_BAND61 = "NONE"
                        STRIPING_BAND62 = "NONE"
                        STRIPING_BAND7 = "NONE"
                        STRIPING_BAND8 = "NONE"
                        BANDING = "N"
                        COHERENT_NOISE = "N"
                        MEMORY_EFFECT = "N"
                        SCAN_CORRELATED_SHIFT = "N"
                        INOPERABLE_DETECTORS = "N"
                        DROPPED_LINES = N
                END_GROUP = CORRECTIONS_APPLIED
        END_GROUP = L1G_PRODUCT_METADATA
END_GROUP = METADATA_FILE
END
```

Appendix1.2 RapidEye Metadata

```xml
<?xml version="1.0" encoding="UTF-8" standalone="no" ?>
– <re:EarthObservation
xmlns:re="http://schemas.rapideye.de/products/productMetadataGeocorrected
" re_standard_product_version="3.0" version="1.2.1"
xmlns:eop="http://earth.esa.int/eop"
xmlns:gml="http://www.opengis.net/gml" xmlns:opt="http://earth.esa.int/opt"
xmlns:xlink="http://www.w3.org/1999/xlink"
xmlns:xs="http://www.w3.org/2001/XMLSchema"
xmlns:xsi="http://www.w3.org/2001/XMLSchema-instance"
xsi:schemaLocation="http://schemas.rapideye.de/products/productMetadataGe
ocorrected
http://schemas.rapideye.de/products/re/3.0/RapidEye_ProductMetadata_Geo
correctedLevel.xsd">
– <gml:metaDataProperty>
– <re:EarthObservationMetaData>
<eop:identifier>2010-12-08T233034_RE2_3A-
NAC_8169366_126793</eop:identifier>
<eop:acquisitionType>NOMINAL</eop:acquisitionType>
<eop:productType>L3A</eop:productType>
<eop:status>ARCHIVED</eop:status>
– <eop:downlinkedTo>
– <eop:DownlinkInformation>
<eop:acquisitionStation
codeSpace="urn:eop:RE:stationLocation">Svalbard</eop:acquisitionStation>
<eop:acquisitionDate>2010-12-08T23:30:34.767739Z</eop:acquisitionDate>
</eop:DownlinkInformation>
</eop:downlinkedTo>
– <eop:archivedIn>
– <eop:ArchivingInformation>
<eop:archivingCenter
codeSpace="urn:eop:RE:stationLocation">BRB</eop:archivingCenter>
<eop:archivingDate>2010-12-21T18:29:27Z</eop:archivingDate>
<eop:archivingIdentifier
codeSpace="urn:eop:RE:dmsCatalogueId">8169366</eop:archivingIdentifier>
</eop:ArchivingInformation>
</eop:archivedIn>
– <eop:processing>
– <eop:ProcessingInformation>
<eop:processorName>DPS</eop:processorName>
<eop:processorVersion>3.5.1</eop:processorVersion>
<eop:nativeProductFormat>GeoTIFF</eop:nativeProductFormat>
</eop:ProcessingInformation>
</eop:processing>
– <re:license>
<re:licenseType>Scientific</re:licenseType>
<re:resourceLink xlink:href="http://info.rapideye.de/license/License_SCIENTIFIC-
2011-02-15.txt" xlink:title="RE EULA" />
</re:license>
<re:versionIsd>3.0</re:versionIsd>
<re:110ilenam>126793</re:110ilenam>
<re:tileId>5923023</re:tileId>
```

```xml
<re:pixelFormat>16U</re:pixelFormat>
          </re:EarthObservationMetaData>
        </gml:metaDataProperty>
        – <gml:validTime>
        – <gml:TimePeriod>
<gml:beginPosition>2010-12-08T23:30:20Z</gml:beginPosition>
  <gml:endPosition>2010-12-08T23:30:46Z</gml:endPosition>
          </gml:TimePeriod>
         </gml:validTime>
         – <gml:using>
        – <eop:EarthObservationEquipment>
          – <eop:platform>
          – <eop:Platform>
    <eop:shortName>RE00</eop:shortName>
  <eop:serialIdentifier>RE-2</eop:serialIdentifier>
    <eop:orbitType>LEO</eop:orbitType>
          </eop:Platform>
          </eop:platform>
        – <eop:instrument>
        – <eop:Instrument>
    <eop:shortName>MSI</eop:shortName>
          </eop:Instrument>
          </eop:instrument>
        – <eop:sensor>
        – <re:Sensor>
 <eop:sensorType>OPTICAL</eop:sensorType>
 <eop:resolution uom="m">6.5</eop:resolution>
    <re:scanType>PUSHBROOM</re:scanType>
             </re:Sensor>
            </eop:sensor>
        – <eop:acquisitionParameters>
        – <re:Acquisition>
   <eop:orbitDirection>DESCENDING</eop:orbitDirection>
 <eop:incidenceAngle uom="deg">5.360000e+00</eop:incidenceAngle>
           <opt:illuminationAzimuthAngle
 uom="deg">4.511494e+01</opt:illuminationAzimuthAngle>
           <opt:illuminationElevationAngle
 uom="deg">7.410421e+01</opt:illuminationElevationAngle>
    <re:azimuthAngle uom="deg">9.881000e+01</re:azimuthAngle>
 <re:spaceCraftViewAngle uom="deg">-3.257890e+00</re:spaceCraftViewAngle>
<re:acquisitionDateTime>2010-12-08T23:30:34.767739Z</re:acquisitionDateTime>
            </re:Acquisition>
          </eop:acquisitionParameters>
         </eop:EarthObservationEquipment>
            </gml:using>
         – <gml:target>
         – <re:Footprint>
        – <gml:multiExtentOf>
      – <gml:MultiSurface srsName="EPSG:4326">
         – <gml:surfaceMembers>
           – <gml:Polygon>
           – <gml:exterior>
           – <gml:LinearRing>
```

```
<gml:posList>-3.467961317694210e+01 1.730903390739995e+02 -
3.467463055501177e+01 1.733629777575798e+02 -
3.489983664134533e+01 1.733694131917195e+02 -
3.490486099058384e+01 1.730960334024918e+02 -
3.467961317694210e+01 1.730903390739995e+02</gml:posList>
                </gml:LinearRing>
                  </gml:exterior>
                  </gml:Polygon>
               </gml:surfaceMembers>
                </gml:MultiSurface>
                </gml:multiExtentOf>
              – <gml:centerOf>
         – <gml:Point srsName="EPSG:4326">
      <gml:pos>-3.478979e+01 1.732297e+02</gml:pos>
                    </gml:Point>
                  </gml:centerOf>
             – <re:geographicLocation>
                 – <re:topLeft>
    <re:latitude>-3.467961317694210e+01</re:latitude>
    <re:longitude>1.730903390739995e+02</re:longitude>
                    </re:topLeft>
                – <re:topRight>
    <re:latitude>-3.467463055501177e+01</re:latitude>
    <re:longitude>1.733629777575798e+02</re:longitude>
                   </re:topRight>
              – <re:bottomRight>
    <re:latitude>-3.489983664134533e+01</re:latitude>
    <re:longitude>1.733694131917195e+02</re:longitude>
                 </re:bottomRight>
             – <re:bottomLeft>
    <re:latitude>-3.490486099058384e+01</re:latitude>
    <re:longitude>1.730960334024918e+02</re:longitude>
                  </re:bottomLeft>
              </re:geographicLocation>
                 </re:Footprint>
                 </gml:target>
              – <gml:resultOf>
           – <re:EarthObservationResult>
                – <eop:browse>
             – <eop:BrowseInformation>
           <eop:type>QUICKLOOK</eop:type>
              <eop:referenceSystemIdentifier
     codeSpace="EPSG">4326</eop:referenceSystemIdentifier>
        <eop:112ilename>2010-12-08T233034_RE2_3A-
     NAC_8169366_126793_browse.tif</eop:112ilename>
                </eop:BrowseInformation>
                  </eop:browse>
              – <eop:product>
             – <re:ProductInformation>
        <eop:112ilename>2010-12-08T233034_RE2_3A-
        NAC_8169366_126793.tif</eop:112ilename>
           <eop:size uom="KB">244181</eop:size>
        <re:productFormat>GeoTIFF</re:productFormat>
```

```
– <re:spatialReferenceSystem>
      <re:epsgCode>32759</re:epsgCode>
   <re:geodeticDatum>WGS_1984</re:geodeticDatum>
  <re:projection>WGS 84 / UTM zone 59S</re:projection>
      <re:projectionZone>59</re:projectionZone>
    </re:spatialReferenceSystem>
   <re:resamplingKernel>CC</re:resamplingKernel>
      <re:numRows>5000</re:numRows>
   <re:numColumns>5000</re:numColumns>
      <re:numBands>5</re:numBands>
        <re:rowGsd>5</re:rowGsd>
      <re:columnGsd>5</re:columnGsd>
  <re:radiometricCorrectionApplied>true</re:radiometricCorrectionApplied>
  <re:radiometricCalibrationVersion>v6.0</re:radiometricCalibrationVersion>
  <re:geoCorrectionLevel>Precision Geocorrection</re:geoCorrectionLevel>
  <re:elevationCorrectionApplied>FineDEM</re:elevationCorrectionApplied>
  <re:atmosphericCorrectionApplied>false</re:atmosphericCorrectionApplied>
  <re:productAccuracy>2.048382568359375e+01</re:productAccuracy>
        </re:ProductInformation>
          </eop:product>
        – <eop:mask>
      – <eop:MaskInformation>
   <eop:type>UNUSABLE DATA</eop:type>
      <eop:format>RASTER</eop:format>
      <eop:referenceSystemIdentifier
  codeSpace="EPSG">32759</eop:referenceSystemIdentifier>
      <eop:113ilename>2010-12-08T233034_RE2_3A-
        NAC_8169366_126793_udm.tif</eop:113ilename>
         </eop:MaskInformation>
          </eop:mask>
  <opt:cloudCoverPercentage uom="%">64</opt:cloudCoverPercentage>
       <opt:cloudCoverPercentageAssessmentConfidence
  uom="%">70</opt:cloudCoverPercentageAssessmentConfidence>

  <opt:cloudCoverPercentageQuotationMode>AUTOMATIC</opt:cloudCoverPercentageQ
                uotationMode>
  <re:unusableDataPercentage uom="%">64</re:unusableDataPercentage>
        – <re:bandSpecificMetadata>
      <re:bandNumber>1</re:bandNumber>
  <re:percentMissingLines>0.000000000000000e+00</re:percentMissingLines>
  <re:percentSuspectLines>0.000000000000000e+00</re:percentSuspectLines>
        <re:binning>1x1</re:binning>
        <re:shifting>1</re:shifting>
        <re:masking>111</re:masking>
  <re:radiometricScaleFactor>9.999999776482582e-03</re:radiometricScaleFactor>
        </re:bandSpecificMetadata>
        – <re:bandSpecificMetadata>
      <re:bandNumber>2</re:bandNumber>
  <re:percentMissingLines>0.000000000000000e+00</re:percentMissingLines>
  <re:percentSuspectLines>0.000000000000000e+00</re:percentSuspectLines>
        <re:binning>1x1</re:binning>
        <re:shifting>1</re:shifting>
        <re:masking>111</re:masking>
```

```xml
<re:radiometricScaleFactor>9.9999997776482582e-03</re:radiometricScaleFactor>
                </re:bandSpecificMetadata>
            – <re:bandSpecificMetadata>
            <re:bandNumber>3</re:bandNumber>
  <re:percentMissingLines>0.000000000000000e+00</re:percentMissingLines>
  <re:percentSuspectLines>0.000000000000000e+00</re:percentSuspectLines>
                <re:binning>1x1</re:binning>
                <re:shifting>1</re:shifting>
                <re:masking>111</re:masking>
<re:radiometricScaleFactor>9.999999776482582e-03</re:radiometricScaleFactor>
                </re:bandSpecificMetadata>
            – <re:bandSpecificMetadata>
            <re:bandNumber>4</re:bandNumber>
  <re:percentMissingLines>0.000000000000000e+00</re:percentMissingLines>
  <re:percentSuspectLines>0.000000000000000e+00</re:percentSuspectLines>
                <re:binning>1x1</re:binning>
                <re:shifting>1</re:shifting>
                <re:masking>111</re:masking>
<re:radiometricScaleFactor>9.999999776482582e-03</re:radiometricScaleFactor>
                </re:bandSpecificMetadata>
            – <re:bandSpecificMetadata>
            <re:bandNumber>5</re:bandNumber>
  <re:percentMissingLines>0.000000000000000e+00</re:percentMissingLines>
  <re:percentSuspectLines>0.000000000000000e+00</re:percentSuspectLines>
                <re:binning>1x1</re:binning>
                <re:shifting>1</re:shifting>
                <re:masking>111</re:masking>
<re:radiometricScaleFactor>9.999999776482582e-03</re:radiometricScaleFactor>
                </re:bandSpecificMetadata>
            </re:EarthObservationResult>
                </gml:resultOf>
            </re:EarthObservation>
```
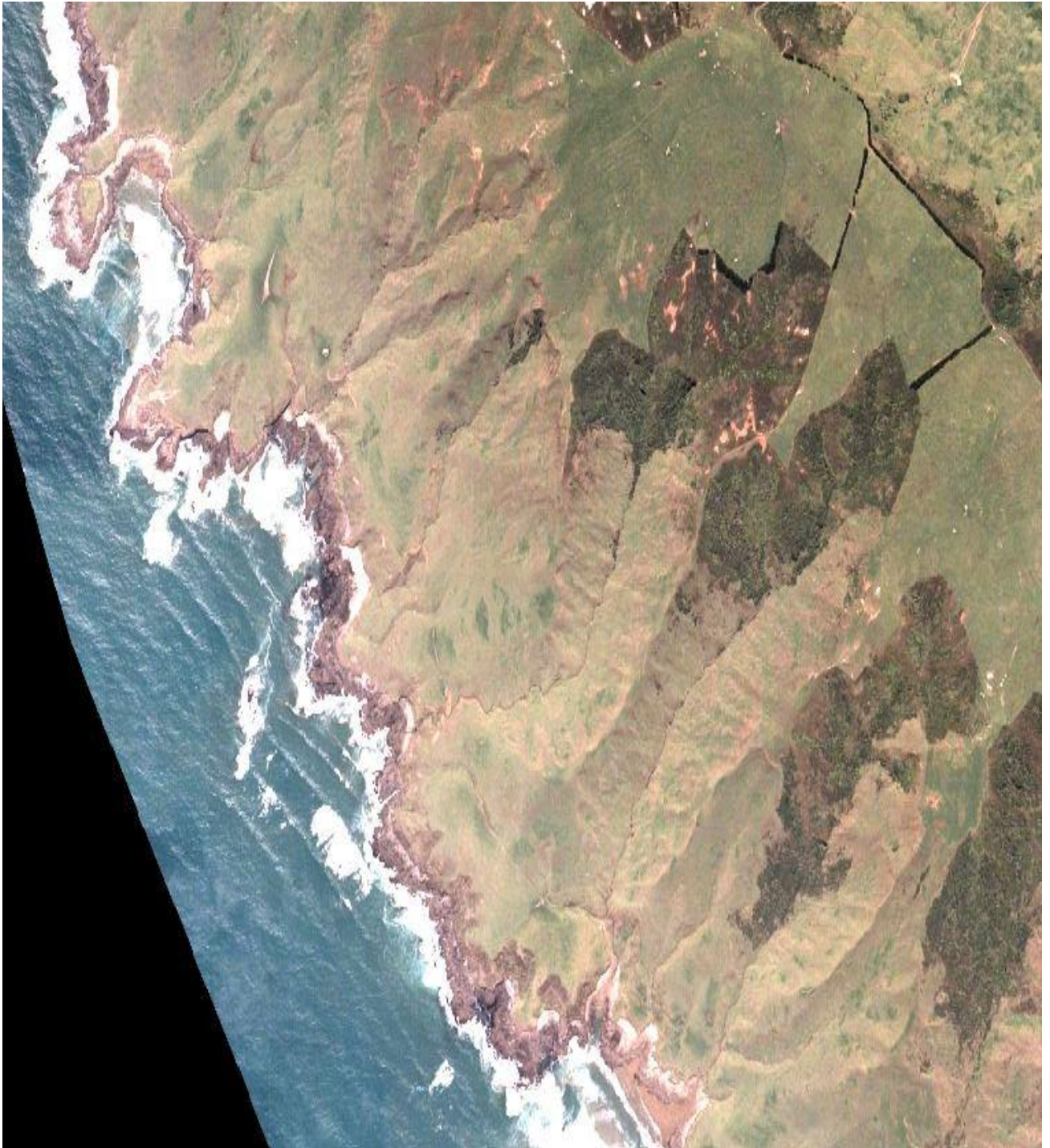
Appendix 1.3 Aerial photo_Ahipara (Koordinates, n.d.)

Appendix 1.3 Aerial photo_Ahipara (Koordinates, n.d.)
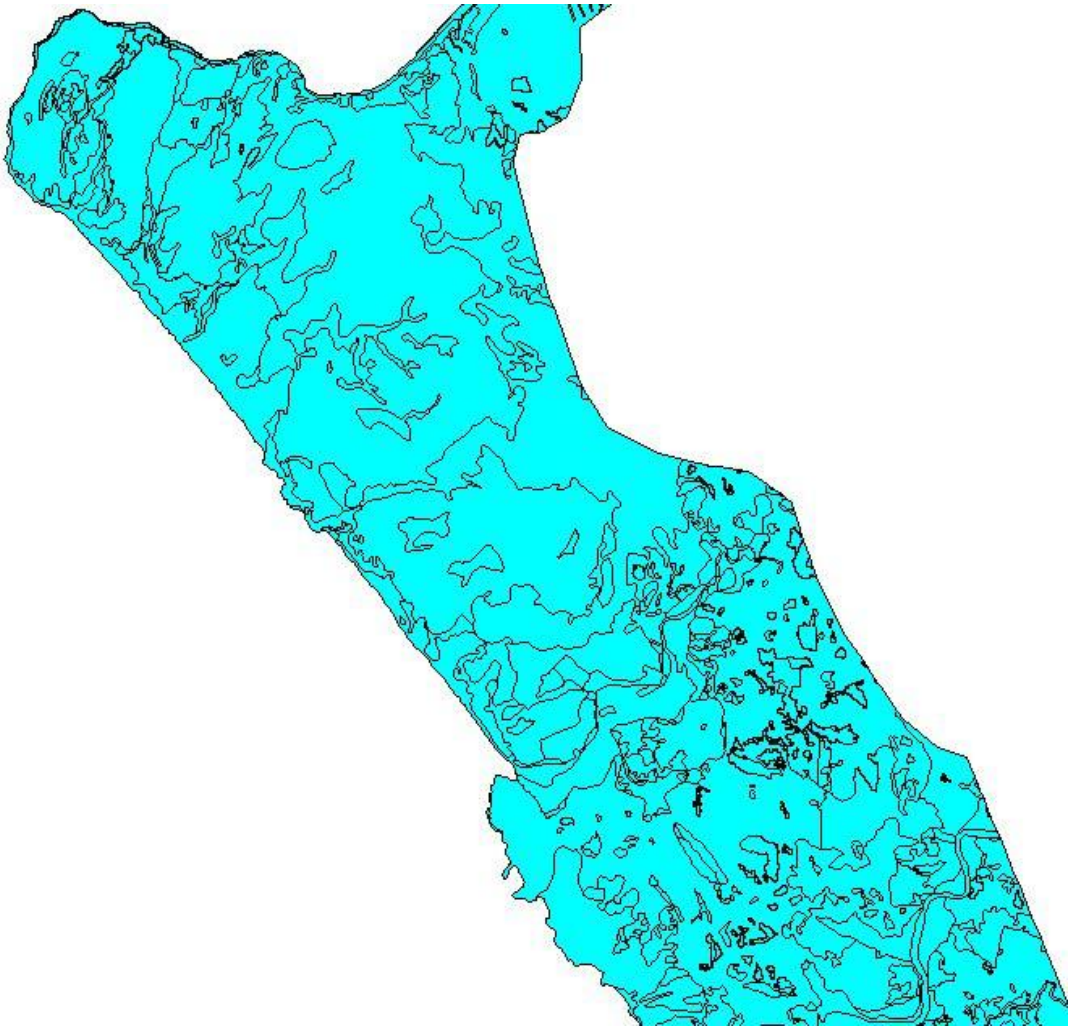
Appendix 1.4 LCDB2 Data_Ahipara
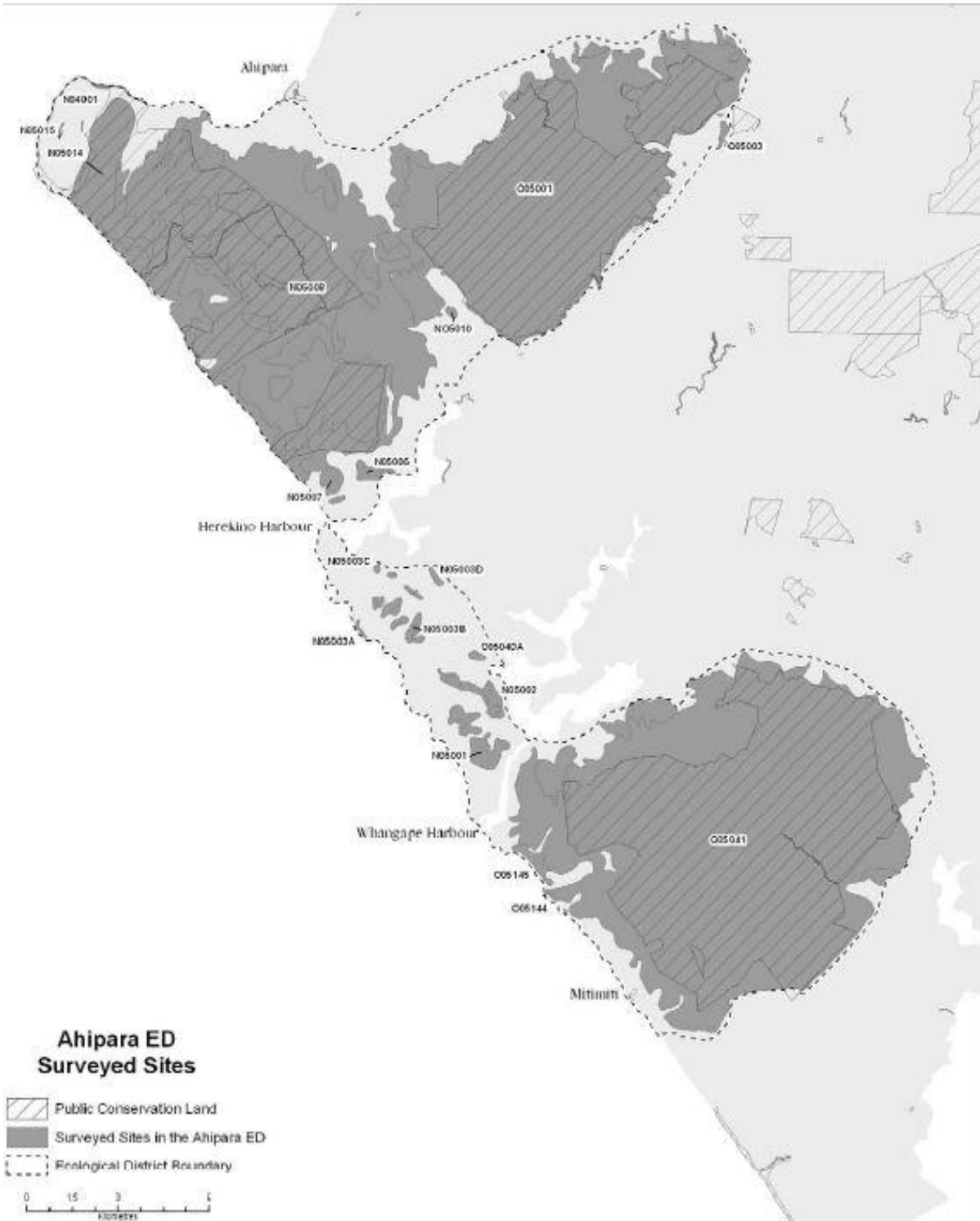
Appendix 1.5 Ahipara region

N05003B Owhata B

0   250   500   1,000
|____|____|_____|
          Metres
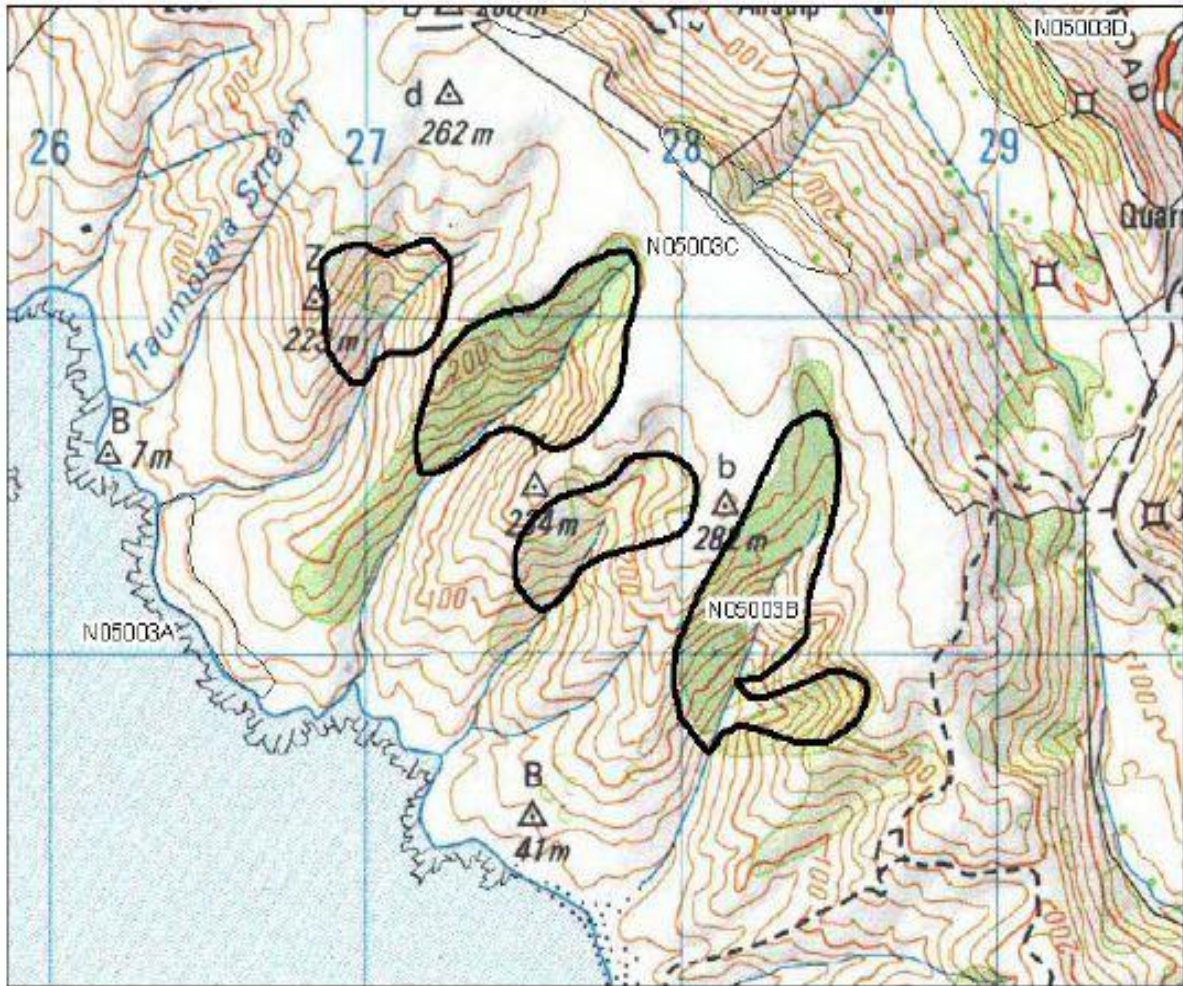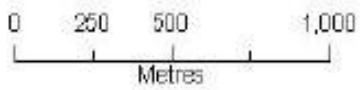
S= Shrubland
F= Forest
W= Wetland
E= Estuarine
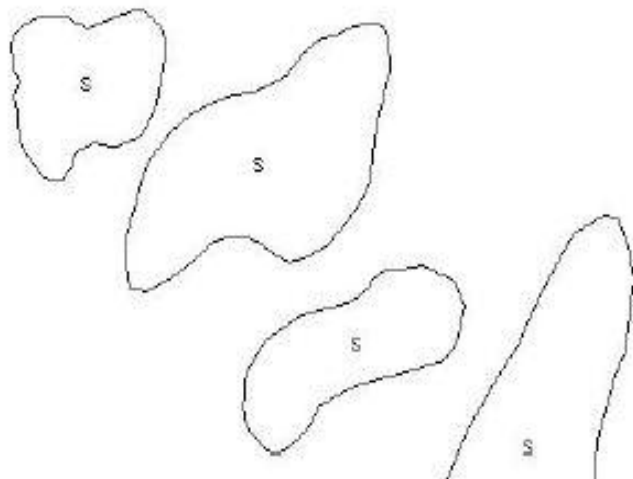
Appendix 1.6 Owhata_Ahipara